

# Ammonia Observations of Planck Cold Cores

Dilda Berdikhan<sup>1,2</sup>, Jarken Esimbek<sup>1,3,4</sup>, Christian Henkel<sup>5,1,6</sup>, Jianjun Zhou<sup>1,3,4</sup>, Xindi Tang<sup>1,2,3,4</sup>, Tie Liu<sup>7</sup>, Gang Wu<sup>5</sup>, Dalei Li<sup>1,2,3,4</sup>, Yuxin He<sup>1,2,3,4</sup>, Toktarkhan Komesh<sup>8,9</sup>, Kadiryja Tursun<sup>1,3,4</sup>, Dongdong Zhou<sup>1,3,4</sup>, Ernar Imanaly<sup>1,2</sup>, and Qaynar Jandaulet<sup>1,2</sup>

(Affiliations can be found after the references)

January 5, 2024

## ABSTRACT

Single-pointing observations of NH<sub>3</sub> (1,1) and (2,2) were conducted towards 672 Planck Early Release Cold Cores (ECCs) using the Nanshan 26-m radio telescope. Out of these sources, a detection rate of 37% (249 cores) was achieved, with NH<sub>3</sub> (1,1) hyperfine structure detected in 187 and NH<sub>3</sub> (2,2) emission lines detected in 76 cores. The detection rate of NH<sub>3</sub> is positively correlated with the continuum emission fluxes at a frequency of 857 GHz. Among the observed 672 cores, ~22% have associated stellar and IR objects within the beam size ( $\sim 2'$ ). This suggests that most of the cores in our sample may be starless. The kinetic temperatures of the cores range from 8.9 to 20.7 K, with an average of 12.3 K, indicating a coupling between gas and dust temperatures. The ammonia column densities range from  $3.6 \times 10^{14}$  to  $6.07 \times 10^{15} \text{ cm}^{-2}$ , with a median value of  $2.04 \times 10^{15} \text{ cm}^{-2}$ . The fractional abundances of ammonia range from 0.3 to  $9.7 \times 10^{-7}$ , with an average of  $2.7 \times 10^{-7}$ , which is one order of magnitude larger than that of Massive Star-Forming (MSF) regions and Infrared Dark Clouds (IRDCs). The correlation between thermal and non-thermal velocity dispersion of the NH<sub>3</sub> (1,1) inversion transition indicates the dominance of supersonic non-thermal motions in the dense gas traced by NH<sub>3</sub>, and the relationship between these two parameters in Planck cold cores is weaker, with lower values observed for both parameters relative to other samples under our examination. The cumulative distribution shapes of line widths in the Planck cold cores closely resemble those of the dense cores found in regions of Cepheus, and Orion L1630 and L1641, with higher values compared to Ophiuchus. However, the higher line width values in the Planck cold cores, when compared to these dense cores in Ophiuchus, suggest that they might be in more advanced and warmer stages of evolution. Additionally, the line width remains relatively small among the various samples examined. A comparison of NH<sub>3</sub> line-center velocities with those of <sup>13</sup>CO and C<sup>18</sup>O shows small differences (0.13 km s<sup>-1</sup> and 0.12 km s<sup>-1</sup>), suggesting quiescence on small scales.

**Key words.** surveys – radio lines: ISM – ISM: molecules – ISM: kinetics and dynamics – stars: formation

## 1. Introduction

Molecular cores, representing the earliest stages of potential star formation, are crucial for our understanding of the initial conditions of this important process shaping the morphology of galaxies. One approach is to conduct a statistical study of cold dense clumps from unbiased large surveys in the Milky Way. The Planck satellite has carried out the first all-sky survey in the submm-to-mm range, providing a wealth of galactic cold dust cores (Planck Collaboration et al. 2011a). The first release of the all-sky Cold Clump Catalogue of Planck Objects (C3PO) was presented by the Planck Collaboration et al. (2011c). This comprehensive catalog profiles 10,342 distinctive cold sources that stand out against a warmer background. Within the collection of C3PO clumps, a subset of 915 Early Cold Cores (ECCs) was identified using specific criteria, namely a signal-to-noise ratio (S/N) greater than 15 and color temperatures below 14 K. The S/N is based on one of the four matched multi-frequency filter (MMF) algorithms (Planck Collaboration et al. 2011b; Melin et al. 2012).

This particular ECC sample is included as part of the Planck Early Release Compact Source Catalogue (ERCSC), as presented by the Planck Collaboration et al. (2011b). The Planck Collaboration et al. (2016) released the Planck Catalog of Galactic cold clumps (PGCCs) with 13188 sources as the full version of the ECC catalog. These sources, found in various environments, are useful for investigating the initial conditions of star formation, including dynamic processes and the evolution of cores in molecular clouds, making use of their characteristic low temperatures and low levels of activity (Juvela et al. 2010,

2012; Liu et al. 2012; Tatematsu et al. 2020; Kim et al. 2020; Fehér et al. 2022).

Plenty of works have been dedicated to the PGCCs using different molecular spectral lines. The Purple Mountain Observatory (PMO) 14m telescope was used to observe <sup>12</sup>CO, <sup>13</sup>CO, and C<sup>18</sup>O transitions in multiple regions. Specifically, 674 cores in Planck cold clumps of the ECCs were observed (Wu et al. 2012), along with 71 cores in Taurus, Perseus, and in the California nebula (Meng et al. 2013), 51 cores in Orion (Liu et al. 2012), 96 cores in the second quadrant (Zhang et al. 2016), 65 cores in the first Quadrant, and 31 cores in the Anti-Center direction region (Zhang et al. 2020). Additionally, the  $J = 1-0$  transitions of HCO<sup>+</sup> and HCN (Yuan et al. 2016) as well as C<sub>2</sub>H  $N = 1-0$  and N<sub>2</sub>H<sup>+</sup>  $J = 1-0$ , were observed toward the 621 CO selected cores (Liu et al. 2019). Two large projects were also conducted to study PGCCs systematically: the Taeduk Radio Astronomy Observatory (TRAO) mapped the  $J = 1-0$  transitions of <sup>12</sup>CO and <sup>13</sup>CO, while the James Clerk Maxwell Telescope (JCMT) surveyed the 850  $\mu\text{m}$  continuum emission of more than 1000 PGCCs selected from the TRAO sample in the SCUBA-2 Continuum Observations of Pre-protostellar Evolution (SCOPE) project (Liu et al. 2018). Further studies of several molecular species toward subsets of the SCOPE objects were made using the SMT 10m, KVN 21m, Atacama Large Millimeter/submillimeter Array, SMA, NRO 45m and Effelsberg 100m telescopes (Liu et al. 2016; Tatematsu et al. 2017, 2020; Kim et al. 2020; Fehér et al. 2022). Based on these studies above, it has been discovered that PGCCs demonstrate a state of

quiescence and are often believed to represent the earliest stage of star formation.

To characterize the physical properties of the interior of these objects in a large, relatively unbiased sample, observations in dense gas tracers are crucial. Ammonia ( $\text{NH}_3$ ) has been established as a reliable dense gas tracer of molecular clouds (e.g., Ho & Townes 1983; Walmsley & Ungerechts 1983; Danby et al. 1988). Specifically,  $\text{NH}_3$  (1,1) and (2,2), both belonging to the para-species of ammonia, have been proven to be excellent thermometers at  $T_{\text{kin}} < 40$  K (Walmsley & Ungerechts 1983). Additionally, the critical densities of  $\text{NH}_3$  (1,1) and (2,2) are about  $10^3 \text{ cm}^{-3}$  (Evans 1999; Shirley 2015), making them a suitable tracer for dense regions and suffering from minimal freeze-out (Bergin & Tafalla 2007). Therefore, we present a pilot study of  $\text{NH}_3$  (1,1), and (2,2) towards ECCs in different environments, complemented by archival CO data, and calculate the characteristics of these cold cores. Fehér et al. (2022) conducted a study of PGCCs using the Effelsberg 100m radio antenna to observe the  $\text{NH}_3$  (1,1) and (2,2) lines as a supplement to SCOPE targets. The selection of regions for observation was based on two main criteria. Preference was given to regions covered by Herschel observations and to regions characterized by high column density clumps (Liu et al. 2018). In contrast to the SCOPE targets, our sample consists of the whole ECC sample obtained under good observational conditions.

This paper presents a survey of Planck Early Release Cold Cores (ECCs) using ammonia lines, conducted with the Nanshan 26-m telescope. In Sect. 2, we provide a detailed description of the sample and observations. In Sect. 3, we describe the sample properties, and in Sect. 4 we present the results of our survey. In Sect. 5, a comprehensive discussion of the data is given. Our main findings are summarized in Sect. 6.

## 2. Samples, observations and data reduction

### 2.1. The sample

To ensure optimal observational conditions, we carefully chose cold cores from the 915 Planck Early Release Cold Cores (ECCs) dataset (as previously mentioned in Sec. 1). Specifically, we focused on ECCs with a declination above  $-30$  degrees (to observe with a sufficiently high elevation for the Nanshan 26-m telescope). As a result of this selection process, our dataset comprises a total of 672 sources, achieved after the exclusion of sources situated within the Galactic center region, where Galactic longitudes fell within  $|l| \leq 5^\circ$ . These exclusions were made due to the complex interstellar medium environment and intense stellar activity prevalent in the central region of the Milky Way (Ao et al. 2013; Ginsburg et al. 2016; Immer et al. 2016). By removing these sources, we aimed to mitigate the potential biases introduced by the unique environment of the Galactic center and obtain a more representative sample of dense cores that better reflect their characteristics in other regions of the galaxy. Subsequently, our observations were conducted with  $\text{NH}_3$  lines using the Nanshan 26-m telescope. The selected sources are listed in Table A.4 of Appendix A and shown in the top panel of Fig. 1.

Previous investigations have explored extensive sets of individual sources employing ammonia as a probe to examine the dense cores within molecular clouds (Jijina et al. 1999; Sridharan et al. 2002; Rosolowsky et al. 2008; Dunham et al. 2011; Wienen et al. 2012; Svoboda et al. 2016). By conducting a cross-match analysis with these surveys, we identified 27 our sources that overlap with the sample that has been previously detected in ammonia surveys. We also conducted a cross-

match analysis with Planck cold cores observed in ammonia (Fehér et al. 2022): Only six of our sources have been previously observed in ammonia survey specifically targeting Planck cold cores.

### 2.2. $\text{NH}_3$ observations

We conducted single-point observations of  $\text{NH}_3$  (1,1), and (2,2) lines from March 2017 to August 2018 using the Nanshan 26-m telescope. A 22.0-24.2 GHz dual polarization channel superheterodyne receiver was employed, with the rest frequency centered at 23.708 GHz to simultaneously observe  $\text{NH}_3$  (1,1) (23.694 GHz) and (2,2) (23.723 GHz).

To convert antenna temperatures  $T_A^*$  into main beam brightness temperatures  $T_{\text{MB}}$ , a beam efficiency of  $\sim 0.59$  was adopted (Wu et al. 2018), with  $T_{\text{MB}}$  uncertainty about 14%. The telescope is equipped with a dual-input Digital Filter Bank (DFB) system with 8192 channels. The typical system temperature is  $\sim 50$  K ( $T_A^*$  scale) at 23.708564 GHz. The FWHM beam of the telescope is  $115''$  obtained from point-like continuum calibrators, and the bandwidth is 64 MHz, resulting in a channel spacing of  $0.098 \text{ km s}^{-1}$ . All velocities are with respect to the Local Standard of Rest (LSR). The total integration time for each on- and off-position was 360 s, with some sources requiring multiple observations to increase the signal-to-noise ratio (S/N). All observations were obtained under good weather conditions and above an elevation of  $30^\circ$ , resulting in a typical RMS noise level of  $\sim 20$  mK.

### 2.3. CO archival data

In this study we also utilized the  $J=1-0$  transitions of  $^{12}\text{CO}$ ,  $^{13}\text{CO}$ , and  $\text{C}^{18}\text{O}$  from the PMO (Liu et al. 2012; Meng et al. 2013; Zhang et al. 2016, 2018, 2020). The  $3\times 3$  beam sideband separation Superconduction Spectroscopic Array Receiver system was used as the front end (Shan et al. 2012). The Half Power Beam Width (HPBW) is 52 arcsec in the 115 GHz band, with a mean beam efficiency of about 50% and the pointing and tracking accuracies are better than  $5''$ . Fast Fourier Transform Spectrometers (FFTSs) were used with each FFTS providing 16384 channels and a total bandwidth of 1 GHz. The channel spacing is  $\sim 0.16 \text{ km s}^{-1}$  for  $^{12}\text{CO}$ ,  $^{13}\text{CO}$  and  $\text{C}^{18}\text{O}$ . The On-The-Fly (OTF) observing mode was applied, with the antenna continuously scanning a region of  $22' \times 22'$  centered on each clump, while only the central  $14' \times 14'$  regions were used due to the noisy edges of the OTF maps.

After matching the spatial resolution of previous PMO mapping observations (Liu et al. 2012; Meng et al. 2013; Zhang et al. 2016, 2018, 2020) with that of the ammonia data ( $2'$ ), we extracted the spectra of the  $J = 1 - 0$  transitions of  $^{12}\text{CO}$ ,  $^{13}\text{CO}$ , and  $\text{C}^{18}\text{O}$  at the  $2' \times 2'$  peak position of each source in our sample to construct a data set. In the PMO observations, 195 sources match our  $\text{NH}_3$  detected sub-sample (see Sect. 4.1).

### 2.4. Data reduction

The data reduction was performed using the CLASS package of GILDAS<sup>1</sup>, and the python plot packages matplotlib (Hunter 2007). The  $\text{NH}_3$  data were spectrally smoothed to better compare and analyze these together with the CO data, resulting in a velocity resolution of  $0.16 \text{ km s}^{-1}$ . A feature was considered a genuine detection when the signal-to-noise ratio (S/N) was above 3. To

<sup>1</sup> <http://www.iram.fr/IRAMFR/GILDAS/>

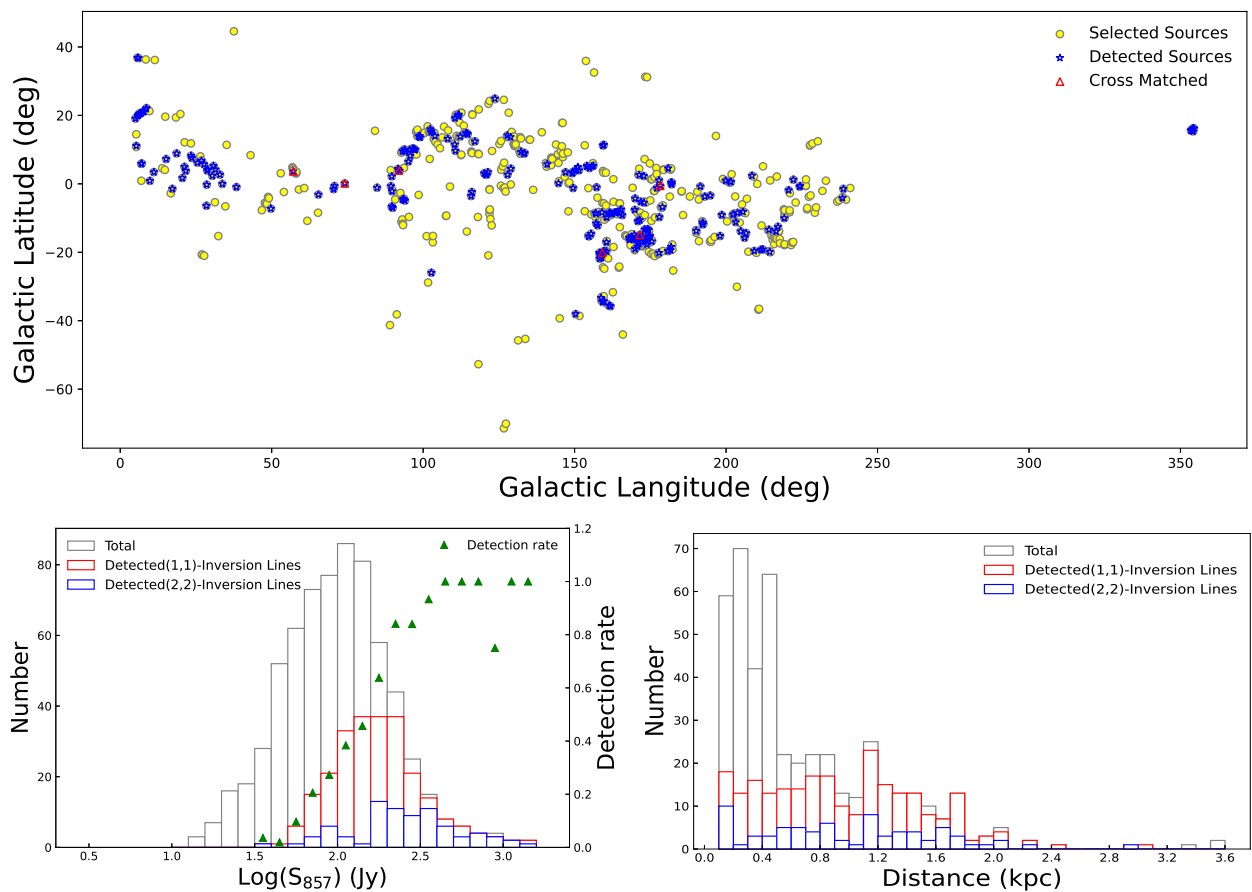


**Fig. 1.** *Top panel:* The distribution of observed cores in the Galactic plane. The selected cores with and without detections of NH<sub>3</sub> emission lines are denoted by blue and yellow circles, respectively. The red triangles denote Planck sources not only being part of our sample but having also been previously detected in ammonia by Fehér et al. (2022). *Lower left:* Detection rate distribution of NH<sub>3</sub> emission lines. The grey histogram represents the whole sample of 672 sources where we searched for NH<sub>3</sub> lines. The red histogram represents the number of sources that we detected in the NH<sub>3</sub> (1,1) line and the blue histogram refers to sources we also detected in the NH<sub>3</sub> (2,2) line. The green triangles denote the detection rate for a given 857  $\mu\text{m}$  flux density. *lower right:* Distribution of distances. Here the grey histogram also refers to the entire sample, while the red histogram visualizes those sources detected in NH<sub>3</sub> (1,1). The blue histogram refers to sources we also detected in the NH<sub>3</sub> (2,2) line.

convert hyperfine blended line widths to intrinsic line widths in the NH<sub>3</sub> inversion spectrum (e.g., Barranco & Goodman 1998), we also fitted the averaged spectra using the GILDAS built-in “NH<sub>3</sub> (1,1)” fitting method which can fit all 18 hyperfine components simultaneously. From this NH<sub>3</sub> (1,1) fit we can obtain integrated intensity, line center velocity, intrinsic line widths of individual hyperfine structure (hfs) components, and optical depth (see Table A.2) of Appendix A.

Main beam brightness temperatures  $T_{\text{MB}}$  are obtained from GAUSS fit. Because the hyperfine satellite lines of the NH<sub>3</sub> (2,2) transition are mostly weak, NH<sub>3</sub> (2,2) optical depths are not determined. A single Gaussian profile was fitted to the main group of NH<sub>3</sub> (2,2) hyperfine components. A total of eight NH<sub>3</sub> cores were fitted with two velocity components. The spectral line of each distinguishable component was fitted with Gaussian and “NH<sub>3</sub>(1,1)” fittings. These components are denoted by the labels “a” and “b” appended to the respective source names, as presented in Table A.2. We treated these two velocity components as separate entities (i.e., plotted them as two distinct cores). However, most of the cores in our observations required only a single velocity component fit. Physical parameters of the dense gas such as rotational temperature ( $T_{\text{rot}}$ ), kinetic temperature ( $T_{\text{kin}}$ ), and NH<sub>3</sub> column density ( $N_{\text{NH}_3}$ ) were derived (see Sects. 3.2 and 3.3). Fig. 2 provides examples of reduced and cal-

ibrated spectra of NH<sub>3</sub> (1,1), and (2,2) inversion lines. Examples for typical ammonia spectrum in different S/N ratios are shown in Fig. B.1 of Appendix B

For the <sup>12</sup>CO, <sup>13</sup>CO and C<sup>18</sup>O spectra, peak main-beam brightness temperature, Local Standard of Rest (LSR) velocities, and line widths have been obtained by fitting Gaussian profiles (see Table C.1 of Appendix C). The excitation temperature for CO ( $T_{\text{ex(CO)}}$ ), <sup>13</sup>CO opacity ( $\tau_{^{13}\text{CO}}$ ), C<sup>18</sup>O opacity ( $\tau_{\text{C}^{18}\text{O}}$ ), <sup>13</sup>CO column density ( $N_{^{13}\text{CO}}$ ), C<sup>18</sup>O column density ( $N_{\text{C}^{18}\text{O}}$ ), and hydrogen column density ( $N_{\text{H}_2}$ ) were also calculated (see Table C.2 of Appendix C).

### 3. Sample properties

#### 3.1. Distances

The distances of our sources were obtained from the literature (Wu et al. 2012; Planck Collaboration et al. 2016). For sources whose distances were unavailable in the literature, we employed the distance with the highest probability from the parallax-based distance estimator of the Bar and Spiral Structure Legacy Survey (Reid et al. 2016). The histogram of the kinematic distances is presented in the *lower right panel* of Fig. 1. It can be deduced from the distance distribution that the NH<sub>3</sub>(1,1) detection rate is

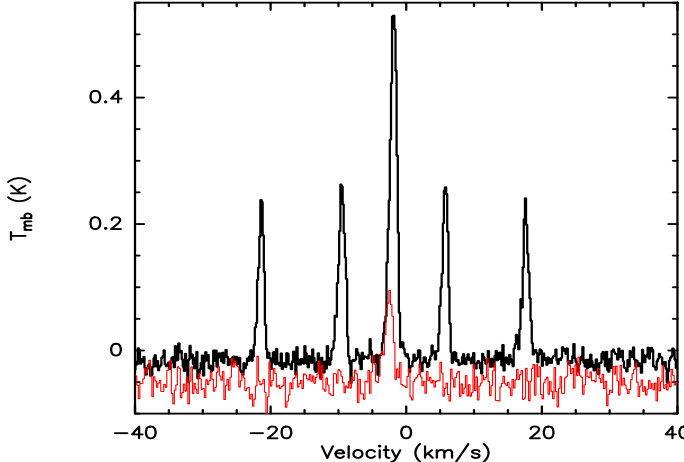


**Fig. 2.** Example for a typical ammonia spectrum. Shown are NH<sub>3</sub> inversion lines from G092.26+03.8. The solid black line represents the observed NH<sub>3</sub> (1,1) spectrum and the solid red line indicates the corresponding NH<sub>3</sub> (2,2) profile.

significantly increased beyond 0.6 kpc, and the NH<sub>3</sub>(2,2) detection rate does not exhibit a clear correlation with distance. The distances of all sources range from 0.11 to 4.09 kpc, with a mean of 0.98 kpc and a median of 0.94 kpc. 56% of the sources have distances within 0.5 and 1.5 kpc.

### 3.2. Kinetic temperature

With the measured data, the rotational temperature ( $T_{\text{rot}}$ ), kinetic temperature ( $T_{\text{kin}}$ ), NH<sub>3</sub> column density ( $N_{\text{NH}_3}$ ), thermal velocity dispersion  $\sigma_{\text{Therm}}$ , non-thermal velocity dispersion  $\sigma_{\text{NT}}$ , thermal-to-non-thermal pressure ratio  $R_p$ , thermal sound speed  $c_s$  and Mach number ( $\mathcal{M}$ ) of cores can be calculated.

Once the optical depth is determined by the "NH<sub>3</sub>(1,1)" fitting as described in Sect 2.4, we can calculate the excitation temperature of the NH<sub>3</sub>(1,1) inversion transition through the relation (Ho & Townes 1983),

$$T_{\text{ex}} = \frac{T_{\text{MB}(1,1)}}{(1 - \exp(-\tau))} + 2.7 \text{ K}, \quad (1)$$

where  $T_{\text{MB}}$  and  $\tau$  represent the temperature and the optical depth of the (1,1) line derived using the GILDAS built-in 'GAUSS' and 'NH<sub>3</sub>(1,1)' fitting methods. A histogram of the optical depths of the (1,1) lines for our positions with NH<sub>3</sub>(1,1) signal-to-noise ratios  $> 3\sigma$  is summarized in Fig. 3b.

Since the relative populations of the  $K = 1$  and 2 ladders of NH<sub>3</sub> are not directly connected radiatively, they are highly sensitive to collisional processes. This allows us to use them as a thermometer of the gas kinetic temperature. The method described in Ho & Townes (1983), has been used to obtain the rotation temperature.

The rotation temperature is given by the expression

$$T_{\text{rot}} = \frac{-41.5}{\ln\left(\frac{-0.282}{\tau} \ln\left(1 - \frac{T_{\text{MB}(2,2)}}{T_{\text{MB}(1,1)}} (1 - \exp(-\tau))\right)\right)} \text{ K}, \quad (2)$$

where  $T_{\text{MB}}$  (2,2) is the main beam brightness temperatures of the (2,2) line derived using the GILDAS built-in 'GAUSS' fitting method.

We estimated the kinetic temperature  $T_{\text{kin}}$  using the approximation of Tafalla et al. (2004) :

$$T_{\text{kin}} = \frac{T_{\text{rot}}(1,2)}{1 - \frac{T_{\text{rot}}(1,2)}{41.5} \ln\left(1 + 1.1 \exp\left(\frac{-16}{T_{\text{rot}}(1,2)}\right)\right)} \text{ K}, \quad (3)$$

where the energy gap between the (1,1) and (2,2) states is  $\Delta E_{12} = 41.5$  K. This approximation has been derived with Monte Carlo models and provides an accuracy of 5% in the range between 5 and 20 K. Most of our sources can be found in this interval.

### 3.3. NH<sub>3</sub> column density

Computing the ammonia column density requires the optical depth and line width of the (1,1) inversion transition along with the rotational temperature, which is obtained from Eqs. (2). As the optical depth and the rotational temperature depend only on line ratios, the resulting column density is a source-averaged quantity.

Realistically assuming that for our cold sources, the bulk of the ammonia populations resides in the metastable ( $J = K$ ), ( $J,K = (0,0)$  to  $(3,3)$ ) levels, the total NH<sub>3</sub> column densities can be calculated from NH<sub>3</sub>(1,1) following (Wienen et al. 2012),

$$N_{\text{NH}_3} \approx N(1,1) \left( \frac{1}{3} \exp\left(\frac{23.1}{T_{\text{rot}}(1,2)}\right) + 1 + \frac{5}{3} \exp\left(-\frac{41.2}{T_{\text{rot}}(1,2)}\right) + \frac{14}{3} \exp\left(-\frac{99.4}{T_{\text{rot}}(1,2)}\right) \right) \text{ cm}^{-2} \quad (4)$$

and

$$N(1,1) = 6.60 \times 10^4 \Delta v \tau \frac{T_{\text{rot}}}{\nu} \text{ cm}^{-2}, \quad (5)$$

where  $N(1,1)$  is the column density of the NH<sub>3</sub>(1,1) transition, the FWHM line width  $\Delta v$  is in km s<sup>-1</sup>, the line frequency  $\nu$  is in GHz, and the rotational temperature  $T_{\text{rot}}$  is in Kelvin.

### 3.4. Velocity dispersions, sound speed, and gas pressure ratio

The observed line widths provide a measure of the internal motions within each Planck source. Here we computed non-thermal velocity dispersion ( $\sigma_{\text{NT}}$ ), thermal velocity dispersion ( $\sigma_{\text{TH}}$ ), and sound speed ( $c_s$ ) following Levshakov et al. (2014), Tang et al. (2017, 2018a,b, 2021).

$$\sigma_{\text{NT}} = \sqrt{\sigma_v^2 - \sigma_{\text{TH}}^2} \text{ km s}^{-1}, \quad (6)$$

where  $\sigma_v = \Delta v(1,1)/8\ln(2)$ , and  $\sigma_{\text{TH}} = (k_B T_{\text{kin}}/17m_H)^{1/2}$ .  $m_H$  is the mass of a single hydrogen atom, and  $k_B$  is the Boltzmann constant.

The thermal sound speed can be calculated with

$$c_s = \sqrt{\frac{k_B T_{\text{kin}}}{\mu m_H}} \text{ km s}^{-1}. \quad (7)$$

where  $\mu = 2.37$  is the mean molecular weight for molecular clouds (Dewangan et al. 2016).

We also calculated the thermal-to-nonthermal pressure ratio ( $R_p = \sigma_{\text{TH}}^2/\sigma_{\text{NT}}^2$ ; Lada et al. 2003) and Mach number (given as  $\mathcal{M} = \sigma_{\text{NT}}/c_s$ ).

The statistical properties of the sample are summarised in Table 1 including the mean values and the medians of the derived quantities, as well as the minimal and maximal values. The

derived values of  $T_{\text{ex}}$ ,  $T_{\text{rot}}$ ,  $T_{\text{kin}}$ ,  $N_{\text{tot}}$ ,  $\sigma_{\text{TH}}$ ,  $\sigma_{\text{NT}}$ ,  $c_s$ ,  $\mathcal{M}$  and  $R_p$  for individual Planck sources are listed separately in Table A.2 of Appendix A.

## 4. Results

### 4.1. $\text{NH}_3$ detection rates

Out of the 672 Planck Early Release Cold Cores (ECCs) that were surveyed with the Nanshan 26-m telescope for  $\text{NH}_3$ , 249 sources (37%) were detected with  $\text{NH}_3$  (1,1) emission lines. Of these, 187 sources reveal  $\text{NH}_3$  (1,1) hyperfine structure, while 76 sources (11%) also show  $\text{NH}_3$  (2,2) emission lines. Observed parameters and calculated parameters are given in Tables A.2–A.3 of Appendix A.

The highest angular resolution of the Planck survey is 5 arcmin, at a frequency of 857 GHz. We plotted the distribution of observed sources and the  $\text{NH}_3$  lines detected in this work as well as the detection rate of the  $\text{NH}_3$  (1,1) line as a function of the 857 GHz aperture flux density  $S_{857}$  of the Planck Sources in the *lower left panel* of Fig. 1. We observe that sources with  $S_{857}$  larger than 3 Jy have a 100% detection rate. Furthermore, the detection rate of the  $\text{NH}_3$  (1,1) line increases from 0 to 100 percent as the flux density  $S_{857}$  rises from 1.5 to 4.6 Jy. However, it should be noted that while the detection rates of the  $\text{NH}_3$  (1,1) line are 100 percent in the last bins, the number of sources within these bins is limited, with only 8, 6, 4, 3, 2, and 2 sources in total.

In the *lower right panel* of Fig. 1, we observed an unexpectedly low detection rate of ammonia in regions with small kinematic distances. To understand this phenomenon, we performed a column density analysis of sources situated within a distance of less than 0.45 kpc. Utilizing hydrogen column density data from the [Planck Collaboration et al. \(2011c\)](#), we found a difference in column densities between sources where ammonia was detected and those where it was not, within this near distance (less than 0.45 kpc). Specifically, sources with detected ammonia exhibited an average hydrogen column density of  $4.32 \times 10^{21} \text{ cm}^{-2}$ , while those without ammonia detection had an average hydrogen column density of  $1.99 \times 10^{21} \text{ cm}^{-2}$ . Moreover, it's important to consider that sources in these nearby regions may have relatively extended spatial distributions. This spatial extension implies that during our observations of ammonia point sources, we may inadvertently miss the real peaks of the Planck cold cores.

The top panel of Fig. 1 presents the spatial distribution of the detected sources, which are mainly located in local star-forming regions such as Taurus and Orion and the galactic plane. This trend is shared by all of the ECCs and CO-selected cores in the sample ([Wu et al. 2012; Yuan et al. 2016](#)). As mentioned in Sect. 2.1, we cross-matched our sample with sources observed by [Fehér et al. \(2022\)](#), owing to distinct criteria detailed in Section 1. Consequently, there is a disparity in the distribution of sources across the galaxy between the two samples (see also Sect. 2.1).

### 4.2. Properties of the $\text{NH}_3$ emitting gas

Figure 3 shows the statistics of observed and physical properties for the  $\text{NH}_3$  detected sample. The top left panel shows the intrinsic line width of an individual hfs component,  $\Delta V(\text{NH}_3(1,1))$ , which ranges approximately from 0.36 to  $2.36 \text{ km s}^{-1}$ , with an average of  $0.89 \pm 0.29 \text{ km s}^{-1}$ , which suggests that the non-thermal turbulence of these sources is significant (errors correspond to the standard deviations of the mean throughout this article). The top middle panel of Figure 3 shows the sample optical depths, which range from 0.1 to 5.3 with an average value of

**Table 1.**  $\text{NH}_3$  parameters of our sample of PGCC cores

Parameter	Range	Mean	Median
$\Delta V(\text{NH}_3(1,1)) [\text{km s}^{-1}]$	0.36–2.36	$0.89 \pm 0.29$	0.83
$\tau$	0.1–5.3	$1.6 \pm 1.1$	1.4
$T_{\text{ex}} [\text{K}]$	2.8–5.4	$3.2 \pm 0.4$	3.1
$T_{\text{rot}} [\text{K}]$	8.6–17.6	$11.4 \pm 2.2$	10.7
$T_{\text{kin}} [\text{K}]$	8.9–20.7	$12.3 \pm 2.9$	11.4
$N_{\text{NH}_3} [10^{15} \text{ cm}^{-2}]$	0.36–6.07	$2.04 \pm 1.2$	1.83
$\sigma_{\text{TH}} [\text{km s}^{-1}]$	0.07–0.10	$0.08 \pm 0.01$	0.07
$\sigma_{\text{NT}} [\text{km s}^{-1}]$	0.30–1.09	$0.55 \pm 0.18$	0.49
$c_s [\text{km s}^{-1}]$	0.18–0.27	$0.21 \pm 0.02$	0.20
$\mathcal{M}$	1.6–5.0	$2.7 \pm 0.8$	2.5
$R_p$	0.01–0.06	$0.02 \pm 0.01$	0.02
$N_{\text{H}_2}(^{13}\text{CO}) [10^{22} \text{ cm}^{-2}]$	0.07–2.88	$0.74 \pm 0.42$	0.63
$\chi_{\text{NH}_3} [10^{-7}]$	0.3–9.7	$2.7 \pm 2.2$	1.9
$T_{\text{dust}} [\text{K}]$	8.6–13.9	$11.5 \pm 1.07$	11.6

**Notes.** The dust temperature ( $T_{\text{dust}}$ ) values presented in this table correspond to a cross-matching of  $\text{NH}_3$ -detected 249 sources with the dust temperature data obtained from [Planck Collaboration et al. \(2016\)](#).

1.6, implying that  $\text{NH}_3$  (1,1) lines in most of the detected PGCC cores are optically thick (see Table 1).

The top right panel shows the excitation temperature,  $T_{\text{ex}}$ , which ranges approximately from 2.8 to 5.4 K, with a mean and median of 3.2 and 3.1 K, respectively. The bottom left panel of Figure 3 shows the derived rotational temperature, which exhibits a range of 8.6 to 17.6 K, with an average value of  $11.4 \pm 2.2$  K. The median value of the rotational temperature is 10.7 K, with a typical value of approximately 10 K. Remarkably, 83% of the sources exhibit values lying between 8 and 14 K. The  $\text{NH}_3$  kinetic temperature distribution, illustrated in the *bottom middle panel* of Fig. 3, ranges from 8.9 to 20.7 K, with an average of  $12.3 \pm 2.9$  K and a median value of 11.4 K. The total  $\text{NH}_3$  column density ranges from 0.36 to  $6.07 \times 10^{15} \text{ cm}^{-2}$ , with an average of  $2.04 \times 10^{15} \text{ cm}^{-2}$ . The total column densities of  $\text{NH}_3$  are presented as a histogram in the *bottom right panel* of Fig. 3, exhibiting a peak around  $10^{15.4} \text{ cm}^{-2}$  in our sample.

The thermal velocity dispersion of  $\text{NH}_3$  (1,1) lines detected at a  $>3\sigma$  level shows a range of 0.07 to  $0.10 \text{ km s}^{-1}$ , with an average of  $0.08 \pm 0.01 \text{ km s}^{-1}$  and a median of  $0.07 \text{ km s}^{-1}$ . The non-thermal velocity dispersion of  $\text{NH}_3$  (1,1) for cores ranges from 0.30 to  $1.09 \text{ km s}^{-1}$ , with an average of  $0.55 \pm 0.18 \text{ km s}^{-1}$  and a median of 0.49  $\text{km s}^{-1}$ . The thermal linewidth is significantly smaller than the non-thermal linewidth, which suggests that non-thermal motions dominate the dense gas in the PGCCs. The sound speed of the gas ranges from 0.18 to  $0.27 \text{ km s}^{-1}$ , with an average of  $0.21 \pm 0.02 \text{ km s}^{-1}$  and median of  $0.20 \text{ km s}^{-1}$ . The thermal to non-thermal pressure ratio in the gas traced by  $\text{NH}_3$  (1,1) ranges from 0.01 to 0.06, with an average of  $0.02 \pm 0.01$ , and a median of 0.02. The Mach number ranges from 1.6 to 5.0 with an average of  $2.7 \pm 0.8$ , and a median of 2.5.

### 4.3. Thermal and non-thermal motions

The clumps are supported against their gravity by both thermal and non-thermal motions ([Cho & Lazarian 2003](#)). The former is a manifestation of the kinetic temperature within a clump, while the latter originates from star-forming activities such as infall motions and outflows that can broaden the non-thermal velocity dispersion. However, the quiescent nature of PGCCs suggests that these motions are not particularly vigorous. Therefore, turbulent motion is the primary contributor to the non-thermal mo-

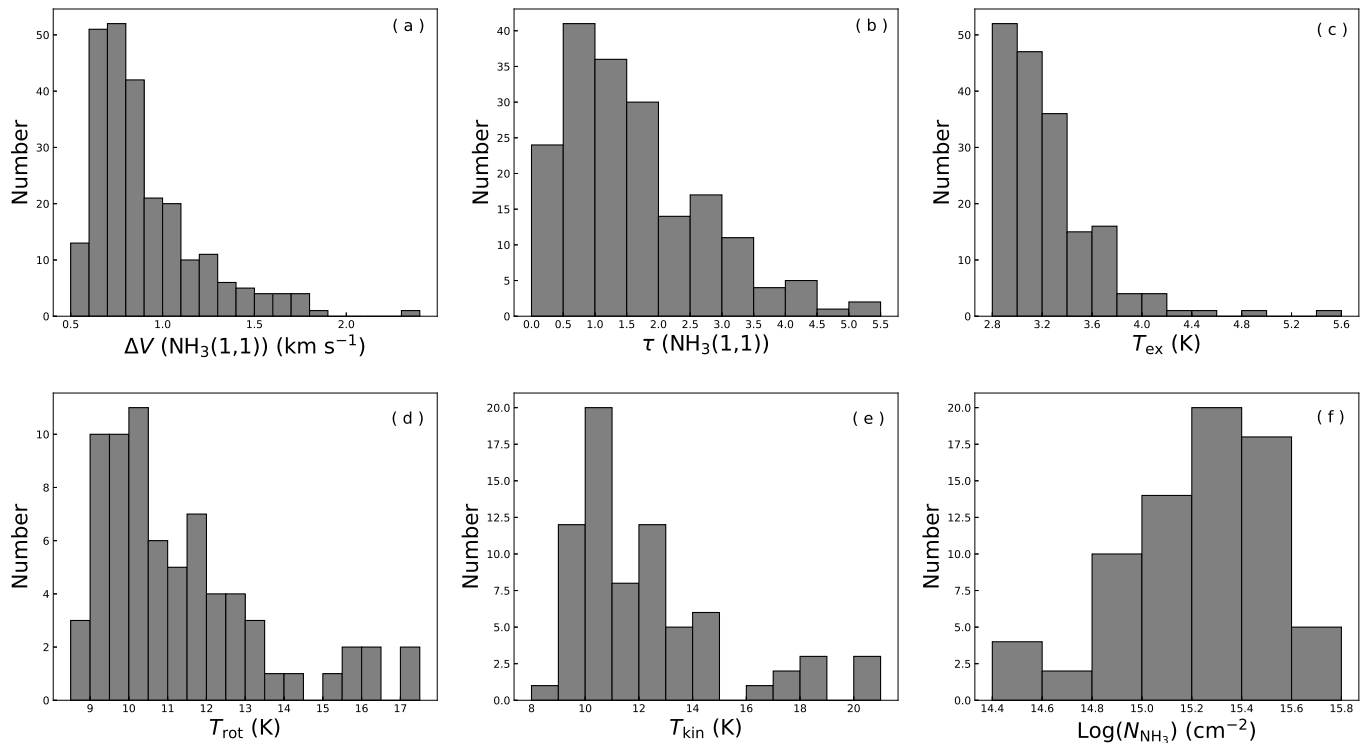


**Fig. 3.** Histograms of physical parameters derived from  $\text{NH}_3$ . (a) Intrinsic line widths of individual  $\text{NH}_3(1,1)$  hyperfine structure components with hyperfine structure and a peak line flux threshold of  $3\sigma$ ; (b) peak optical depths of the main group of hf components  $\tau_m(1,1)$  for those positions with  $\text{NH}_3(1,1)$  hyperfine structure and  $S/N > 3$  (these line widths and peak optical depths are derived from the GILDAS built-in “ $\text{NH}_3(1,1)$ ” fitting method); (c) excitation temperature  $T_{\text{ex}}$ ; (d) rotational temperature  $T_{\text{rot}}$ ; (e) kinetic temperature  $T_{\text{kin}}$ ; (f)  $\text{NH}_3$  column densities.

tion of these cores. Ammonia is one of the few dense gas tracers that allows for the simultaneous computation of line width and kinetic temperature, as well as thermal and non-thermal line widths. Our data are particularly well-suited for investigating these two types of motion.

When turbulent energy is converted into heat, a correlation is expected to exist between the kinetic temperature and linewidth (Guesten et al. 1985; Molinari et al. 1996; Ao et al. 2013; Ginsburg et al. 2016; Immer et al. 2016; Tang et al. 2017, 2018a,b, 2021). In this study, we investigate the existence of a correlation between temperature and turbulence in PGCCs traced by the dense gas. To achieve this, we utilized the  $\text{NH}_3(1,1)$  and  $(2,2)$  line ratio derived kinetic temperature and  $\text{NH}_3$  non-thermal velocity dispersion ( $\sigma_{\text{NT}}$ ) as a decent approximation proxy for turbulence. The non-thermal velocity dispersions versus the kinetic temperature for the sources are shown in Fig. 4, with the dotted line representing the thermal sound speed. Our results indicate a weak correlation between non-thermal velocity dispersion and kinetic temperature, suggesting that turbulent heating may contribute to gas temperature in these cold cores.

#### 4.4. Associated stellar objects

The associated objects of the cores are crucial for our understanding of their environment and evolutionary stages. Therefore, we investigated the objects associated with the cores, including infrared (IR) objects, young stellar objects (YSOs), and young stellar object candidates (YSO candidates). We obtained the stellar objects from the Simbad website. Statistical properties are given in Tables 2-3. YSOs are distinguished by their manifestation of not only infrared excess but also additional spec-

tral features, providing evidence of active star formation processes (Allen et al. 2004; Gutermuth et al. 2004). Conversely, YSO candidates represent potential YSOs necessitating further scrutiny and validation.

In our study, we adopted the ammonia beam size ( $\sim 2'$ ) as a matching criterion. Among the 672 cores observed, our analysis revealed the presence of 131 ( $\sim 19\%$ ) IR objects, 57 ( $\sim 8\%$ ) YSOs and 58 ( $\sim 8\%$ ) YSO candidates. The rare association may indicate low star formation activity (Lada et al. 2009; Lombardi et al. 2010). However, it cannot be entirely excluded that the associated objects originate from different gas clumps located along the line-of-sight (Wu et al. 2006). It is important to note that certain cores in our sample may encompass multiple IR sources, as well as multiple YSOs or YSO candidates. Notably, the majority of these IR objects correspond to single-point sources detected by the Infrared Astronomical Satellite (IRAS). Overall, our findings indicate that 149 ( $\sim 22\%$ ) cores have different types of associated objects within a beam size of  $\sim 2'$ . Additionally, we find that 112 ( $\sim 17\%$ ) cores contain at least one IR object, 29 ( $\sim 4\%$ ) cores have YSOs, and 23 ( $\sim 3\%$ ) cores contain YSO candidates. Among these, 102 sources only associate with IR objects, 18 cores only associate with YSOs and 16 cores only associate with YSO candidates. 4 cores are associated with both YSOs and YSO candidates, 7 cores with both YSO and IR objects, 3 cores with both IR objects and YSO candidates.

Considering the 249 cores where  $\text{NH}_3(1,1)$  emission was detected, we find 66 ( $\sim 27\%$ ) IR objects, 48 ( $\sim 19\%$ ) YSOs, and 52 ( $\sim 21\%$ ) YSO candidate sources associated with these cores using the aforementioned  $\sim 2'$  criterion. In general, 80 ( $\sim 32\%$ ) cores have different types of associated objects. Additionally, we find that 53 ( $\sim 21\%$ ) cores contain at least one IR object, 23 ( $\sim 9\%$ ) cores host YSOs, and 17 ( $\sim 7\%$ ) cores harbor YSO

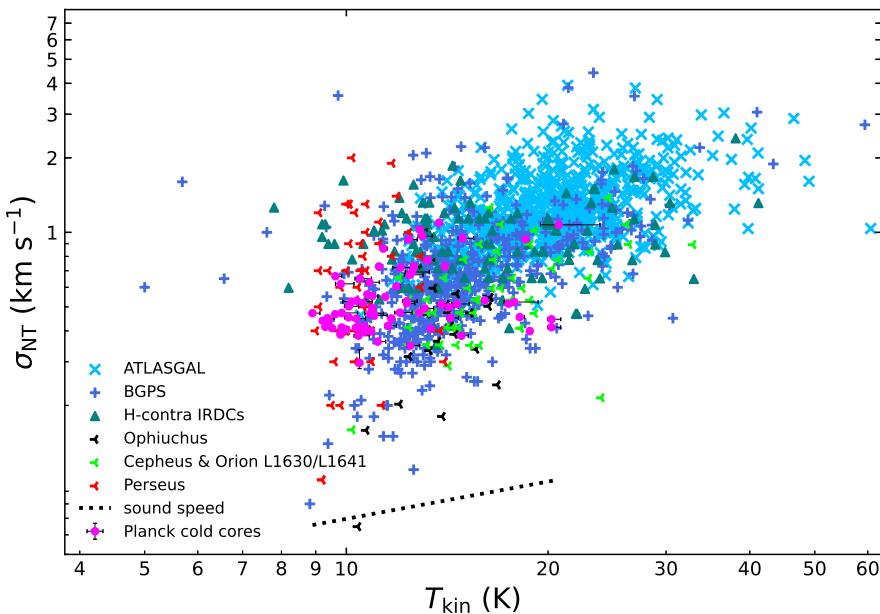


**Fig. 4.** Left: Non-thermal velocity dispersion  $\sigma_{NT}$  vs. gas kinetic temperature derived from NH<sub>3</sub> (1,1). The black dotted line at the bottom represents the thermal sound speed (*left*).

**Table 2.** Numbers of associated stellar objects

Types of matched cores	Matching criteria	Number of associated stellar objects			Number of cores containing stellar objects		
		with IR objects	with YSOs	with YSO candidates	contain IR objects	contain YSOs	contain YSO candidates
		672 observed cores ~2'	131 (~19%)	57 (~8%)	58 (~8%)	112 (~17%)	29 (~4%)
249 NH <sub>3</sub> detected cores	~2'	66 (~27%)	48 (~19%)	52 (~21%)	53 (~21%)	23 (~9%)	17 (~7%)

**Notes.** Matching criteria refer to associated objects within the ~2' ammonia beam size.

**Table 3.** Matching results by types of stellar objects

Types of matched cores	Matching criteria	Single-source matches			Multi-source matches			
		IR	YSO	YSO candidate	YSOs & YSO candidate	IR & YSOs	IR & YSO candidate	IR&YSOs&YSO candidate
		672 observed cores ~2'	102 (~15%)	18 (~3%)	16 (~2%)	4 (~1%)	7 (~1%)	3 (~1%)
249 NH <sub>3</sub> detected cores	~2'	45 (~18%)	13 (~5%)	9 (~4%)	5 (~2%)	5 (~2%)	3 (~1%)	

**Notes.** "Single-source matches" are sources that are exclusively associated with either an IR source or with one specific type of stellar object. "Multi-source matches" refer to sources that are associated with multiple types.

candidates. 45 sources only associate with IR objects, 13 cores only associate with YSOs and 9 cores only associate with YSO candidates. 5 cores are associated with both YSOs and YSO candidates, 5 cores with both YSOs and IR objects, and 3 cores with both IR objects and YSO candidates.

Based on preliminary statistical analysis, the proportion of sources with NH<sub>3</sub> emission matching IR sources and stellar objects is higher than the overall proportion of the total sample matching IR sources and YSOs. The ammonia detection rate of sources matching young stellar objects or their candidates in the 672 observed cores is 66%, while the ammonia detection rate of sources matching IR objects is 45%. The ammonia detection rate is higher in sources with matching stellar objects. Not all sources with matched stellar objects and IR objects have been detected in NH<sub>3</sub> (1,1). There can be several reasons for this. Firstly, distance plays a significant role. If the YSOs or IR objects are located at a large distance, the faint emission signal from ammonia may

be too weak to be detected. Secondly, the spatial resolution of the observing instrument can also be a factor. Other factors include line-of-sight effects and environmental conditions, where the physical environment surrounding the YSOs may influence the presence of ammonia molecules. The inescapable issue at hand is that our matching could potentially be limited to line-of-sight coincidence, lacking the necessary distance information for spatial alignment.

#### 4.5. NH<sub>3</sub> abundances

The column densities of ammonia in our sample range from 0.36  $\sim 6.07 \times 10^{15} \text{ cm}^{-2}$ , with a mean value of approximately  $2.04 \times 10^{15} \text{ cm}^{-2}$  and a median value of about  $1.83 \times 10^{15} \text{ cm}^{-2}$  (Table 1). We utilized <sup>13</sup>CO to derive the H<sub>2</sub> column densities as described in Appendix C. The H<sub>2</sub> column densities  $N_{\text{H}_2}(^{13}\text{CO})$  range from  $7.0 \times 10^{20}$  to  $2.88 \times 10^{22} \text{ cm}^{-2}$ , with an average of

$7.4 \times 10^{21} \text{ cm}^{-2}$ . The column densities of NH<sub>3</sub> denoted as  $N_{\text{NH}_3}$ , were compared with the column densities of H<sub>2</sub>, denoted as  $N_{\text{H}_2}$ , derived from <sup>13</sup>CO to determine the fractional abundance of ammonia in each source. The fractional abundance,  $\chi_{\text{NH}_3}$ , is defined as the ratio of  $N_{\text{NH}_3}$  to  $N_{\text{H}_2}$ (<sup>13</sup>CO). The ammonia abundances in the sources range from 0.3 to  $9.7 \times 10^{-7}$ , with an average of  $2.7 \times 10^{-7}$ .

Fig. 5 illustrates the column densities of NH<sub>3</sub> and its abundances,  $\chi_{\text{NH}_3}$ , as a function of H<sub>2</sub> column density and kinetic temperature  $T_{\text{kin}}$ . It is observed that the NH<sub>3</sub> column densities and fractional abundances are inversely proportional to the kinetic temperatures. Moreover, there is a trend of decreasing fractional NH<sub>3</sub> abundance,  $\chi_{\text{NH}_3}$ , with increasing  $N_{\text{H}_2}$ .

## 5. Discussion

### 5.1. Column densities and abundances

The ammonia column densities in our results are consistent with the findings of PGCC selected sources from SCUBA-2, whose column densities range from 0.4 to  $1.5 \times 10^{16} \text{ cm}^{-2}$ , with a mean value of approximately  $1.3 \times 10^{15} \text{ cm}^{-2}$  (Fehér et al. 2022). The ammonia column densities we obtained in our observations are also consistent with those reported in most star-forming environments (Dunham et al. 2011; Wienen et al. 2012; Cyganowski et al. 2013).

The average value of  $N_{\text{H}_2}$ (<sup>13</sup>CO),  $7.4 \times 10^{21} \text{ cm}^{-2}$ , is consistent with the results obtained from the Planck cold cores observed by PMO (Wu et al. 2012; Meng et al. 2013; Zhang et al. 2016). In the SCOPE-2 follow-up observations, the H<sub>2</sub> column densities of 97 Planck cold cores range from  $10^{22}$  to  $10^{24} \text{ cm}^{-2}$  (Fehér et al. 2022), which are higher than the column densities obtained in our work. This may be attributed to the fact that the SCOPE-2 survey does not include sources with column densities  $N_{\text{H}_2} < 2 \times 10^{21} \text{ cm}^{-2}$  (Eden et al. 2019).

Previous observations of NH<sub>3</sub> fractional abundance in high-mass star-forming clumps suggest a median value of  $2.7 \times 10^{-8}$  (Urquhart et al. 2015). Additionally, Dunham et al. (2011), Wienen et al. (2012), and Merello et al. (2019) obtained average abundance values of  $1.2 \times 10^{-7}$ ,  $4.6 \times 10^{-8}$ , and  $1.5 \times 10^{-8}$ , respectively, in clumps of the Bolocam Galactic Plane Survey (BGPS), the APEX Telescope Large Area Survey of the GALaxy (ATLASGAL), and the Hi-GAL survey. Furthermore, fractional abundances of  $4 \times 10^{-8}$ ,  $8 \times 10^{-7}$  and  $1 \times 10^{-8}$  were derived for infrared dark clouds by Pillai et al. (2006), Ragan et al. (2011), and Chira et al. (2013), respectively. The average NH<sub>3</sub> abundance derived from PGCCs in this study is one order of magnitude greater than that of MSF regions and IRDCs and exhibits a narrow distribution similar to that of IRDCs. The elevated NH<sub>3</sub> fractional abundance in PGCCs relative to other star-forming regions is likely attributable to the earlier phase of cloud evolution of PGCCs compared to Massive Star-forming (MSF) regions or even IRDCs. Ammonia is more abundant in cold, dense cores than most other molecules (Bergin & Langer 1997). The average NH<sub>3</sub> abundances obtained in our study are consistent with those predicted for low-mass pre-protostellar cores by chemical models (Bergin & Langer 1997).

The NH<sub>3</sub> column densities and fractional abundances are inversely proportional to the kinetic temperatures (see in Fig. 5 a, b), which is consistent with the findings of previous studies on infrared dark clouds (Chira et al. 2013). The NH<sub>3</sub> column densities in all cores tend to increase with  $N_{\text{H}_2}$ , as shown in Fig. 5 (c), following the general trend that the NH<sub>3</sub> emission follows the dust continuum emission in the cores. This is in agreement

with the results reported by Ragan et al. (2011), who found that IRDCs with no evidence of embedded star formation activity exhibit a strong correlation between ammonia and H<sub>2</sub> column density. A similar trend is observed in the cold cores in our observation.

### 5.2. Comparative analysis of thermal and non-thermal motions

To obtain comprehensive statistics on PGCCs, we conducted a comparative analysis of the non-thermal velocity dispersions and kinetic temperatures. Studies encompass a diverse range of samples, including high-mass star-forming clumps at various evolutionary stages from ATLASGAL and BGPS surveys (Dunham et al. 2011; Wienen et al. 2012), high contrast Infrared Dark Clouds (IRDCs) (Chira et al. 2013), as well as starless cores in the Perseus region (Rosolowsky et al. 2008; Schnee et al. 2009), and dense cores in the Ophiuchus, Cepheus, and Orion L1630 and L1641 molecular clouds (Harju et al. 1991, 1993; Friesen et al. 2009). This comprehensive approach allows us to gain valuable insights into the physical properties of these objects and their evolutionary characteristics. In Table 4, we have compiled a list containing the fundamental information of the sources used for comparison in this study.

As seen in Fig. 4, unlike high-mass star-forming clumps and dense cores in star-forming regions (Dunham et al. 2011; Wienen et al. 2012), the relationship between non-thermal velocity dispersion and kinetic temperatures in PGCCs is much weaker, which is similar to or even less than for infrared dark clouds (Chira et al. 2013). Additionally, the distribution of non-thermal velocity dispersion and kinetic temperatures of Planck cold cores is narrower when compared to the observations of the other samples. Spearman's rank correlation coefficients ( $\rho$ ) for non-thermal velocity dispersion versus kinetic temperatures in different samples and the resultant  $\rho$ -values are presented in Table A.5 of Appendix A. The table presents the obtained  $\rho$ -values along with their corresponding P-values. The analysis of this table reveals varying degrees of correlation between non-thermal velocity dispersion and kinetic temperature across different samples. Particularly, a conspicuous positive correlation is discernible in the ATLASGAL, BGPS, Ophiuchus, Cepheus, and Orion L1630/L1641 samples, underscored by small P-values. However, in the High-contrast IRDCs, the correlation is relatively weak, with a Spearman correlation coefficient of 0.07 and a p-value of 0.45, suggesting a weak and non-significant linear relationship between these two variables. The Perseus sample also manifests a relatively weak correlation, featuring a Spearman correlation coefficient of 0.2 and a p-value of 0.16, implying a modest positive correlation trend that lacks statistical significance. In contrast, our Planck cold cores sample displays a pronounced positive correlation between non-thermal velocity dispersion and kinetic temperature. With a Spearman correlation coefficient of 0.33 and a p-value of  $4.00 \times 10^{-3}$ .

Furthermore, gas pressure ratios derived from our results closely align with those obtained by Urquhart et al. (2015), who conducted a study on 66 massive young stellar objects and compact Hii regions from the RMS survey (Red MSX Source survey, Lumsden et al. 2013). Urquhart et al. (2015) obtained gas pressure ratios ( $R_p$ ) of 0.01–0.02 for both massive star-forming and quiescent clumps. In contrast, Lada et al. (2003) reported significantly higher values of  $R_p = 4\text{--}5$  for low-mass star-forming cores, such as Barnard 68, based on C<sup>18</sup>O and C<sup>34</sup>S data. Our sample, which includes non-thermal movements that significantly con-

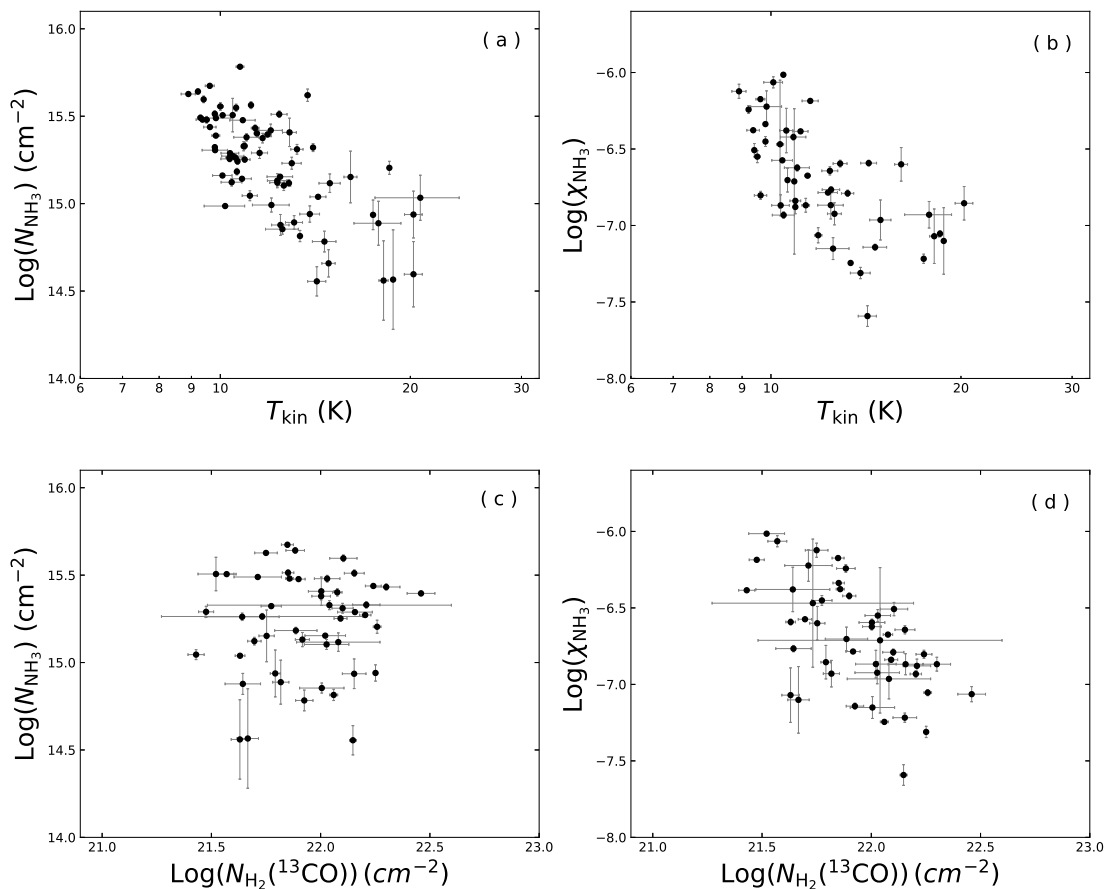


**Fig. 5.** (a,b) Column densities and fractional abundances  $N_{\text{NH}_3}/N_{\text{H}_2}(^{13}\text{CO})$  versus kinetic temperature  $T_{\text{kin}}$  and (c,d) vs. the column density of  $\text{H}_2$  derived from  $^{13}\text{CO}$  ( $N_{\text{H}_2}(^{13}\text{CO})$ ).

**Table 4.** Fundamental information on different  $\text{NH}_3$  samples

Sources	Reference	Type	$\text{NH}_3$ source number
BGPS	Dunham et al. (2011)	High-mass star-forming clumps, at various evolutionary stages	456
ATLASGAL	Wienen et al. (2012)	High-mass star-forming clumps, at various evolutionary stages	752
UC HII Cand High contrast IRDCs	Molinari et al. (1996) Chira et al. (2013)	Precursors of ultracompact HII regions Capable of harbouring high-mass star-forming regions Early evolutionary stages	163 109
High IR extinction clouds	Rygl et al. (2010)	Cold and compact high extinction clouds	54
EGOs	Cyanowski et al. (2013)	Northern extended green objects (EGOs)	94
Ophiuchus	Friesen et al. (2009)	Studies of isolated starless clumps	21
Perseus	Schnee et al. (2009)	Starless cores	49
Cepheus & Orion L1630 / L1641	Harju et al. (1993, 1991)	Warm, massive clumps	51

tribute to the kinetic energy balance, more closely aligns with samples of massive clumps compared to others.

### 5.3. Correlation between $\text{NH}_3$ and other molecular species

In their survey of 674 Planck cold clumps, Wu et al. (2012) discovered that the velocities of transitions from CO and its isotopologues were highly consistent with one another. We plot the absolute value of the difference between  $J=1-0$  transitions of  $^{13}\text{CO}$  and  $\text{C}^{18}\text{O}$  and the  $\text{NH}_3(1,1)$  line-center velocities from Gaussian fits in Fig. 6 (a, b). When multiple  $^{13}\text{CO}$  velocities were detected along the line of sight, we assumed that the velocity component closest to the  $\text{NH}_3$  velocity is associated with the core (Kirk et al. 2007).

The minute discrepancy in centroid velocity between  $\text{NH}_3$  and  $^{13}\text{CO}$  ( $\sim 0.17 \text{ km s}^{-1}$ ), and between  $\text{NH}_3$  and  $\text{C}^{18}\text{O}$  ( $\sim 0.18 \text{ km s}^{-1}$ ), can be compared to the distinction in line-center velocities of  $\text{N}_2\text{H}^+$  and  $\text{C}^{18}\text{O}$  in low-mass, starless, and protostellar cores Walsh et al. (2004); Kirk et al. (2007). Fig. 6 (a, b) illustrate that the majority of cores (64% for the difference between  $^{13}\text{CO}$   $\text{NH}_3(1,1)$  line-center velocities and 70% for the difference between  $\text{C}^{18}\text{O}$  and  $\text{NH}_3(1,1)$  line-center velocities) exhibit differences smaller than the sound speed (dotted lines), and the remaining cores have differences that are not much larger. This phenomenon was investigated in the Perseus molecular cloud by Kirk et al. (2007), who found that the relative motions of dense  $\text{N}_2\text{H}^+$  cores and their envelopes (measured in  $\text{C}^{18}\text{O}$ ) generally exhibit velocity differences lower than thermal mo-

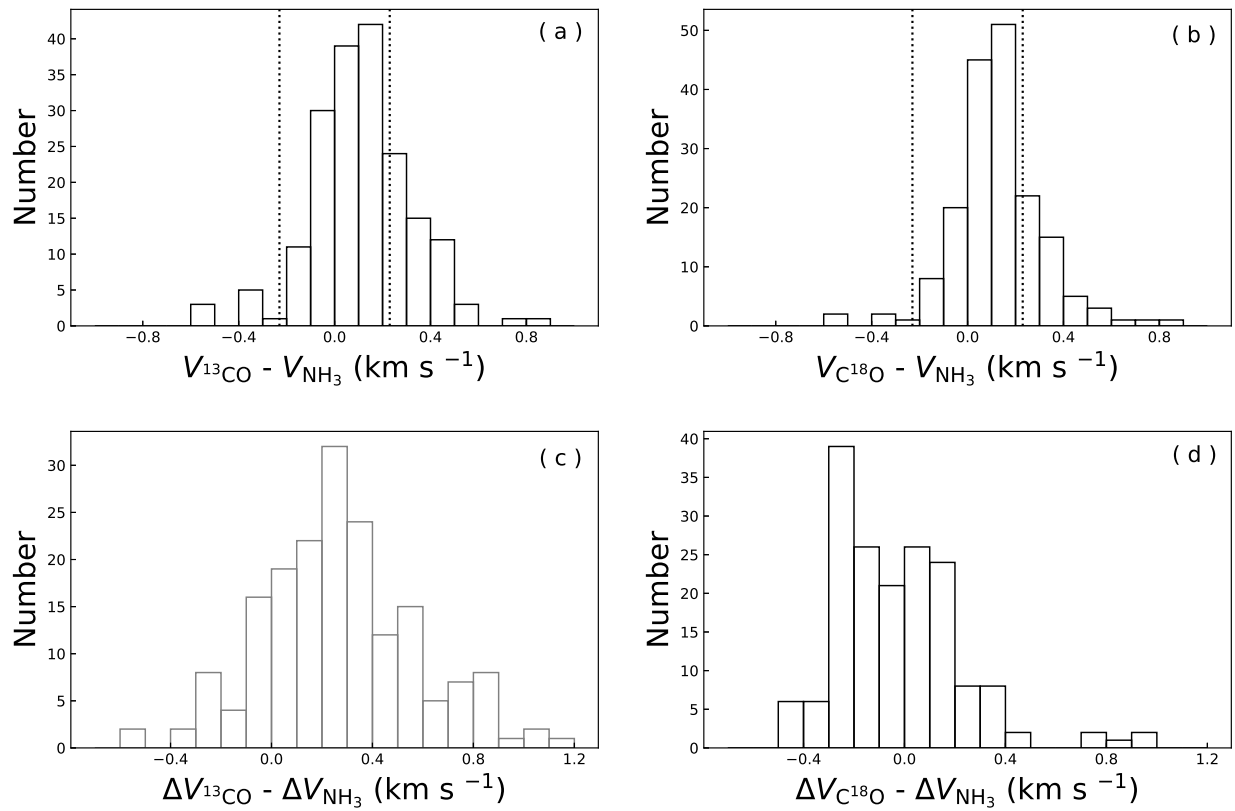


**Fig. 6.** Distributions between differences of line-center velocities (a, b) and line widths (c, d) of <sup>13</sup>CO, C<sup>18</sup>O and NH<sub>3</sub>. The average sound speed is indicated as dotted lines in (a, b).

tions in the majority of cases ( $\sim 90\%$ ). This is also consistent with the findings of Walsh et al. (2004), who measured a core-to-envelope velocity difference that exceeded the sound speed in only 3% of their sample. These samples consisted of isolated low-mass cores. Therefore, these comparisons suggest that the velocity differences between low and high-density tracers in the Planck cores observed by NH<sub>3</sub> are similar to those in low-mass, starless, or prestellar cores. In the survey of CO-selected cores in Planck cold clumps, Yuan et al. (2016) found that the central velocity differences of transitions from <sup>13</sup>CO, HCO<sup>+</sup> and HCN are strikingly consistent with each other. The central velocities (obtained by fitting Gaussian profiles) between <sup>13</sup>CO and HCO<sup>+</sup> ( $V_{^{13}\text{CO}} - V_{\text{HCO}^+}$ ), <sup>13</sup>CO and HCN ( $V_{^{13}\text{CO}} - V_{\text{HCN}}$ ), HCO<sup>+</sup> and HCN ( $V_{\text{HCO}^+} - V_{\text{HCN}}$ ) in their study have mean values of 0.006, 0.05, and 0.002 km s<sup>-1</sup>, respectively. The smaller deviations from Yuan et al. (2016) may indicate that <sup>13</sup>CO, HCO<sup>+</sup>, and HCN are better coupled with each other. It is important to note that the channel spacing employed in their study was 0.21 km s<sup>-1</sup>. In this work, the mean value of the velocity difference among the central velocities of <sup>13</sup>CO and NH<sub>3</sub> is 0.17 km s<sup>-1</sup>, with channel spacing of 0.16 km s<sup>-1</sup>. It is worth noting that the relatively low-velocity resolution might impact the interpretation of the small velocity differences observed in both cases. To address this, future observations with higher resolution would be beneficial for a more accurate comparison. By improving the velocity resolution, we can measure and compare the central velocity differences between different molecular lines more accurately, providing deeper insights. Such observations would help further validate and explain the consistency among these molecular transitions and enhance our understanding of the physical processes occurring within Planck cold clumps. Therefore, future

high-resolution observations will be would help to further validate this matter.

The mean intrinsic line width of the NH<sub>3</sub> (1,1) lines obtained from GAUSS fit is approximately 0.89 km s<sup>-1</sup>, which is comparable to that of C<sup>18</sup>O  $J=1-0$  (0.8 km s<sup>-1</sup>) in Wu et al. (2012), C<sub>2</sub>H  $N=1-0$  (1.0 km s<sup>-1</sup>) reported in Liu et al. (2019), and HCN  $J=1-0$  (1.06 km s<sup>-1</sup>) in Yuan et al. (2016). The differences in line widths among different molecular tracers may result from turbulence at different scales. Fig. 6 (c, d) show the distributions of the differences in line widths between <sup>13</sup>CO and C<sup>18</sup>O with NH<sub>3</sub>. The mean widths of NH<sub>3</sub> and <sup>13</sup>CO are nearly identical, with an average difference of  $\sim 0.14$  km s<sup>-1</sup>. In contrast to high-mass star-forming clumps, where the average difference between NH<sub>3</sub> and <sup>13</sup>CO is 4.3 km s<sup>-1</sup> (Wienen et al. 2012), the intrinsic line widths of NH<sub>3</sub>, <sup>13</sup>CO and C<sup>18</sup>O are approximately equal in our sample. This finding is consistent with the notion that these PGCCs are quiescent, as the majority of them appear to be transitioning from clouds to dense cores (Wu et al. 2012).

#### 5.4. A comparison with different star formation samples

To investigate the physical conditions and assess the potential for star formation within the cold clumps, we conducted a comparative analysis of various NH<sub>3</sub> molecular line surveys targeting different types of celestial objects. This analysis involved a comprehensive examination of line widths, kinetic temperatures, NH<sub>3</sub> column densities, as well as column densities of H<sub>2</sub>, and fractional abundances. In this particular study, to conduct a more comprehensive comparative analysis, we have incorporated not only the samples mentioned in Sec. 4.3, but also included additional statistical samples, ultra-compact HII (UC HII) regions or

UC H<sub>II</sub> region candidates (Molinari et al. 1996), High Infrared (IR) extinction clouds (Rygl et al. 2010) and Extended Green Objects (EGOs) (Cyganowski et al. 2013). The fundamental information regarding these sources has been presented in Table 4. It is crucial to emphasize that not all papers provide data for every parameter. In certain studies, some parameters were not reported. Therefore, in the comparison involving these parameters, we opted to consider only those papers that presented available data.

The kinetic temperatures of the cores range from 8.9 to 20.7 K, with an average of  $12.3 \pm 2.9$  K and a median value of 11.4 K (as mentioned in Sect. 4.2), and after cross-matching our NH<sub>3</sub> detected 249 sources with PGCCs from Planck Collaboration et al. (2016), we have observed that the dust temperature ( $T_{\text{dust}}$ ) of these 249 sources falls within the range of 8.6 to 13.9 K, with an average value of 11.5 K. The similarity in temperature ranges between  $T_{\text{kin}}$  and  $T_{\text{dust}}$  indicates an efficient coupling of gas and dust. The cumulative distribution of the kinetic temperature of NH<sub>3</sub> for different samples is presented in Fig. 7 (a). The results indicate that the UC H<sub>II</sub> candidates exhibit the highest kinetic temperatures (Molinari et al. 1996), while the Planck cold cores show lower temperatures compared to other classes of sources. The temperature distribution of the samples is distinct and follows the expected evolutionary sequence. Hence, the kinetic temperature can serve as a reliable indicator for distinguishing between different evolutionary stages.

Fig. 7 (b) depicts the cumulative distribution of NH<sub>3</sub>(1,1) line widths. Our analysis indicates that the line widths of ATLASGAL sources are the largest. The changes in the ATLASGAL and UC H<sub>II</sub> regions flatten off when the line width exceeds  $\sim 2.5 \text{ km s}^{-1}$ , and their slopes are nearly identical when the line width is smaller than  $2.5 \text{ km s}^{-1}$ . The variation of the cumulative fraction function of line width for the Planck cold cores is narrower when compared to other star-forming samples (Dunham et al. 2011; Wienen et al. 2012; Chira et al. 2013), and exhibits a similar cumulative distribution figure to those found in the dense cores of regions like Cepheus, and Orion L1630 and L1641, and Ophiuchus, as reported in Harju et al. (1991, 1993) and Friesen et al. (2009). However, the average linewidth in the Planck cold cores is slightly larger than that observed in Ophiuchus ( $0.62 \text{ km s}^{-1}$ ). Notably, the higher line width values observed in the Planck cold cores, in comparison to the dense cores in Ophiuchus, may imply that they are in more advanced and warmer stages of evolution. However, it is worth highlighting that the line width remains relatively small across the various samples under examination. Fig. 7 (c), (d), and (e) presents the cumulative distribution of column densities for NH<sub>3</sub>, H<sub>2</sub>, and fractional ammonia abundances for various samples. The ammonia column densities of cold cores are generally higher than those of other samples and are even comparable to those of ATLASGAL and EGO sources. Conversely, the cumulative distribution for Planck cold clumps exhibits the smallest H<sub>2</sub> column density range, resulting in high ammonia abundances. Despite the relatively high NH<sub>3</sub> column density observed in Planck cold cores, comprehensive consideration of its lower temperature, linewidth, and other parameters still leads to the conclusion that Planck sources are in an early stage of evolution.

To quantitatively compare the distributions, we conducted two-sample Kolmogorov-Smirnov (K-S) tests using the `scipy.stats.ks_2samp` procedure in the `scipy` package. This statistical test assesses the dissimilarity between two samples, with the K-S statistic serving as a measure of this dissimilarity, ranging from 0 to 1. A K-S statistic of 0 implies that there is no

significant difference, suggesting the two samples may be from the same distribution. Conversely, a higher K-S statistic suggests a lower likelihood of the samples originating from the same distribution. Additionally, we computed P-values for each pair of samples, representing the probability that the samples share the same distribution. The outcomes of these tests are summarized in Table A.4 of Appendix A. In summary, the K-S test results for all examined parameters, including kinetic temperature, line width, ammonia column density, hydrogen molecule column density, and ammonia abundance, consistently yielded P-values below 0.05. These findings strongly imply substantial disparities between the Planck cold cores and the comparison samples in the examined parameters, which may reflect variations in their physical properties or the influence of distinct environmental conditions. Nevertheless, it is noteworthy that, in the distributions of kinetic temperature and linewidth, the Perseus, Cepheus, and Orion L1630/L1641 samples exhibit smaller KS statistic values. Moreover, their P-values are comparatively larger than those of other samples. In contrast, there is no pronounced similarity in the distributions of ammonia column density and hydrogen molecule column density among these samples. Additionally, in the abundance distribution, Planck displays relatively smaller KS values and larger P-values when compared to BGPS and ATLASGAL samples.

## 6. Summary

We used the Nanshan 26-m radio telescope to perform single-pointing observations of NH<sub>3</sub>(1,1) and (2,2) inversion transitions towards 672 Planck sources. The main results of this study are as follows:

1. Among the observed 672 Planck sources, 249 (37%) were detected. Among these detections, 187 cores exhibit NH<sub>3</sub>(1,1) hyperfine structure while 76 (11%) cores also show corresponding NH<sub>3</sub>(2,2) emission lines. The observed sources are mainly located in local star-forming regions. The detection rate of NH<sub>3</sub> is positively correlated with the continuum emission fluxes of Planck sources at a frequency of 857 GHz, increasing as the 857 GHz flux density increases.
2. Among the observed 672 sources,  $\sim 22\%$  have associated stellar and IR objects within the beam size ( $\sim 2'$ ). This may indicate low star formation activity of the cores in our sample and the ammonia detection rate is higher in sources with matching stellar objects.
3. The correlation between thermal and non-thermal velocity dispersion in NH<sub>3</sub>(1,1) indicates the dominance of non-thermal pressure and supersonic non-thermal motions in the dense gas traced by NH<sub>3</sub>. In contrast to high-mass star-forming clumps and dense cores in star-forming regions, the relationship between non-thermal velocity dispersion and kinetic temperatures in PGCCs is notably weaker, with lower values observed for both parameters relative to other samples under our examination.
4. The comparison of the line-center velocities of NH<sub>3</sub> with those from <sup>13</sup>CO and C<sup>18</sup>O reveals small discrepancies ( $0.17 \pm 0.33 \text{ km s}^{-1}$ ,  $0.12 \pm 0.18 \text{ km s}^{-1}$ ). The widths of NH<sub>3</sub>, <sup>13</sup>CO, and C<sup>18</sup>O in our sample were almost undistinguishable. These are consistent with the idea that these PGCCs are quiescent, as the majority of them appear to be transitioning from clouds to dense clumps.
5. The ammonia column densities range between  $0.36$  to  $6.07 \times 10^{15} \text{ cm}^{-2}$ . The mean value is approximately  $2.04 \times 10^{15} \text{ cm}^{-2}$ , and the fractional abundances of ammonia range from

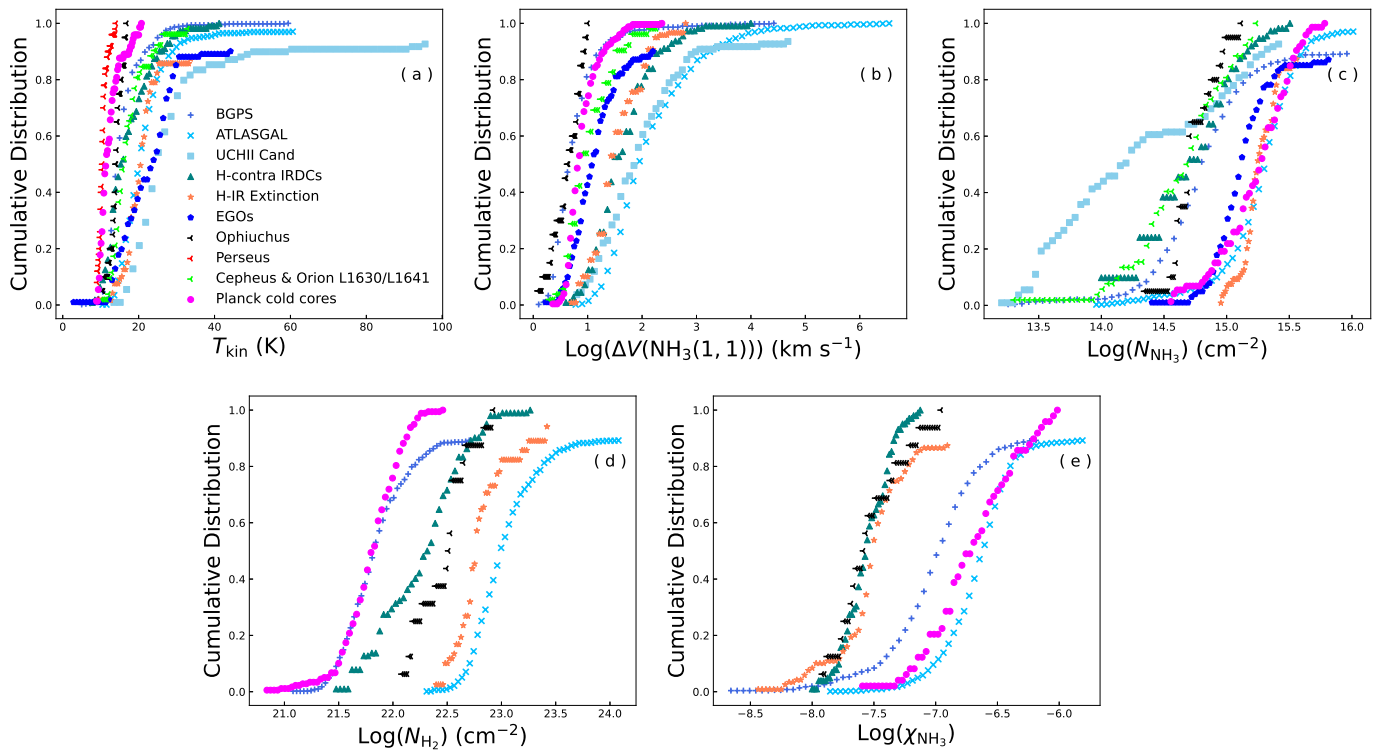


**Fig. 7.** Comparisons for the cumulative distribution of the line widths of  $\text{NH}_3(1,1)$ , kinetic temperatures, column densities, and abundances of different star formation samples.

0.3 to  $9.7 \times 10^{-7}$ , with an average of  $2.7 \times 10^{-7}$ . Our observed fractional abundances of  $\text{NH}_3$  are consistently one order of magnitude larger in PGCCs than in Massive Star-forming (MSF) regions and Infrared Dark Clouds (IRDCs). This significant difference in  $\text{NH}_3$  fractional abundance suggests that PGCCs are in an earlier phase of cloud evolution compared to MSF regions and IRDCs. The elevated  $\text{NH}_3$  fractional abundance in PGCCs relative to other star-forming regions is likely attributable to the earlier phase of cloud evolution of PGCCs compared to Massive Star-forming (MSF) regions or even IRDCs.

6. The kinetic temperatures of the cores range from 8.9 to 20.7 K, with an average of  $12.3 \pm 2.9$  K. Similar temperature ranges between  $T_{\text{kin}}$  and  $T_{\text{dust}}$  indicate that the gas and dust are well coupled.
7. The cumulative distribution shapes of line widths in the Planck cold cores closely resemble those of the dense cores found in regions Cepheus, and Orion L1630 and L1641, but with slightly higher values compared to Ophiuchus. However, the higher line width values in the Planck cold cores, when compared to these dense cores in Ophiuchus, suggest that they might be in more advanced and warmer stages of evolution. Nevertheless, it is worth noting that line width values remain small across the various samples under examination. This observation highlights the unique characteristics of the Planck cold cores in the context of their evolutionary stages.

**Acknowledgements.** This work was mainly funded by the National Key R&D Program of China under grant No. 2022YFA1603103. It was also partially funded by the Regional Collaborative Innovation Project of Xinjiang Uyghur Autonomous Region grant 2022E01050, the Tianshan Talent Program of Xinjiang Uyghur Autonomous Region under grant No. 2022TSYCLJ0005, the Natural Science Foundation of Xinjiang Uyghur Autonomous Region under grant No. 2022D01E06, the Chinese Academy of Sciences (CAS) “Light of West China” Program under grant Nos. xbzg-zdsys-202212, 2020-XBQNXZ-017,

and 2021-XBQNXZ-028, the National Key R&D Program of China with grant 2023YFA1608002, the National Natural Science Foundation of China (NSFC) under grants Nos. 12173075, 12373029, and 12103082, the Xinjiang Key Laboratory of Radio Astrophysics under grant No. 2023D04033, the Youth Innovation Promotion Association CAS. C.H. has been funded by the Chinese Academy of Sciences President’s International Fellowship Initiative by grant No. 2023VMA0031. Moreover, this work is sponsored (in part) by the Science Committee of the Ministry of Science and Higher Education of the Republic of Kazakhstan grant No. AP13067768. This work is based on observations made with the Nanshan 26-m radio telescope, the Nanshan 26-m Radio Telescope is partly supported by the Operation, Maintenance and Upgrading Fund for Astronomical Telescopes and Facility Instruments, budgeted from the Ministry of Finance of China (MOF) and administrated by the Chinese Academy of Sciences (CAS), and the Urumqi Nanshan Astronomy and Deep Space Exploration Observation and Research Station of Xinjiang.

## References

- Allen, L. E., Calvet, N., D'Alessio, P., et al. 2004, *ApJS*, 154, 363.
- André, P., Men'shchikov, A., Bontemps, S., et al. 2010, *A&A*, 518, L102.
- Ao, Y., Henkel, C., Menten, K. M., et al. 2013, *A&A*, 550, A135.
- Aguirre, J. E., Ginsburg, A. G., Dunham, M. K., et al. 2011, *ApJS*, 192, 4.
- Barranco, J. A., & Goodman, A. A. 1998, *ApJ*, 504, 207.
- Bergin, E. A. & Langer, W. D. 1997, *ApJ*, 486, 316.
- Bergin, E. A. & Tafalla, M. 2007, *ARA&A*, 45, 339.
- Chira, R.-A., Beuther, H., Linz, H., et al. 2013, *A&A*, 552, A40.
- Cho, J., & Lazarian, A. 2003, Revista Mexicana de Astronomia y Astrofisica Conference Series, 15, 293.
- Cyganowski, C. J., Koda, J., Rosolowsky, E., et al. 2013, *ApJ*, 764, 61.
- Dame, T. M., Hartmann, D., & Thaddeus, P. 2001, *ApJ*, 547, 792.
- Danby, G., Flower, D. R., Valiron, P., et al. 1988, *MNRAS*, 235, 229.
- Dunham, M. K., Rosolowsky, E., Evans, N. J., II, et al. 2011, *ApJ*, 741, 110.
- Dewangan, L. K., Ojha, D. K., Luna, A., et al. 2016, *ApJ*, 819, 66.
- Eden, D. J., Liu, T., Kim, K.-T., et al. 2019, *MNRAS*, 485, 2895.
- Evans, N. J., II 1999, *ARA&A*, 37, 311.
- Fehér, O., Tóth, L. V., Kraus, A., et al. 2022, *ApJS*, 258, 17.
- Frerking, M. A., Langer, W. D., & Wilson, R. W. 1982, *ApJ*, 262, 590.
- Friesen, R. K., Di Francesco, J., Shirley, Y. L., et al. 2009, *ApJ*, 697, 1457.
- Ginsburg, A., Henkel, C., Ao, Y., et al. 2016, *A&A*, 586, A50.
- Guesten, R., Walmsley, C. M., Ungerechts, H., et al. 1985, *A&A*, 142, 381.
- Gutermuth, R. A., Megeath, S. T., Muzerolle, J., et al. 2004, *ApJS*, 154, 374.
- Goldreich, P. & Kwan, J. 1974, *ApJ*, 189, 441.
- Harju, J., Walmsley, C. M., & Wouterloot, J. G. A. 1991, *A&A*, 245, 643.
- Harju, J., Walmsley, C. M., & Wouterloot, J. G. A. 1993, *A&AS*, 98, 51.
- Ho, P. T. P., & Townes, C. H. 1983, *ARA&A*, 21, 239.
- Hunter, J. D. 2007, Computing in Science and Engineering, 9, 90.
- Immer, K., Kauffmann, J., Pillai, T., et al. 2016, *A&A*, 595, A94.
- Jijina, J., Myers, P. C., & Adams, F. C. 1999, *ApJS*, 125, 161.
- Juvela, M., Ristorcelli, I., Montier, L. A., et al. 2010, *A&A*, 518, L93.
- Juvela, M., Ristorcelli, I., Pagani, L., et al. 2012, *A&A*, 541, A12.
- Kawamura, A., Onishi, T., Yonekura, Y., et al. 1998, *ApJS*, 117, 387.
- Kim, G., Tatematsu, K., Liu, T., et al. 2020, *ApJS*, 249, 33.
- Kirk, H., Johnstone, D., & Tafalla, M. 2007, *ApJ*, 668, 1042.
- Kong, S., Lada, C. J., Lada, E. A., et al. 2015, *ApJ*, 805, 58.
- Kunth, D., Guideroni, B., Heydari-Malayeri, M., et al. 1996, The Interplay Between Massive Star Formation, the ISM and Galaxy Evolution, 11.
- Lada, C. J., Lada, E. A., Clemens, D. P., et al. 1994, *ApJ*, 429, 694.
- Lada, C. J., Bergin, E. A., Alves, J. F., & Huard, T. L. 2003, *ApJ*, 586, 286.
- Lada, C. J., Lombardi, M., & Alves, J. F. 2009, *ApJ*, 703, 52.
- Levshakov, S. A., Henkel, C., Reimers, D., & Wang, M. 2014, *A&A*, 567, A78.
- Lombardi, M., Lada, C. J., & Alves, J. 2010, *A&A*, 512, A67.
- Liu, T., Wu, Y., & Zhang, H. 2012, *ApJS*, 202, 4.
- Liu, T., Zhang, Q., Kim, K.-T., et al. 2016, *ApJS*, 222, 7.
- Liu, T., Kim, K.-T., Juvela, M., et al. 2018, *ApJS*, 234, 28.
- Liu, X.-C., Wu, Y., Zhang, C., et al. 2019, *A&A*, 622, A32.
- Lumsden, S. L., Hoare, M. G., Urquhart, J. S., et al. 2013, *ApJS*, 208, 11.
- McCutcheon, W. H., Shuter, W. L. H., Dickman, R. L., et al. 1980, *ApJ*, 237, f9.
- Melin, J.-B., Aghanim, N., Bartelmann, M., et al. 2012, *A&A*, 548, A51.
- Meng, F., Wu, Y., & Liu, T. 2013, *ApJS*, 209, 37.
- Merello, M., Molinari, S., Rygl, K. L. J., et al. 2019, *MNRAS*, 483, 5355.
- Molinari, S., Brand, J., Cesaroni, R., et al. 1996, *A&A*, 308, 573.
- Molinari, S., Swinyard, B., Bally, J., et al. 2010, *PASP*, 122, 314.
- Pineda, J. L., Goldsmith, P. F., Chapman, N., et al. 2010, *ApJ*, 721, 686.
- Pillai, T., Wyrowski, F., Carey, S. J., et al. 2006, *A&A*, 450, 569.
- Planck Collaboration, Ade, P. A. R., Aghanim, N., et al. 2011a, *A&A*, 536, A1.
- Planck Collaboration, Ade, P. A. R., Aghanim, N., et al. 2011b, *A&A*, 536, A7.
- Planck Collaboration, Ade, P. A. R., Aghanim, N., et al. 2011, *A&A*, 536, A23.
- Planck Collaboration, Ade, P. A. R., Aghanim, N., et al. 2016, *A&A*, 594, A28.
- Ragan, S. E., Bergin, E. A., & Wilner, D. 2011, *ApJ*, 736, 163.
- Reid, M. J., Dame, T. M., Menten, K. M., et al. 2016, *ApJ*, 823, 77.
- Rygl, K. L. J., Wyrowski, F., Schuller, F., et al. 2010, *A&A*, 515, A42.
- Rosolowsky, E. W., Pineda, J. E., Foster, J. B., et al. 2008, *ApJS*, 175, 509.
- Shan, W., Yang, J., Shi, S., et al. 2012, IEEE Transactions on Terahertz Science and Technology, 2, 593.
- Sharpless, S. 1959, *ApJS*, 4, 257.
- Schnee, S., Rosolowsky, E., Foster, J., et al. 2009, *ApJ*, 691, 1754.
- Schuller, F., Menten, K. M., Contreras, Y., et al. 2009, *A&A*, 504, 415.
- Shirley, Y. L. 2015, *PASP*, 127, 299.
- Sridharan, T. K., Beuther, H., Schilke, P., et al. 2002, *ApJ*, 566, 931.
- Svoboda, B. E., Shirley, Y. L., Battersby, C., et al. 2016, *ApJ*, 822, 59.
- Tafalla, M., Myers, P. C., Caselli, P., & Walmsley, C. M. 2004, *A&A*, 416, 191.
- Tang, X. D., Henkel, C., Menten, K. M., et al. 2017, *A&A*, 598, A30.
- Tang, X. D., Henkel, C., Menten, K. M., et al. 2018, *A&A*, 609, A16.
- Tang, X. D., Henkel, C., Wyrowski, F., et al. 2018, *A&A*, 611, A6.
- Tang, X. D., Henkel, C., Menten, K. M., et al. 2021, *A&A*, 655, A12.
- Tatematsu, K., Liu, T., Ohashi, S., et al. 2017, *ApJS*, 228, 12.
- Tatematsu, K., Liu, T., Kim, G., et al. 2020, *ApJ*, 895, 119.
- Urquhart, J. S., Figura, C. C., Moore, T. J. T., et al. 2015, *MNRAS*, 452, 4029.
- Ungerechts, H., Walmsley, C. M., & Winnewisser, G. 1986, *A&A*, 157, 207.
- Ungerechts, H., Bergin, E. A., Goldsmith, P. F., et al. 1997, *ApJ*, 482, 245.
- Walsh, A. J., Myers, P. C., & Burton, M. G. 2004, *ApJ*, 614, 194.
- Walmsley, C. M., & Ungerechts, H. 1983, *A&A*, 122, 164.
- Wienen, M., Wyrowski, F., Schuller, F., et al. 2012, *A&A*, 544, A146.
- Wood, D. O. S., & Churchwell, E. 1989, *ApJ*, 340, 265.
- Wu, Y., Zhang, Q., Yu, W., et al. 2006, *A&A*, 450, 607.
- Wu, Y., Liu, T., Meng, F., et al. 2012, *ApJ*, 756, 76.
- Wu, G., Qiu, K., Esimbek, J., et al. 2018, *A&A*, 616, A111.
- Wu, Y., & Evans, N. J. 1989, *ApJ*, 340, 307.
- Yuan, J., Wu, Y., Liu, T., et al. 2016, *ApJ*, 820, 37.
- Zhang, T., Wu, Y., Liu, T., et al. 2016, *ApJS*, 224, 43.
- Zhang, C.-P., Liu, T., Yuan, J., et al. 2018, *ApJS*, 236, 49.
- Zhang, C., Wu, Y., Liu, X., et al. 2020, *ApJS*, 247, 29.

- <sup>1</sup> Xinjiang Astronomical Observatory, Chinese Academy of Sciences, 830011 Urumqi, P. R. China  
e-mail: dilda@xao.ac.cn, jarken@xao.ac.cn, tangxindi@xao.ac.cn
- <sup>2</sup> University of Chinese Academy of Sciences, 100080 Beijing, P. R. China
- <sup>3</sup> Key Laboratory of Radio Astronomy, Chinese Academy of Sciences, Nanjing, JiangSu 210008, P. R. China
- <sup>4</sup> Xinjiang Key Laboratory of Radio Astrophysics, Urumqi 830011, PR China
- <sup>5</sup> Max-Planck-Institut für Radioastronomie, Auf dem Hügel 69, 53121 Bonn, Germany
- <sup>6</sup> Astronomy Department, King Abdulaziz University, PO Box 80203, 21589 Jeddah, Saudi Arabia
- <sup>7</sup> Shanghai Astronomical Observatory, Chinese Academy of Sciences, 80 Nandan Road, Shanghai 200030, People's Republic of China
- <sup>8</sup> Energetic Cosmos Laboratory, Nazarbayev University, Astana 010000, Kazakhstan
- <sup>9</sup> Institute of Experimental and Theoretical Physics, Al-Farabi Kazakh National University, Almaty 050040, Kazakhstan

## Appendix A: ECC Clump Catalogue

**Table A.1.** Basic information of the observed sources

Num	Name	Glon °	Glat °	Dist kpc	Num	Name	Glon °	Glat °	Dist kpc	Num	Name	Glon °	Glat °	Dist kpc
1	G005.03+19.07	5.03	19.08	1.50	71	G052.99+03.07	53.00	3.08		141	G098.50-03.24	98.50	-3.25	
2	G005.29+14.47	5.30	14.48		72	G054.03-02.38	54.03	-2.39		142	G098.52+13.88	98.53	13.88	1.22
3	G005.29+11.07	5.30	11.07	1.44	73	G056.84+04.81	56.84	4.82		143	G098.89+14.01	98.90	14.02	1.17
4	G005.31+10.78	5.32	10.79	0.12	74	G057.08+04.46	57.08	4.46		144	G098.96+13.68	98.96	13.69	1.17
5	G005.69+36.84	5.69	36.84	0.21	75	G057.10+03.65	57.11	3.66	0.77	145	G099.11+13.97	99.12	13.98	
6	G005.80+19.92	5.80	19.93	1.05	76	G057.17+03.41	57.17	3.42		146	G099.97+14.76	99.98	14.77	
7	G006.04+36.74	6.04	36.75	1.19	77	G057.26+04.01	57.26	4.01	-0.66	147	G100.32+14.84	100.33	14.84	
8	G006.08+20.26	6.09	20.26	1.33	78	G058.02+03.02	58.03	3.02		148	G100.45+14.95	100.46	14.96	
9	G006.32+20.44	6.33	20.44	1.38	79	G058.07+03.20	58.07	3.21		149	G101.14-15.28	101.14	-15.29	
10	G006.41+20.56	6.42	20.56	1.42	80	G058.16+03.50	58.16	3.51	0.67	150	G101.49+16.80	101.49	16.80	
11	G006.70+20.66	6.70	20.66	1.17	81	G058.97-01.66	58.97	-1.66		151	G101.62-28.84	101.62	-28.84	
12	G006.94+05.84	6.94	5.85	0.43	82	G060.75-01.23	60.75	-1.23	0.88	152	G101.88+15.17	101.89	15.17	
13	G006.96+00.89	6.97	0.90		83	G061.76-10.80	61.77	-10.81		153	G102.17+07.27	102.17	7.27	-0.77
14	G006.98+20.72	6.99	20.72	0.95	84	G065.30-08.44	65.30	-8.44		154	G102.19+15.24	102.19	15.25	
15	G007.14+05.94	7.14	5.94	1.36	85	G065.43-03.15	65.43	-3.15	0.35	155	G102.34+15.96	102.35	15.97	0.88
16	G007.53+21.10	7.54	21.10	0.88	86	G070.44-01.54	70.44	-1.55	1.25	156	G102.70+15.19	102.70	15.19	0.17
17	G007.80+21.10	7.80	21.10	0.82	87	G070.72-00.63	70.73	-0.63	1.23	157	G102.72-25.98	102.72	-25.99	
18	G008.43+36.35	8.44	36.35		88	G074.11+00.11	74.11	0.11	2.22	158	G102.72+15.36	102.72	15.37	0.32
19	G008.52+21.84	8.53	21.84	0.94	89	G084.11+15.50	84.11	15.50		159	G103.18-17.09	103.18	-17.09	14.52
20	G008.67+22.14	8.68	22.15	0.84	90	G084.79-01.11	84.79	-1.12	2.22	160	G103.22-15.23	103.23	-15.23	
21	G009.62+21.28	9.62	21.28	0.12	91	G089.03-41.28	89.03	-41.29	0.21	161	G103.49+13.07	103.49	13.08	
22	G009.79+00.87	9.80	0.88	2.91	92	G089.29+04.01	89.30	4.01		162	G103.71+14.88	103.71	14.88	
23	G011.09+03.43	11.10	3.43	1.12	93	G089.36-00.67	89.36	-0.67	0.73	163	G103.77+13.90	103.78	13.90	
24	G011.40+36.19	11.40	36.19	0.20	94	G089.62+02.16	89.63	2.16	1.62	164	G103.90+13.97	103.91	13.98	0.89
25	G013.86+04.55	13.86	4.56		95	G089.64-06.86	89.65	-6.86	0.54	165	G104.06+12.19	104.06	12.20	
26	G014.74+04.06	14.74	4.07		96	G089.75-02.16	89.76	-2.16	0.62	166	G104.78+11.49	104.79	11.49	
27	G014.87+19.62	14.88	19.63		97	G089.64-06.59	89.65	-6.60	0.67	167	G105.55+10.40	105.56	10.41	0.90
28	G015.16+07.23	15.16	7.24	0.29	98	G089.93-07.03	89.93	-7.03		168	G106.30+13.57	106.30	13.57	
29	G016.67-02.76	16.68	-2.76		99	G089.93-01.94	89.93	-1.94	1.18	169	G106.89+16.72	106.90	16.72	
30	G017.22-01.47	17.23	-1.47	3.02	100	G090.76-04.55	90.77	-4.56	0.48	170	G107.51-09.36	107.51	-9.37	
31	G018.39+19.39	18.39	19.39		101	G091.29-38.15	91.30	-38.16		171	G107.64-09.29	107.64	-9.29	
32	G018.61+08.87	18.61	8.88	0.74	102	G091.73+04.36	91.74	4.37	2.07	172	G108.10+13.19	108.11	13.19	1.06
33	G019.86+20.40	19.86	20.40		103	G092.02+03.93	92.02	3.94	0.80	173	G108.23+15.61	108.24	15.62	
34	G020.52+01.69	20.52	1.70	1.78	104	G092.26-03.80	92.26	3.81	1.63	174	G108.85-00.80	108.85	-0.80	0.18
35	G021.20+04.96	21.20	4.97	0.28	105	G092.48-02.64	92.48	-2.65		175	G110.41+11.52	110.41	11.53	0.90
36	G021.26+12.12	21.27	12.12		106	G092.79+09.14	92.79	9.14	0.31	176	G110.52+19.17	110.52	19.17	1.47
37	G021.66+03.78	21.67	3.79	0.63	107	G092.83-11.03	92.83	-11.03	0.41	177	G110.54+11.91	110.54	11.91	0.30
38	G023.33+11.81	23.33	11.82		108	G093.12-10.40	93.12	-10.41	0.24	178	G110.65+09.65	110.65	9.65	0.30
39	G023.37+08.21	23.38	8.22	0.54	109	G093.16+09.61	93.16	9.61	0.44	179	G110.76+19.43	110.76	19.43	0.24
40	G023.68+07.53	23.69	7.54	0.67	110	G093.20+09.53	93.21	9.54	1.46	180	G110.76+20.18	110.76	20.18	0.22
41	G025.48+06.18	25.49	6.19	0.23	111	G093.22-04.59	93.23	-4.59	0.69	181	G110.96+19.49	110.96	19.49	0.36
42	G026.45+08.02	26.46	8.03	-0.82	112	G093.31-11.68	93.32	-11.68	0.40	182	G111.04+14.03	111.05	14.03	
43	G026.85+06.78	26.85	6.79	0.55	113	G093.36-12.06	93.36	-12.06	0.14	183	G111.33+19.94	111.34	19.95	
44	G026.93-20.68	26.94	-20.68		114	G093.44-04.66	93.45	-4.67	0.12	184	G111.42+19.82	111.42	19.83	0.40
45	G027.09-20.70	27.09	-20.70		115	G093.51-04.31	93.52	-4.31	0.12	185	G111.46+20.18	111.47	20.18	0.63
46	G027.66+05.71	27.66	5.72	0.59	116	G093.62-04.44	93.63	-4.44	0.14	186	G111.66+20.20	111.67	20.20	1.30
47	G027.70-21.02	27.71	-21.02	0.41	117	G093.66+04.66	93.67	4.67		187	G111.68+19.74	111.69	19.75	1.40
48	G028.45-06.39	28.45	-6.39	0.93	118	G093.69+09.99	93.69	9.99	0.21	188	G111.77+13.78	111.77	13.79	0.30
49	G028.56-00.24	28.56	-0.24	4.09	119	G093.75-04.59	93.76	-4.59	0.63	189	G111.77+20.26	111.77	20.26	1.31
50	G028.71+03.88	28.72	3.88	0.55	120	G093.91+10.02	93.91	10.03	1.40	190	G111.97+20.52	111.97	20.52	
51	G028.87+04.23	28.87	4.24	0.52	121	G093.99-04.91	94.00	-4.91	0.67	191	G112.03+17.89	112.04	17.90	
52	G030.43+02.35	30.43	2.35	0.44	122	G094.08+09.46	94.09	9.46	0.98	192	G112.25+13.82	112.26	13.82	0.78
53	G030.78+05.22	30.78	5.23	0.57	123	G095.11+06.50	95.12	6.50	1.37	193	G112.52+08.38	112.52	8.39	
54	G031.26-05.37	31.27	-5.38		124	G095.29-09.66	95.30	-9.67	0.39	194	G112.60+08.53	112.61	8.54	0.27
55	G031.44+04.18	31.44	4.18	0.78	125	G095.51+09.97	95.52	9.97	1.37	195	G112.63+20.80	112.63	20.80	
56	G032.38-15.26	32.39	-15.27		126	G095.75+08.17	95.76	8.18	0.80	196	G113.42+16.97	113.42	16.98	
57	G032.93+02.68	32.94	2.69	0.84	127	G095.97+08.17	95.98	8.18	-0.73	197	G113.62+15.01	113.62	15.02	
58	G033.70-00.01	33.71	-0.02	0.70	128	G096.30+10.01	96.31	10.01		198	G113.75+14.90	113.75	14.90	
59	G034.69-06.57	34.69	-6.58	0.67	129	G096.37+10.29	96.37	10.29		199	G114.16+14.80	114.17	14.81	0.77
60	G035.13+11.37	35.13	11.38		130	G096.59+10.29	96.59	10.29	1.29	200	G114.41-13.93	114.41	-13.94	
61	G037.51+44.57	37.52	44.57	0.20	131	G096.94+10.25	96.94	10.26	1.26	201	G114.56+14.72	114.57	14.73	0.79
62	G038.36-00.95	38.36	-0.95	1.11	132	G097.09+10.12	97.10	10.12	1.27	202	G114.67+14.47	114.68	14.48	0.77
63	G043.02+08.36	43.02	8.37	0.30	133	G097.20+09.87	97.21	9.88	1.22	203	G115.81-03.54	115.82	-3.55	0.37
64	G046.75-07.68	46.76	-7.69		134	G097.38+09.95	97.38	9.95	1.17	204	G115.92+09.46	115.93	9.46	1.00
65	G047.74-05.56	47.75	-5.57		135	G097.71+15.32	97.71	15.33		205	G116.01+09.12	116.02	9.12	
66	G048.25-05.73	48.25	-5.74		136	G097.77+08.59	97.78	8.59	1.10	206	G116.08-02.38	116.08	-2.39	0.39
67	G048.40-05.82	48.41	-5.83		137	G097.80+15.21	97.80	15.21		207	G116.12+08.98	116.13	8.99</td	

**Table A.2.** Continued

Num	Name	Glon	Glat	Dist	Num	Name	Glon	Glat	Dist	Num	Name	Glon	Glat	Dist
		°	°	kpc			°	°	kpc			°	°	kpc
211	G117.11+12.42	117.11	12.43	0.11	286	G144.44+08.55	144.45	8.56	-0.66	361	G159.41-34.36	159.41	-34.36	1.20
212	G118.08-09.68	118.08	-9.69		287	G144.49+08.70	144.49	8.71		362	G159.52+03.26	159.52	3.27	3.50
213	G118.14+08.83	118.15	8.84		288	G144.66+00.16	144.67	0.17	0.85	363	G159.58-32.84	159.59	-32.84	0.25
214	G118.25-52.70	118.25	-52.71	0.26	289	G144.66+06.11	144.67	6.11	0.53	364	G159.65-19.68	159.65	-19.69	0.29
215	G118.34+08.66	118.34	8.67		290	G144.84+00.76	144.84	0.76		365	G159.65+11.39	159.65	11.40	0.17
216	G118.36+21.74	118.37	21.74	0.38	291	G145.08-39.30	145.09	-39.31	0.28	366	G159.67-05.71	159.68	-5.72	0.14
217	G120.16+03.09	120.17	3.10	1.36	292	G145.48+09.51	145.48	9.52	-0.66	367	G159.67-34.31	159.68	-34.32	0.43
218	G120.67+02.66	120.67	2.67	1.82	293	G145.81+10.97	145.81	10.98		368	G159.76-19.62	159.76	-19.63	0.31
219	G120.98+02.66	120.98	2.67	0.87	294	G145.87+17.77	145.88	17.78	0.20	369	G159.78-24.80	159.79	-24.81	
220	G121.35+03.39	121.35	3.40	0.72	295	G146.05+17.81	146.05	17.82	0.20	370	G159.82-10.48	159.83	-10.48	
221	G121.50-20.92	121.51	-20.92		296	G146.11+07.80	146.12	7.80		371	G160.33+03.24	160.33	3.25	
222	G121.57+23.39	121.57	23.40	0.38	297	G146.18+08.80	146.18	8.80		372	G160.35-06.37	160.36	-6.37	
223	G121.88-08.76	121.88	-8.76		298	G146.71+02.05	146.71	2.05	-1.03	373	G160.51-17.07	160.51	-17.07	0.14
224	G121.90-01.54	121.90	-1.55	-1.23	299	G147.01+03.39	147.02	3.40	0.59	374	G160.51-16.84	160.51	-16.84	1.12
225	G121.92-07.66	121.93	-7.67		300	G147.76+09.17	147.77	9.18		375	G160.53-19.72	160.53	-19.73	0.37
226	G121.92-01.71	121.93	-1.72		301	G147.96-08.02	147.96	-8.03	-0.82	376	G160.53-09.84	160.53	-9.84	0.65
227	G121.99+24.23	121.99	24.24	0.38	302	G148.00+00.09	148.01	0.09	0.77	377	G160.62-16.70	160.62	-16.70	0.14
228	G122.01-07.48	122.01	-7.48		303	G148.24+00.41	148.25	0.41		378	G160.64-35.04	160.64	-35.04	
229	G122.18-10.27	122.19	-10.28		304	G149.23+03.07	149.24	3.08	0.86	379	G160.83-09.46	160.84	-9.46	0.14
230	G122.62-12.13	122.63	-12.14		305	G149.41+03.37	149.41	3.38	0.50	380	G161.08-21.78	161.08	-21.78	
231	G122.73+09.61	122.74	9.61	0.32	306	G149.52-01.23	149.52	-1.23	0.89	381	G161.21-08.72	161.21	-8.73	0.71
232	G123.66+24.89	123.66	24.89	0.69	307	G149.58+03.45	149.59	3.45	0.17	382	G161.34-09.32	161.35	-9.33	0.25
233	G123.74+24.76	123.75	24.77	0.38	308	G149.65+03.54	149.66	3.55	0.17	383	G161.43-35.59	161.43	-35.59	1.49
234	G125.17+11.64	125.18	11.64		309	G150.22+03.91	150.23	3.92	0.18	384	G161.60-08.34	161.61	-8.35	0.59
235	G125.66-00.55	125.66	-0.56		310	G150.35-38.06	150.36	-38.06	0.55	385	G161.85-08.66	161.85	-8.67	0.47
236	G125.70+12.52	125.71	12.52	0.37	311	G150.44+03.95	150.45	3.96	0.87	386	G161.85-35.75	161.85	-35.75	1.74
237	G125.77+04.12	125.77	4.13	-1.01	312	G151.08+04.46	151.08	4.46	0.83	387	G162.24-09.04	162.25	-9.05	0.14
238	G126.27+05.11	126.28	5.12	0.48	313	G151.45+03.95	151.46	3.96	0.80	388	G162.46-08.70	162.47	-8.71	0.30
239	G126.49-01.30	126.50	-1.31		314	G151.58-38.58	151.59	-38.59		389	G162.64-31.67	162.64	-31.67	
240	G126.62+24.54	126.63	24.54	0.13	315	G153.34-08.00	153.35	-8.01		390	G162.79+01.34	162.80	1.34	-1.26
241	G126.65-71.43	126.66	-71.44		316	G153.34+11.26	153.35	11.26	0.30	391	G162.83-18.44	162.84	-18.45	0.14
242	G126.73+06.18	126.74	6.19		317	G153.74+35.91	153.74	35.92	0.35	392	G162.86-05.24	162.86	-5.25	0.14
243	G126.95-01.06	126.96	-1.06	-1.17	318	G154.07+05.09	154.07	5.10	0.24	393	G162.90-08.63	162.91	-8.63	0.14
244	G127.22-02.25	127.22	-2.26	0.57	319	G154.07+05.21	154.07	5.21	0.23	394	G163.21-08.40	163.21	-8.40	0.76
245	G127.31-70.09	127.32	-70.10		320	G154.48-15.17	154.49	-15.17		395	G163.32-08.42	163.32	-8.42	0.41
246	G127.66+13.95	127.66	13.96		321	G154.55-01.24	154.56	-1.25		396	G163.67-08.34	163.67	-8.35	0.44
247	G127.79+13.68	127.79	13.69		322	G154.68-15.34	154.69	-15.35	0.39	397	G163.82-08.32	163.83	-8.33	0.42
248	G127.85+14.16	127.86	14.17	0.49	323	G154.90+04.61	154.91	4.61	0.26	398	G164.13-08.85	164.14	-8.86	0.42
249	G127.88+02.66	127.88	2.67	1.16	324	G154.95-15.19	154.95	-15.19	0.14	399	G164.57-24.48	164.58	-24.48	0.14
250	G128.21+13.70	128.21	13.71		325	G155.45-14.59	155.46	-14.59	0.35	400	G164.75-24.19	164.75	-24.19	
251	G128.25+20.78	128.25	20.78	0.38	326	G155.52-08.93	155.52	-8.93		401	G164.81-05.67	164.82	-5.68	0.14
252	G128.89+13.68	128.89	13.69	0.13	327	G155.67+05.11	155.68	5.12	0.16	402	G164.92-12.65	164.93	-12.65	
253	G128.95-00.18	128.96	-0.19	1.43	328	G156.04+06.03	156.05	6.04		403	G164.94-08.57	164.95	-8.57	0.42
254	G128.95+04.44	128.96	4.44	0.21	329	G156.20+05.26	156.20	5.27	0.23	404	G164.94-05.71	164.95	-5.72	0.33
255	G129.22+15.17	129.22	15.17	0.21	330	G156.42+32.53	156.42	32.53		405	G165.16-07.55	165.17	-7.56	0.26
256	G129.90+11.62	129.90	11.62	0.78	331	G156.53-08.63	156.53	-8.63	0.14	406	G165.34-07.51	165.34	-7.52	0.38
257	G129.94+11.73	129.95	11.74		332	G156.90-08.49	156.91	-8.50	1.12	407	G165.69-09.14	165.70	-9.14	0.83
258	G129.96+13.78	129.97	13.79	0.31	333	G156.92-09.72	156.93	-9.73	0.14	408	G165.91-44.02	165.92	-44.03	
259	G130.14+11.07	130.14	11.07		334	G157.10-08.70	157.10	-8.71	1.09	409	G166.70-15.05	166.71	-15.06	0.14
260	G130.14+11.68	130.14	11.68		335	G157.12-11.56	157.13	-11.57	0.89	410	G166.99-15.34	166.99	-15.35	0.14
261	G130.14+13.78	130.14	13.79	0.45	336	G157.19-08.81	157.19	-8.82	0.14	411	G167.23-15.32	167.23	-15.33	0.14
262	G130.36+11.26	130.36	11.26	0.60	337	G157.25-01.00	157.26	-1.01	0.43	412	G168.00-15.69	168.00	-15.69	1.29
263	G130.56+11.51	130.56	11.51		338	G157.54-04.05	157.54	-4.05		413	G168.13-16.39	168.13	-16.39	1.10
264	G131.35-45.73	131.36	-45.73	0.24	339	G157.58-08.89	157.59	-8.89	0.14	414	G168.46-17.93	168.46	-17.94	
265	G131.72+09.70	131.73	9.71	1.07	340	G157.60-12.17	157.61	-12.18	1.17	415	G168.72-15.48	168.73	-15.48	0.99
266	G132.03+08.95	132.03	8.95	0.85	341	G157.91-08.23	157.92	-8.23	0.14	416	G168.85-15.83	168.86	-15.83	1.18
267	G132.07+08.80	132.08	8.80	0.85	342	G158.20-20.28	158.20	-20.28	0.14	417	G168.85-14.70	168.86	-14.71	0.14
268	G132.07+13.63	132.08	13.63		343	G158.22-20.14	158.23	-20.15	0.14	418	G169.14-01.13	169.15	-1.14	
269	G132.27+13.26	132.28	13.27		344	G158.24-21.80	158.25	-21.80	0.37	419	G169.32-16.15	169.32	-16.16	1.03
270	G132.29+09.36	132.30	9.37	1.25	345	G158.37-20.72	158.38	-20.72	0.73	420	G169.43-16.17	169.43	-16.18	1.08
271	G133.28+08.81	133.29	8.82	1.56	346	G158.40-21.86	158.40	-21.86	0.14	421	G169.76-16.15	169.76	-16.16	1.07
272	G133.48+09.02	133.48	9.03	1.68	347	G158.77-33.30	158.77	-33.31	0.60	422	G169.82-19.39	169.83	-19.39	0.14
273	G133.72-45.31	133.73	-45.32		348	G158.86-21.60	158.86	-21.60	0.52	423	G169.84-07.61	169.85	-7.61	1.18
274	G135.08+12.92	135.09	12.92		349	G158.88-34.18	158.88	-34.18	0.33	424	G169.98-18.97	169.98	-18.98	1.58
275	G135.28+12.90	135.29	12.90		350	G158.97-33.0								

**Table A.3.** Continued

Num	Name	Glon	Glat	Dist	Num	Name	Glon	Glat	Dist	Num	Name	Glon	Glat	Dist
		°	°	kpc			°	°	kpc			°	°	kpc
436	G171.14-17.58	171.15	-17.58	0.79	511	G177.86+01.04	177.87	1.04	1.71	586	G206.54-14.45	206.54	-14.46	0.42
437	G171.32+04.40	171.32	4.41		512	G177.89-20.16	177.89	-20.17	0.36	587	G206.60-14.40	206.61	-14.40	0.62
438	G171.34-10.67	171.34	-10.67	0.23	513	G177.97-09.72	177.98	-9.73	0.60	588	G206.87-04.36	206.87	-4.37	0.42
439	G171.34+02.59	171.34	2.59	1.78	514	G178.28-00.61	178.29	-0.62	0.94	589	G207.35-19.82	207.36	-19.83	0.42
440	G171.43-17.36	171.43	-17.37	0.23	515	G178.48-06.76	178.48	-6.77	0.23	590	G208.56+02.36	208.56	2.37	1.14
441	G171.49-14.90	171.50	-14.90	1.47	516	G178.72-07.01	178.73	-7.01	0.23	591	G209.20+02.12	209.20	2.13	1.13
442	G171.51-10.59	171.52	-10.60	1.35	517	G178.98-06.74	178.99	-6.75	0.59	592	G209.28-19.62	209.29	-19.63	1.08
443	G171.67-18.05	171.67	-18.05	0.23	518	G179.14-06.27	179.14	-6.28	0.23	593	G210.01-20.16	210.01	-20.17	0.42
444	G171.73-17.13	171.74	-17.13	0.23	519	G179.18-19.62	179.19	-19.63	0.31	594	G210.30-00.03	210.30	-0.03	5.44
445	G171.78-15.65	171.78	-15.66	0.23	520	G179.29+04.20	179.30	4.20		595	G210.67-36.77	210.67	-36.77	0.14
446	G171.78-08.44	171.78	-8.44	0.23	521	G179.40+04.06	179.41	4.07	0.70	596	G210.89-36.53	210.89	-36.54	0.14
447	G171.80-15.32	171.80	-15.33	1.64	522	G180.81-19.66	180.81	-19.67	0.35	597	G211.48-19.27	211.49	-19.27	0.61
448	G171.80-09.78	171.80	-9.78	0.23	523	G180.92+04.53	180.92	4.54	0.96	598	G211.70-12.17	211.71	-12.18	0.42
449	G171.84-05.22	171.85	-5.23	1.55	524	G181.16+04.33	181.16	4.33		599	G212.10-19.15	212.10	-19.16	0.65
450	G171.91-15.65	171.91	-15.66	0.23	525	G181.42-03.73	181.43	-3.73		600	G212.18+05.11	212.19	5.12	
451	G172.06-15.21	172.07	-15.21	1.65	526	G181.71+04.16	181.71	4.16		601	G213.92-13.61	213.93	-13.61	0.42
452	G172.13-16.93	172.13	-16.94	1.98	527	G181.73-19.35	181.74	-19.35	0.25	602	G213.96-19.64	213.97	-19.65	0.42
453	G172.15-16.02	172.16	-16.02	0.23	528	G181.84+00.31	181.85	0.32	1.76	603	G214.21-13.40	214.21	-13.40	1.39
454	G172.15-09.93	172.16	-9.93	0.23	529	G181.88+04.49	181.89	4.50		604	G214.43-19.90	214.43	-19.91	0.46
455	G172.30-09.91	172.31	-9.92	0.23	530	G182.02-00.16	182.02	-0.17		605	G214.54+00.98	214.54	0.99	
456	G172.33-18.24	172.33	-18.25	0.23	531	G182.04+00.41	182.04	0.41	1.76	606	G214.69-19.94	214.69	-19.95	0.42
457	G172.57-18.11	172.57	-18.11		532	G182.15-17.95	182.15	-17.95	0.23	607	G215.00-15.13	215.00	-15.13	
458	G172.83-05.17	172.84	-5.17	0.23	533	G182.19-17.71	182.20	-17.72	0.23	608	G215.41-16.39	215.42	-16.39	0.42
459	G172.85-14.74	172.86	-14.75	0.23	534	G182.30-19.19	182.31	-19.19	0.23	609	G215.70-15.05	215.71	-15.06	0.42
460	G172.85+02.27	172.86	2.28	1.71	535	G182.54-25.34	182.55	-25.34		610	G215.88-17.58	215.88	-17.58	0.42
461	G172.92-16.74	172.92	-16.74	1.43	536	G185.29-02.27	185.30	-2.28		611	G215.92-15.32	215.93	-15.33	0.42
462	G172.94-05.49	172.95	-5.49	1.75	537	G185.33-02.12	185.34	-2.13		612	G216.01-15.94	216.01	-15.95	0.42
463	G173.07-17.89	173.08	-17.90	0.23	538	G185.80-09.12	185.80	-9.12	0.24	613	G216.18-15.24	216.19	-15.25	0.42
464	G173.07-16.52	173.08	-16.53	1.29	539	G188.04-03.71	188.04	-3.71		614	G216.32-15.71	216.32	-15.71	0.42
465	G173.10+07.23	173.10	7.24		540	G190.08-13.51	190.09	-13.52		615	G216.51-13.88	216.52	-13.88	1.12
466	G173.12-13.32	173.12	-13.32	1.47	541	G190.15-14.34	190.15	-14.34	0.22	616	G216.69-13.88	216.69	-13.88	0.42
467	G173.18-09.12	173.19	-9.12		542	G190.17-13.78	190.17	-13.79	0.27	617	G216.76+02.12	216.76	2.13	12.90
468	G173.32+31.27	173.32	31.28		543	G190.50-02.29	190.50	-2.29	-1.10	618	G216.76-16.06	216.76	-16.06	0.42
469	G173.36-16.27	173.36	-16.28	1.32	544	G191.00-04.59	191.01	-4.59	0.51	619	G217.13-12.54	217.13	-12.54	1.16
470	G173.45-13.34	173.45	-13.34	1.52	545	G191.03-16.74	191.03	-16.74		620	G217.41-13.93	217.42	-13.94	0.42
471	G173.45-05.43	173.45	-5.44	0.23	546	G191.51-00.76	191.51	-0.76	0.18	621	G217.46-13.78	217.46	-13.79	0.42
472	G173.60-17.89	173.61	-17.90		547	G191.51-00.77	192.51	0.24	12.45	622	G217.70-16.12	217.71	-16.12	
473	G173.69-15.55	173.69	-15.56	0.23	548	G192.28-11.33	192.28	-11.34	0.42	623	G217.79-17.36	217.79	-17.37	0.42
474	G173.78-05.26	173.78	-5.27	0.32	549	G192.32-11.87	192.33	-11.87	0.38	624	G219.06-07.46	219.07	-7.46	0.42
475	G173.80-15.88	173.80	-15.89	1.77	550	G192.54-11.56	192.55	-11.57	0.40	625	G219.24-10.02	219.24	-10.03	1.29
476	G173.89-17.64	173.89	-17.64	1.10	551	G192.94-03.73	192.94	-3.73	1.00	626	G219.24-07.95	219.24	-7.95	0.42
477	G173.91-16.25	173.91	-16.26	0.23	552	G194.69-16.84	194.70	-16.84	0.40	627	G219.26-17.89	219.27	-17.90	0.42
478	G173.91+31.16	173.91	31.17		553	G194.80-03.41	194.81	-3.42	1.56	628	G219.28-09.27	219.29	-9.27	0.91
479	G173.95-13.74	173.96	-13.75	1.74	554	G194.94-16.74	194.94	-16.74	0.40	629	G219.30-08.15	219.31	-8.16	
480	G174.06-15.81	174.07	-15.81	1.97	555	G195.00-16.95	195.01	-16.96	0.40	630	G219.33-17.64	219.33	-17.64	0.42
481	G174.08-13.24	174.09	-13.25	1.65	556	G195.09-16.41	195.10	-16.41	0.40	631	G219.35-09.70	219.35	-9.71	0.91
482	G174.22-13.43	174.22	-13.44	1.70	557	G196.21-15.50	196.22	-15.50	0.40	632	G219.37-07.68	219.37	-7.69	0.42
483	G174.39-13.43	174.40	-13.44	1.84	558	G196.65+13.99	196.66	14.00		633	G220.67-01.86	220.67	-1.87	1.22
484	G174.44-15.75	174.44	-15.75	1.78	559	G198.03-15.24	198.04	-15.25	0.14	634	G220.95-08.32	220.96	-8.33	
485	G174.50-19.88	174.51	-19.89	0.23	560	G198.56-09.10	198.57	-9.10	2.03	635	G220.97-07.74	220.98	-7.75	
486	G174.57-13.66	174.57	-13.67	0.23	561	G198.96+01.41	198.96	1.42		636	G221.06-02.72	221.07	-2.72	
487	G174.70-15.48	174.70	-15.48	2.06	562	G199.88+00.93	199.89	0.93	0.97	637	G221.46-17.89	221.46	-17.90	
488	G174.81-15.15	174.81	-15.15	2.00	563	G200.34-10.97	200.35	-10.98		638	G221.68-17.07	221.68	-17.07	0.42
489	G174.81+05.96	174.81	5.96		564	G201.13+00.31	201.14	0.32	0.79	639	G222.01-17.13	222.01	-17.13	0.42
490	G174.88-17.11	174.88	-17.11	0.23	565	G201.26+00.46	201.27	0.47		640	G222.14-16.97	222.14	-16.98	
491	G174.99-04.83	174.99	-4.84	0.38	566	G201.44+00.65	201.45	0.65	0.53	641	G222.23+01.21	222.23	1.21	2.47
492	G175.16-16.74	175.17	-16.74	0.23	567	G201.59+00.55	201.60	0.56	0.68	642	G222.95-05.45	222.96	-5.45	0.54
493	G175.20+01.28	175.21	1.29	4.59	568	G201.84+02.81	201.84	2.82	0.76	643	G224.27-00.82	224.27	-0.82	1.42
494	G175.31-20.50	175.32	-20.50		569	G202.21-09.17	202.21	-9.18	0.42	644	G224.47-00.65	224.47	-0.65	1.52
495	G175.34-10.82	175.34	-10.83	0.23	570	G202.30-08.91	202.30	-8.91	0.41	645	G226.16-00.41	226.16	-0.41	1.05
496	G175.49-16.80	175.50	-16.80	1.96	571	G202.58-08.70	202.59	-8.71	0.42	646	G226.29-00.63	226.30	-0.63	
497	G175.53+01.34	175.54	1.34		572	G203.00-03.69	203.01	-3.70	0.18	647	G226.36-00.50	226.36	-0.50	0.77
498	G175.58-16.60	175.58	-16.61	0.23	573	G203.11-08.70	203.12	-8.71	0.42	648	G226.38+01.30	226.38	1.31	0.88
499	G175.97-20.38	175.98	-20.38		574	G203.20-11.20	203.20	-11.21	0.41	649	G226.71-07.46	226.71	-7.46</	

**Table A.4.** Continued

Num	Name	Glon °	Glat °	Dist kpc	Num	Name	Glon °	Glat °	Dist kpc	Num	Name	Glon °	Glat °	Dist kpc
661	G236.68-05.21	236.69	-5.21		665	G238.71-01.47	238.71	-1.47	1.13	669	G353.54+15.73	353.54	15.73	0.12
662	G237.30-04.76	237.30	-4.76		666	G239.58-04.61	239.59	-4.61		670	G354.17+15.32	354.18	15.33	0.12
663	G238.44-04.16	238.45	-4.16		667	G240.99-01.21	241.00	-1.21	6.15	671	G354.19+16.27	354.20	16.28	0.12
664	G238.51-03.88	238.51	-3.88	1.00	668	G353.49+15.57	353.50	15.58	0.12	672	G354.46+16.15	354.46	16.16	0.12

**Table A.2.** Observed parameters of the NH<sub>3</sub> (1,1) and NH<sub>3</sub> (2,2) emission lines in the NH<sub>3</sub> detected sources.

Name	$V_{\text{LSR}}(1,1)$ km s <sup>-1</sup>	$\Delta v(1,1)$ km s <sup>-1</sup>	$\tau(1,1)$	$T_{\text{MB}}(1,1)$ K	$V_{\text{LSR}}(2,2)$ km s <sup>-1</sup>	$\Delta v(2,2)$ km s <sup>-1</sup>	$T_{\text{MB}}(2,2)$ K
G005.03+19.07	3.88(0.03)	0.76(0.06)		0.07(0.01)			
G005.29+11.07	4.04(0.03)	0.83(0.08)	0.64(0.47)	0.12(0.01)			
G005.69+36.84	1.76(0.04)	0.48(0.08)		0.03(0.01)			
G005.80+19.92	2.79(0.04)	0.65(0.09)		0.27(0.04)			
G006.04+36.74	2.37(0.02)	0.68(0.04)	4.16(0.30)	1.11(0.09)	2.30(0.03)	0.32(0.06)	0.20(0.03)
G006.08+20.26	3.96(0.05)	0.92(0.14)		0.21(0.04)			
G006.32+20.44	4.13(0.01)	0.69(0.03)	0.85(0.10)	0.71(0.04)	4.21(0.02)	0.50(0.05)	0.12(0.01)
G006.41+20.56	4.30(0.02)	0.68(0.05)		0.40(0.04)			
G006.70+20.66	3.55(0.02)	0.84(0.04)	0.39(0.15)	0.37(0.02)	3.46(0.04)	0.57(0.12)	0.06(0.01)
G006.94+05.84	9.82(0.02)	0.76(0.05)	1.94(0.44)	0.34(0.03)			
G006.98+20.72	2.95(0.03)	0.71(0.06)	1.04(0.56)	0.13(0.01)	2.97(0.04)	0.40(0.07)	0.06(0.01)
G007.14+05.94	10.28(0.03)	0.92(0.07)	2.25(0.35)	0.51(0.05)			
G007.53+21.10	2.91(0.02)	0.79(0.04)		0.22(0.02)	2.94(0.05)	0.75(0.14)	0.05(0.01)
G007.80+21.10	3.55(0.10)	0.90(0.18)	1.43(0.69)	0.08(0.01)	3.45(0.13)	1.20(0.27)	0.03(0.01)
G008.52+21.84	3.66(0.03)	0.60(0.06)	0.97(0.69)	0.23(0.03)			
G008.67+22.14	3.39(0.02)	0.65(0.03)	3.88(0.18)	0.61(0.04)	3.39(0.02)	0.28(0.07)	0.10(0.01)
G009.79+00.87	28.85(0.05)	1.83(0.14)	2.07(0.20)	0.30(0.04)	28.79(0.08)	0.94(0.21)	0.08(0.02)
G011.09+03.43	6.56(0.03)	0.65(0.05)	2.81(0.80)	0.08(0.01)			
G015.16+07.23	2.68(0.04)	0.86(0.12)		0.08(0.01)			
G018.61+08.87	6.74(0.03)	0.57(0.07)		0.13(0.02)			
G020.52+01.69	27.12(0.04)	1.00(0.09)	1.10(0.54)	0.19(0.03)			
G021.20+04.96	3.42(0.03)	0.79(0.06)	2.52(0.77)	0.24(0.03)			
G021.66+03.78	6.73(0.03)	0.89(0.07)	1.19(0.44)	0.29(0.03)			
G023.37+08.21	7.81(0.04)	0.75(0.09)	3.07(0.94)	0.21(0.03)			
G023.68+07.53	7.69(0.04)	0.77(0.10)	2.82(0.91)	0.13(0.02)			
G025.48+06.18	7.63(0.02)	0.67(0.05)	2.53(0.62)	0.41(0.04)			
G026.85+06.78	7.05(0.02)	0.67(0.06)	1.67(0.54)	0.28(0.03)			
G027.66+05.71	8.03(0.02)	0.75(0.05)	0.10(0.12)	0.13(0.01)			
G028.45-06.39	11.95(0.03)	0.81(0.06)	0.89(0.39)	0.30(0.03)			
G028.56-00.24	85.18(0.29)	1.79(0.51)	0.51(0.16)	0.39(0.11)	85.18(0.06)	1.82(0.14)	0.15(0.01)
G028.71+03.88	7.52(0.03)	0.94(0.07)	5.35(0.01)	0.80(0.09)	7.47(0.01)	0.60(0.04)	0.22(0.01)
G028.87+04.23	6.57(0.02)	0.76(0.04)	1.93(0.19)	0.29(0.02)	6.57(0.12)	0.65(0.43)	0.03(0.01)
G030.43+02.35	9.03(0.04)	1.11(0.10)	1.66(0.45)	0.27(0.04)			
G030.78+05.22	8.06(0.03)	1.22(0.06)	1.56(0.10)	0.47(0.04)	7.98(0.03)	1.13(0.07)	0.12(0.01)
G031.44+04.18	10.93(0.03)	1.00(0.08)	0.79(0.38)	0.28(0.03)			
G032.93+02.68	11.53(0.03)	0.86(0.08)	0.49(0.36)	0.34(0.03)			
G038.36-00.95	16.62(0.03)	1.29(0.07)	1.42(0.15)	0.77(0.07)	16.66(0.06)	1.04(0.12)	0.16(0.03)
G049.76-07.25	21.45(0.02)	0.77(0.06)	0.42(0.38)	0.14(0.01)	30.26(0.05)	0.42(0.12)	0.04(0.01)
G057.10+03.65	11.59(0.05)	1.10(0.09)	1.97(0.50)	0.19(0.03)			
G065.43-03.15	5.93(0.04)	1.04(0.11)	1.37(0.50)	0.21(0.03)			
G070.44-01.54	10.90(0.03)	1.71(0.08)	1.34(0.49)	0.24(0.02)	10.81(0.07)	1.77(0.17)	0.05(0.01)
G070.72-00.63	12.11(0.07)	1.52(0.19)		0.05(0.01)			
G074.11+00.11a	-2.23(0.17)	1.25(0.17)	0.96(0.37)	0.20(0.03)			
G074.11+00.11b	-0.77(0.17)	1.19(0.17)	0.86(0.50)	0.22(0.03)			
G084.79-01.11	0.85(0.04)	1.57(0.08)	1.84(0.15)	0.85(0.09)	0.91(0.07)	1.27(0.13)	0.17(0.04)
G089.36-00.67	2.51(0.02)	1.13(0.06)	1.12(0.01)	0.30(0.02)	2.53(0.06)	1.01(0.24)	0.05(0.01)
G089.62+02.16	-0.40(0.02)	0.87(0.05)	3.35(0.16)	0.46(0.04)	-0.39(0.03)	0.37(0.06)	0.08(0.01)
G089.64-06.59	12.35(0.04)	0.88(0.09)		0.06(0.01)			
G089.75-02.16	1.87(0.05)	1.17(0.11)	1.55(0.46)	0.05(0.01)			
G089.93-01.94	1.45(0.04)	1.12(0.09)	1.92(0.53)	0.10(0.01)			
G091.73+04.36	-4.55(0.02)	0.89(0.05)	1.77(0.13)	0.40(0.03)	-4.51(0.06)	0.84(0.13)	0.04(0.01)
G092.02+03.93	-1.66(0.03)	0.87(0.07)	0.35(0.41)	0.25(0.03)			
G092.26+03.80	-1.87(0.03)	1.22(0.07)	2.55(0.09)	0.55(0.05)	-1.89(0.04)	1.06(0.10)	0.10(0.01)
G093.20+09.53	-1.84(0.12)	0.51(0.19)	5.15(0.43)	0.17(0.03)	-2.01(0.04)	0.41(0.11)	0.04(0.01)
G093.22-04.59	3.97(0.09)	0.79(0.17)	1.83(0.87)	0.10(0.01)			
G093.62-04.44	3.61(0.03)	0.88(0.07)	0.78(0.41)	0.24(0.03)	3.68(0.10)	0.83(0.25)	0.08(0.03)
G093.91+10.02	-1.96(0.03)	0.80(0.06)	2.88(0.48)	0.13(0.01)	-2.06(0.07)	0.58(0.14)	0.03(0.01)
G093.99-04.91	4.79(0.02)	0.78(0.04)	2.60(0.35)	0.16(0.01)	4.79(0.08)	0.82(0.18)	0.03(0.01)
G094.08+09.46	0.02(0.02)	0.84(0.05)	3.02(0.18)	0.30(0.03)	-0.09(0.06)	0.68(0.17)	0.04(0.01)
G095.51+09.97	-2.75(0.02)	0.78(0.06)	0.58(0.40)	0.12(0.01)			
G095.75+08.17	0.37(0.02)	0.76(0.05)	0.44(0.34)	0.11(0.01)	0.18(0.04)	0.32(0.09)	0.04(0.01)
G096.59+10.29	-2.71(0.02)	0.68(0.06)	0.47(0.52)	0.11(0.01)	-3.51(0.04)	0.29(0.08)	0.04(0.01)
G096.94+10.25	-2.65(0.02)	0.60(0.05)	1.91(0.63)	0.24(0.02)			
G097.09+10.12	-2.65(0.02)	0.79(0.05)	3.78(0.19)	0.43(0.04)	-2.72(0.05)	0.51(0.09)	0.05(0.01)

**Table A.2.** Continued

Name	$V_{\text{LSR}}(1, 1)$ km s $^{-1}$	$\Delta v(1, 1)$ km s $^{-1}$	$\tau(1, 1)$	$T_{\text{MB}}(1, 1)$ K	$V_{\text{LSR}}(2, 2)$ km s $^{-1}$	$\Delta v(2, 2)$ km s $^{-1}$	$T_{\text{MB}}(2, 2)$ K
G097.20+09.87	-2.59(0.04)	1.02(0.08)	1.92(0.47)	0.25(0.03)			
G097.38+09.95	-2.38(0.03)	0.75(0.06)	3.20(0.67)	0.12(0.01)			
G098.52+13.88	-3.21(0.02)	0.69(0.05)	0.88(0.50)	0.13(0.01)			
G098.89+14.01	-2.85(0.02)	0.71(0.04)	2.37(0.34)	0.22(0.02)	-2.73(0.04)	0.28(0.10)	0.04(0.01)
G098.96+13.68	-2.91(0.03)	0.62(0.07)	1.60(0.85)	0.05(0.01)			
G102.34+15.96	2.44(0.02)	0.76(0.04)	2.98(0.15)	0.72(0.05)	2.39(0.05)	0.66(0.10)	0.08(0.02)
G102.70+15.19	1.81(0.02)	0.71(0.04)	2.14(0.39)	0.18(0.01)			
G102.72+15.36	1.17(0.02)	0.71(0.05)	2.99(0.53)	0.29(0.03)			
G103.90+13.97	2.73(0.02)	0.76(0.04)	2.71(0.21)	0.44(0.03)	2.71(0.02)	0.39(0.05)	0.09(0.01)
G108.10+13.19	-5.54(0.02)	0.73(0.05)	3.07(0.48)	0.34(0.03)			
G110.65+09.65	-4.60(0.02)	0.92(0.05)	2.35(0.15)	0.54(0.04)	-4.54(0.04)	0.68(0.07)	0.10(0.02)
G111.66+20.20	-8.24(0.02)	0.83(0.04)	2.16(0.08)	0.53(0.04)	-8.24(0.02)	0.61(0.05)	0.08(0.01)
G111.68+19.74	-9.06(0.02)	0.80(0.06)	1.60(0.44)	0.08(0.01)			
G111.77+20.26	-8.41(0.03)	0.64(0.06)	1.78(0.95)	0.14(0.02)			
G114.16+14.80	-4.39(0.02)	0.63(0.05)	4.29(0.54)	0.45(0.04)			
G114.56+14.72	-4.58(0.06)	0.55(0.10)		0.02(0.01)			
G114.67+14.47	-4.56(0.02)	1.11(0.06)	1.89(0.11)	0.77(0.06)	-4.47(0.06)	1.11(0.16)	0.07(0.01)
G115.81-03.54	-0.97(0.01)	0.65(0.03)	1.67(0.24)	0.44(0.03)	-1.07(0.07)	0.59(0.20)	0.05(0.01)
G116.08-02.38	-1.13(0.04)	1.42(0.09)	0.10(0.10)	0.07(0.01)			
G117.11+12.42	3.84(0.02)	0.79(0.05)	3.17(0.28)	0.60(0.05)	3.87(0.05)	0.33(0.11)	0.11(0.03)
G120.16+03.09	-19.83(0.17)	1.02(0.17)	0.31(0.53)	0.18(0.03)			
G120.67+02.66	-16.95(0.02)	0.87(0.05)	0.88(0.29)	0.21(0.02)	-17.02(0.04)	0.59(0.10)	0.07(0.01)
G120.98+02.66	-17.30(0.04)	1.35(0.08)	1.10(0.27)	0.12(0.01)			
G121.35+03.39	-5.51(0.04)	0.71(0.11)	2.32(0.92)	0.21(0.04)			
G123.66+24.89	-3.72(0.10)	0.55(0.19)		0.01(0.00)			
G127.85+14.16	2.64(0.03)	0.64(0.07)		0.11(0.02)			
G127.88+02.66	-11.70(0.03)	0.96(0.07)	1.47(0.45)	0.10(0.01)			
G128.89+13.68	3.80(0.02)	0.80(0.05)	3.03(0.32)	0.39(0.04)	3.95(0.10)	0.77(0.26)	0.05(0.02)
G128.95-00.18	-14.83(0.03)	0.66(0.05)		0.06(0.01)			
G132.29+09.36	-12.52(0.04)	1.32(0.09)	0.65(0.28)	0.11(0.01)			
G133.28+08.81	-11.09(0.04)	1.09(0.09)		0.06(0.01)			
G133.48+09.02a	-16.99(0.11)	1.58(0.20)	0.75(0.11)	0.24(0.03)	-16.56(0.11)	2.34(0.27)	0.05(0.01)
G133.48+09.02b	-15.23(0.17)	1.70(0.30)	0.70(0.20)	0.17(0.03)			
G140.97+05.73	-11.68(0.06)	1.05(0.12)		0.06(0.01)			
G144.66+00.16	-7.88(0.02)	0.69(0.05)	2.51(0.58)	0.15(0.01)			
G147.01+03.39	-4.75(0.02)	0.76(0.04)	1.95(0.28)	0.27(0.02)			
G149.23+03.07	2.98(0.06)	1.30(0.12)		0.06(0.01)			
G149.41+03.37	3.35(0.04)	0.95(0.09)	0.10(0.45)	0.07(0.01)			
G149.52-01.23	-8.06(0.24)	1.33(0.43)	0.87(0.56)	0.07(0.01)			
G150.22+03.91	3.07(0.03)	0.60(0.06)	0.79(0.01)	0.24(0.03)			
G150.35-38.06	4.86(0.02)	0.72(0.06)	0.10(0.35)	0.10(0.01)			
G150.44+03.95	3.31(0.03)	0.63(0.05)	4.10(0.70)	0.36(0.04)			
G151.08+04.46	3.15(0.02)	0.66(0.04)	1.45(0.43)	0.49(0.04)			
G151.45+03.95	1.82(0.04)	1.20(0.09)	0.81(0.33)	0.10(0.01)			
G154.07+05.09	4.43(0.05)	1.63(0.12)	0.94(0.33)	0.06(0.01)			
G154.07+05.21	4.39(0.04)	0.91(0.12)		0.17(0.03)			
G154.68-15.34	3.18(0.03)	0.58(0.07)		0.24(0.03)			
G154.90+04.61a	2.82(0.13)	0.84(0.18)	0.77(0.32)	0.06(0.01)			
G154.90+04.61b	3.69(0.13)	0.99(0.24)	0.48(0.75)	0.08(0.01)			
G155.45-14.59	1.67(0.03)	0.81(0.09)	0.10(8.91)	0.10(0.01)			
G155.67+05.11	4.43(0.04)	0.90(0.09)		0.17(0.02)			
G156.20+05.26	5.36(0.02)	0.62(0.05)	0.10(0.13)	0.26(0.02)			
G156.90-08.49	-7.92(0.04)	0.63(0.10)		0.05(0.01)			
G157.10-08.70	-7.51(0.04)	0.74(0.09)		0.06(0.01)			
G157.12-11.56	-1.68(0.02)	1.08(0.06)	0.10(0.23)	0.14(0.01)			
G157.25-01.00	5.20(0.04)	0.69(0.10)		0.15(0.03)			
G157.60-12.17	-7.73(0.03)	0.88(0.06)	1.43(0.43)	0.23(0.02)			
G158.20-20.28	7.39(0.01)	0.70(0.03)	2.13(0.14)	0.60(0.04)	7.38(0.03)	0.46(0.09)	0.07(0.01)
G158.22-20.14	8.12(0.01)	0.67(0.03)	1.88(0.11)	0.83(0.05)	8.13(0.02)	0.35(0.05)	0.10(0.01)
G158.24-21.80	3.92(0.02)	0.77(0.05)		0.23(0.02)			
G158.37-20.72	7.08(0.02)	0.93(0.05)	1.61(0.09)	0.52(0.04)	6.99(0.04)	0.40(0.10)	0.06(0.01)
G158.77-33.30	-2.64(0.04)	1.13(0.10)	0.95(0.44)	0.08(0.01)			
G158.86-21.60	4.73(0.02)	0.87(0.04)	0.64(0.17)	0.33(0.02)	4.81(0.05)	0.50(0.11)	0.07(0.02)
G159.01-08.46	-4.72(0.03)	0.90(0.08)	1.17(0.41)	0.12(0.01)			
G159.21-20.44	6.35(0.02)	1.02(0.05)	2.13(0.07)	1.05(0.08)	6.30(0.02)	0.82(0.04)	0.20(0.01)
G159.21-20.12	6.44(0.04)	0.70(0.08)		0.14(0.02)			
G159.23-34.49	-5.39(0.03)	1.05(0.06)	1.11(0.31)	0.18(0.02)			
G159.34+11.20	2.30(0.06)	0.58(0.16)		0.09(0.02)			
G159.41-34.36	-5.36(0.03)	0.86(0.07)	0.36(0.41)	0.19(0.02)			
G159.65-19.68	2.14(0.04)	1.09(0.09)	1.32(0.49)	0.06(0.01)			
G159.65+11.39	7.28(0.04)	0.79(0.09)		0.13(0.02)			
G159.67-34.31	-1.58(0.04)	0.89(0.12)		0.06(0.01)			
G159.76-19.62	7.72(0.06)	1.45(0.14)		0.06(0.01)			
G160.51-16.84	10.03(0.02)	0.86(0.04)	0.92(0.19)	0.24(0.02)	10.03(0.05)	0.51(0.20)	0.05(0.01)

**Table A.2.** Continued

Name	$V_{\text{LSR}}(1, 1)$ km s $^{-1}$	$\Delta v(1, 1)$ km s $^{-1}$	$\tau(1, 1)$	$T_{\text{MB}}(1, 1)$ K	$V_{\text{LSR}}(2, 2)$ km s $^{-1}$	$\Delta v(2, 2)$ km s $^{-1}$	$T_{\text{MB}}(2, 2)$ K
G160.53-19.72	-3.84(0.02)	0.99(0.05)	0.58(0.23)	0.38(0.03)			
G160.53-09.84	3.50(0.02)	0.87(0.05)		0.11(0.01)			
G161.21-08.72	-3.86(0.02)	0.62(0.05)	1.68(0.65)	0.22(0.02)			
G161.43-35.59	-5.87(0.05)	0.87(0.10)		0.12(0.02)			
G161.60-08.34	-3.26(0.03)	0.68(0.08)		0.12(0.02)			
G161.85-08.66	-2.50(0.03)	0.70(0.06)	2.54(0.71)	0.22(0.03)			
G161.85-35.75	-6.91(0.04)	0.86(0.13)	2.00(0.90)	0.20(0.03)			
G162.46-08.70	-1.21(0.02)	0.86(0.06)	0.99(0.33)	0.34(0.03)			
G163.21-08.40	-2.40(0.05)	1.21(0.12)		0.10(0.02)			
G163.32-08.42	-2.04(0.03)	0.87(0.06)	2.91(0.35)	0.38(0.04)			
G163.67-08.34	-2.04(0.06)	0.92(0.18)		0.24(0.05)			
G164.94-08.57	-0.85(0.02)	0.88(0.04)	0.88(0.11)	0.45(0.03)	-0.88(0.11)	1.04(0.24)	0.03(0.01)
G165.16-07.55	-0.83(0.03)	0.62(0.07)		0.10(0.01)			
G165.34-07.51a	-1.71(0.06)	0.47(0.14)		0.04(0.01)			
G165.34-07.51b	-0.64(0.11)	1.22(0.30)		0.04(0.01)			
G165.69-09.14	-0.82(0.02)	0.72(0.04)	2.16(0.38)	0.47(0.04)			
G168.00-15.69	7.30(0.04)	0.55(0.09)		0.12(0.02)			
G168.13-16.39	6.26(0.01)	0.62(0.03)	1.53(0.22)	0.51(0.03)	6.20(0.04)	0.34(0.08)	0.07(0.01)
G168.72-15.48	7.15(0.02)	0.60(0.04)	2.03(0.44)	0.54(0.04)			
G168.85-15.83	6.29(0.05)	1.33(0.11)	1.35(0.47)	0.16(0.02)			
G169.32-16.15a	5.00(0.04)	0.73(0.11)		0.21(0.03)			
G169.32-16.15b	6.77(0.04)	0.93(0.11)		0.21(0.03)			
G169.43-16.17	5.43(0.03)	1.29(0.07)	0.37(0.24)	0.31(0.03)			
G169.76-16.15a	5.25(0.04)	0.98(0.12)		0.17(0.03)			
G169.76-16.15b	6.65(0.03)	0.72(0.08)		0.22(0.03)			
G169.84-07.61	6.38(0.03)	0.67(0.06)		0.10(0.01)			
G169.98-18.97	7.52(0.05)	0.68(0.11)		0.09(0.02)			
G169.98-04.27	7.66(0.02)	0.76(0.03)	1.30(0.00)	0.34(0.02)	7.69(0.02)	0.21(0.06)	0.08(0.01)
G170.00-16.14	6.59(0.01)	0.60(0.03)	1.13(0.32)	0.30(0.02)	6.64(0.05)	0.31(0.08)	0.05(0.01)
G170.13-16.06	6.78(0.02)	0.81(0.05)	1.19(0.35)	0.43(0.04)			
G170.26-16.02	6.56(0.02)	0.74(0.04)	4.01(0.19)	0.65(0.05)	6.59(0.03)	0.39(0.07)	0.09(0.01)
G170.81-18.34	7.87(0.04)	0.79(0.09)	3.04(0.98)	0.07(0.01)			
G170.88-10.92	5.85(0.02)	0.61(0.04)	1.43(0.55)	0.34(0.03)			
G170.99-15.81	6.26(0.04)	0.90(0.09)	0.90(0.31)	0.22(0.03)			
G171.14-17.58	7.37(0.04)	0.62(0.07)		0.15(0.03)			
G171.34+02.59	-19.58(0.06)	2.36(0.15)	0.10(0.66)	0.10(0.01)			
G171.49-14.90	6.40(0.02)	0.74(0.04)	4.35(0.13)	1.04(0.08)	6.42(0.02)	0.35(0.04)	0.14(0.01)
G171.51-10.59	5.96(0.02)	0.67(0.05)	3.30(0.74)	0.31(0.03)			
G171.80-15.32	6.75(0.02)	0.69(0.03)	3.30(0.22)	0.69(0.05)	6.76(0.03)	0.34(0.06)	0.08(0.01)
G171.84-05.22	6.96(0.02)	0.65(0.04)	2.78(0.40)	0.62(0.05)			
G172.06-15.21	6.57(0.04)	0.52(0.10)		0.14(0.03)			
G172.13-16.93	7.00(0.02)	0.67(0.04)	1.12(0.40)	0.35(0.03)			
G172.85+02.27	-17.67(0.03)	1.57(0.07)	0.90(0.12)	0.22(0.02)	-17.66(0.05)	1.34(0.12)	0.08(0.01)
G172.92-16.74	4.71(0.13)	0.96(0.29)		0.03(0.01)			
G172.94-05.49	6.76(0.03)	0.47(0.06)		0.23(0.03)			
G173.12-13.32	5.15(0.02)	0.53(0.05)		0.11(0.01)			
G173.36-16.27	6.28(0.02)	0.70(0.04)	2.14(0.22)	0.47(0.03)	6.32(0.04)	0.30(0.07)	0.06(0.01)
G173.45-13.34	5.22(0.04)	0.36(0.07)	3.64(0.26)	0.48(0.04)			
G173.80-15.88	5.81(0.02)	0.70(0.04)	2.74(0.03)	0.90(0.06)	5.88(0.02)	0.25(0.07)	0.11(0.01)
G173.89-17.64	5.03(0.04)	0.63(0.07)		0.14(0.02)			
G173.95-13.74	6.43(0.04)	0.88(0.11)	1.17(0.68)	0.19(0.03)			
G174.06-15.81	6.09(0.02)	0.75(0.04)	1.83(0.17)	0.80(0.05)			
G174.08-13.24	5.15(0.02)	0.70(0.04)	3.28(0.15)	0.90(0.06)	5.18(0.03)	0.41(0.09)	0.10(0.01)
G174.22-13.43	5.76(0.02)	1.05(0.05)	1.10(0.08)	0.63(0.05)	6.01(0.04)	0.24(0.07)	0.06(0.01)
G174.39-13.43	5.62(0.02)	0.72(0.05)	0.58(0.39)	0.34(0.03)			
G174.44-15.75	6.58(0.04)	1.03(0.09)		0.17(0.02)			
G174.70-15.48	5.82(0.02)	0.76(0.04)	1.51(0.14)	0.58(0.04)	5.86(0.05)	0.56(0.13)	0.05(0.01)
G174.81-15.15	5.72(0.03)	0.61(0.06)		0.15(0.02)			
G175.49-16.80	5.43(0.01)	0.66(0.03)	2.48(0.09)	0.87(0.05)	5.41(0.02)	0.31(0.05)	0.10(0.01)
G177.14-01.21	-17.32(0.05)	1.64(0.13)	0.52(0.27)	0.12(0.02)			
G177.86+01.04	-18.22(0.15)	1.47(0.36)		0.03(0.01)			
G177.89-20.16	6.88(0.04)	0.59(0.10)		0.11(0.02)			
G177.97-09.72	7.11(0.02)	0.79(0.05)	4.59(0.21)	0.81(0.07)	7.09(0.03)	0.40(0.08)	0.14(0.03)
G178.28-00.61	-1.11(0.05)	0.84(0.13)	1.99(0.77)	0.08(0.01)			
G178.98-06.74	7.61(0.02)	0.66(0.04)	3.86(0.26)	0.44(0.03)			
G180.81-19.66	8.74(0.03)	0.70(0.09)		0.17(0.02)			
G180.92+04.53	1.52(0.03)	1.02(0.08)	1.84(0.40)	0.35(0.04)			
G181.73-19.35	8.67(0.03)	0.82(0.09)		0.07(0.01)			
G181.84+00.31	2.95(0.02)	1.05(0.05)	1.28(0.19)	0.27(0.02)			
G182.04+00.41	2.50(0.04)	1.06(0.08)	0.98(0.42)	0.09(0.01)			
G190.17-13.78	1.03(0.04)	0.86(0.11)		0.12(0.02)			
G191.51-00.76	0.08(0.03)	0.87(0.07)	0.25(0.39)	0.09(0.01)			
G192.12-10.90	9.87(0.02)	0.67(0.05)	0.10(0.42)	0.16(0.01)			
G192.28-11.33	9.96(0.04)	0.88(0.08)	0.94(0.55)	0.09(0.01)			
G192.32-11.87	11.98(0.03)	0.96(0.06)	1.47(0.26)	0.39(0.04)			

**Table A.2.** Continued

Name	$V_{\text{LSR}}(1, 1)$ km s $^{-1}$	$\Delta v(1, 1)$ km s $^{-1}$	$\tau(1, 1)$	$T_{\text{MB}}(1, 1)$ K	$V_{\text{LSR}}(2, 2)$ km s $^{-1}$	$\Delta v(2, 2)$ km s $^{-1}$	$T_{\text{MB}}(2, 2)$ K
G192.94-03.73	4.00(0.05)	1.36(0.12)		0.05(0.01)			
G194.80-03.41	12.14(0.04)	1.24(0.10)	1.25(0.35)	0.11(0.01)			
G198.03-15.24	-0.13(0.03)	0.94(0.07)	0.40(0.43)	0.07(0.01)			
G198.56-09.10	11.25(0.02)	0.72(0.05)	1.39(0.44)	0.41(0.04)			
G199.88+00.93	5.70(0.03)	0.98(0.07)	1.42(0.35)	0.33(0.04)			
G201.13+00.31	4.75(0.04)	0.90(0.08)	1.24(0.60)	0.15(0.02)			
G201.44+00.65	6.32(0.02)	0.89(0.05)	1.35(0.25)	0.30(0.02)	6.26(0.05)	0.41(0.14)	0.05(0.01)
G201.59+00.55a	3.94(0.05)	1.21(0.11)	0.71(0.15)	0.31(0.03)	4.28(0.14)	1.75(0.25)	0.04(0.01)
G201.59+00.55b	5.13(0.05)	0.77(0.10)	1.42(0.39)	0.20(0.03)			
G202.30-08.91	11.83(0.02)	1.16(0.05)	0.55(0.10)	0.24(0.02)	12.07(0.07)	0.73(0.14)	0.03(0.01)
G203.20-11.20	10.35(0.02)	1.09(0.05)	1.40(0.10)	0.41(0.03)	10.61(0.13)	0.66(0.45)	0.04(0.01)
G203.75-08.49	11.57(0.04)	0.64(0.09)		0.06(0.01)			
G204.82-13.88	8.06(0.04)	1.13(0.12)	0.30(0.42)	0.17(0.02)			
G205.57-08.25	11.47(0.04)	0.66(0.09)		0.06(0.01)			
G206.10-15.77	9.09(0.02)	0.67(0.04)	2.64(0.20)	0.64(0.05)	9.13(0.02)	0.43(0.05)	0.11(0.01)
G206.60-14.40	3.95(0.05)	1.44(0.12)	0.51(0.36)	0.08(0.01)			
G208.56+02.36	9.20(0.05)	0.88(0.13)		0.06(0.01)			
G209.28-19.62a	7.57(0.16)	1.71(0.30)	0.24(0.20)	0.20(0.03)			
G209.28-19.62b	8.92(0.05)	0.98(0.11)		0.32(0.03)	8.29(0.10)	1.34(0.23)	0.06(0.01)
G211.48-19.27	3.79(0.04)	1.61(0.09)	0.95(0.14)	0.34(0.04)	3.66(0.07)	0.99(0.17)	0.06(0.01)
G212.10-19.15	4.30(0.02)	1.04(0.06)	1.52(0.10)	0.54(0.04)	4.24(0.09)	1.26(0.18)	0.04(0.01)
G214.21-13.40	11.95(0.03)	0.85(0.08)	0.10(1.19)	0.21(0.02)			
G214.43-19.90	2.76(0.03)	0.97(0.07)	0.66(0.35)	0.26(0.03)			
G216.51-13.88	9.86(0.04)	0.78(0.09)	2.97(0.92)	0.15(0.02)			
G217.13-12.54	11.53(0.03)	0.64(0.05)		0.10(0.01)			
G219.24-10.02	12.28(0.03)	0.73(0.08)		0.12(0.02)			
G220.67-01.86	12.08(0.03)	1.11(0.07)	1.22(0.26)	0.28(0.03)			
G222.23+01.21	28.44(0.05)	1.09(0.13)	1.31(0.60)	0.06(0.01)			
G224.27-00.82	14.10(0.03)	1.44(0.07)	1.61(0.09)	0.57(0.05)	14.19(0.05)	1.32(0.12)	0.08(0.01)
G224.47-00.65	15.57(0.02)	1.22(0.07)	0.93(0.11)	0.44(0.04)	15.45(0.05)	0.70(0.12)	0.07(0.01)
G238.71-01.47	19.25(0.06)	1.65(0.13)	0.97(0.38)	0.10(0.01)			
G353.49+15.57	4.13(0.02)	0.80(0.03)	1.47(0.08)	1.04(0.06)	4.12(0.02)	0.66(0.05)	0.20(0.02)
G353.54+15.73	4.29(0.02)	0.87(0.04)	1.34(0.11)	1.40(0.09)	4.35(0.04)	0.66(0.11)	0.23(0.04)
G354.17+15.32	3.51(0.01)	0.65(0.03)	0.64(0.22)	0.40(0.02)	3.55(0.03)	0.29(0.07)	0.08(0.02)
G354.19+16.27	2.54(0.02)	0.83(0.04)	0.84(0.15)	0.37(0.02)	2.50(0.05)	0.66(0.16)	0.06(0.01)
G354.46+16.15	2.43(0.01)	0.70(0.03)	2.05(0.09)	1.16(0.07)	2.41(0.02)	0.39(0.04)	0.15(0.02)

**Table A.3.** Calculated parameters of the NH<sub>3</sub> (1,1) and (2,2) emission lines detected in the 73 cores.

Name	T <sub>ex</sub> K	T <sub>rot</sub> K	T <sub>kin</sub> K	N <sub>NH<sub>3</sub></sub> 10 <sup>15</sup> cm <sup>-2</sup>	σ <sub>NT</sub> km s <sup>-1</sup>	σ <sub>TH</sub> km s <sup>-1</sup>	c <sub>s</sub> km s <sup>-1</sup>	M	R <sub>P</sub>	χ 10 <sup>-7</sup>
G006.04+36.74	3.8(1.1)	9.6(0.1)	10.0(0.1)	3.6(0.2)	0.40(0.01)	0.07(0.01)	0.19(0.01)	2.2(0.2)	0.03(0.01)	...
G006.32+20.44	3.9(1.2)	12.3(0.1)	13.4(0.1)	0.7(0.1)	0.41(0.01)	0.08(0.01)	0.22(0.01)	1.9(0.1)	0.04(0.01)	0.6(0.1)
G006.70+20.66	3.9(0.8)	13.0(0.4)	14.2(0.5)	0.4(0.1)	0.50(0.01)	0.08(0.01)	0.22(0.01)	2.3(0.1)	0.03(0.01)	0.3(0.1)
G006.98+20.72	2.9(0.1)	17.2(0.4)	20.2(0.6)	0.9(0.3)	0.41(0.01)	0.10(0.01)	0.27(0.01)	1.6(0.1)	0.06(0.01)	1.4(0.3)
G007.80+21.10	2.8(0.1)	14.4(0.3)	16.1(0.4)	1.4(0.5)	0.53(0.02)	0.09(0.01)	0.24(0.01)	2.3(0.7)	0.03(0.01)	2.5(0.6)
G008.67+22.14	3.3(0.6)	9.4(0.1)	9.8(0.1)	3.3(0.1)	0.39(0.01)	0.07(0.01)	0.18(0.01)	2.1(0.2)	0.03(0.01)	4.6(0.1)
G009.79+00.87	3.0(0.3)	12.6(0.1)	13.8(0.1)	4.2(0.3)	1.09(0.01)	0.08(0.01)	0.22(0.01)	5.0(1.4)	0.01(0.01)	...
G028.56-00.24	3.7(0.8)	17.6(2.0)	20.7(3.2)	1.1(0.3)	1.07(0.02)	0.10(0.01)	0.27(0.02)	4.0(3.1)	0.01(0.01)	...
G028.71+03.88	3.5(0.8)	10.2(0.1)	10.7(0.2)	6.1(0.1)	0.56(0.01)	0.07(0.01)	0.19(0.01)	2.9(0.4)	0.02(0.01)	...
G028.87+04.23	3.0(0.3)	9.9(0.3)	10.3(0.3)	1.8(0.1)	0.45(0.01)	0.07(0.01)	0.19(0.01)	2.4(0.2)	0.02(0.01)	...
G030.78+05.22	3.3(0.6)	12.8(0.1)	14.0(0.1)	2.1(0.1)	0.73(0.01)	0.08(0.01)	0.22(0.01)	3.3(0.4)	0.01(0.01)	...
G038.36-00.95	3.7(1.0)	12.2(0.2)	13.2(0.3)	2.1(0.1)	0.77(0.01)	0.08(0.01)	0.21(0.01)	3.6(0.5)	0.01(0.01)	1.6(0.1)
G049.76-07.25	3.1(0.1)	15.8(0.2)	18.1(0.3)	0.4(0.2)	0.45(0.01)	0.09(0.01)	0.25(0.01)	1.8(0.2)	0.04(0.01)	0.9(0.3)
G070.44-01.54	3.0(0.3)	11.9(0.3)	12.9(0.3)	2.6(0.5)	1.02(0.01)	0.08(0.01)	0.21(0.01)	4.9(0.8)	0.01(0.01)	2.5(0.1)
G084.79-01.11	3.7(1.0)	11.6(0.3)	12.4(0.4)	3.2(0.1)	0.94(0.01)	0.08(0.01)	0.21(0.01)	4.5(0.7)	0.01(0.01)	2.3(0.1)
G089.36-00.67	3.1(0.4)	11.6(0.5)	12.4(0.6)	1.4(0.1)	0.67(0.01)	0.08(0.01)	0.21(0.01)	3.3(0.4)	0.01(0.01)	1.4(0.3)
G089.62+02.16	3.2(0.5)	10.1(0.1)	10.6(0.1)	3.5(0.2)	0.52(0.01)	0.07(0.01)	0.19(0.01)	2.7(0.3)	0.02(0.01)	...
G091.73+04.36	3.2(0.5)	9.9(0.3)	10.4(0.3)	1.9(0.1)	0.53(0.01)	0.07(0.01)	0.19(0.01)	2.8(0.3)	0.02(0.01)	1.4(0.2)
G092.26+03.80	3.3(0.6)	10.6(0.1)	11.2(0.1)	3.7(0.2)	0.73(0.01)	0.07(0.01)	0.20(0.01)	3.7(0.6)	0.01(0.01)	...
G093.20+09.53	2.9(0.2)	10.0(0.1)	10.5(0.1)	3.2(0.7)	0.30(0.04)	0.07(0.01)	0.19(0.01)	1.6(0.7)	0.06(0.01)	9.7(0.3)
G093.62-04.44	3.1(0.3)	15.6(1.1)	17.8(1.5)	0.8(0.2)	0.52(0.01)	0.09(0.01)	0.25(0.01)	2.1(0.2)	0.03(0.01)	1.2(0.2)
G093.91+10.02	2.8(0.1)	11.3(0.4)	12.0(0.5)	2.6(0.2)	0.47(0.01)	0.08(0.01)	0.20(0.01)	2.3(0.3)	0.03(0.01)	...
G093.99-04.91	2.9(0.2)	10.4(0.4)	11.0(0.5)	2.4(0.1)	0.46(0.01)	0.07(0.01)	0.20(0.01)	2.4(0.2)	0.03(0.01)	2.4(0.1)
G094.08+09.46	3.0(0.3)	9.6(0.3)	10.1(0.3)	3.2(0.1)	0.50(0.01)	0.07(0.01)	0.19(0.01)	2.7(0.3)	0.02(0.01)	8.6(0.7)
G095.75+08.17	3.0(0.1)	17.2(0.4)	20.2(0.7)	0.4(0.2)	0.45(0.01)	0.10(0.01)	0.27(0.01)	1.7(0.1)	0.05(0.01)	...
G096.59+10.29	3.0(0.1)	16.3(0.1)	18.8(0.1)	0.4(0.2)	0.40(0.01)	0.10(0.01)	0.26(0.01)	1.6(0.2)	0.06(0.01)	0.8(0.4)
G097.09+10.12	3.1(0.4)	8.6(0.2)	8.9(0.2)	4.2(0.1)	0.47(0.01)	0.07(0.01)	0.18(0.01)	2.7(0.3)	0.02(0.01)	7.5(0.8)
G098.89+14.01	2.9(0.2)	10.9(0.3)	11.5(0.3)	2.0(0.1)	0.42(0.01)	0.07(0.01)	0.20(0.01)	2.1(0.2)	0.03(0.01)	6.5(0.1)
G102.34+15.96	3.5(0.8)	9.0(0.2)	9.4(0.2)	3.0(0.1)	0.45(0.01)	0.07(0.01)	0.18(0.01)	2.5(0.2)	0.02(0.01)	4.2(0.1)
G103.90+13.97	3.2(0.5)	11.0(0.1)	11.7(0.1)	2.4(0.2)	0.45(0.01)	0.08(0.01)	0.20(0.01)	2.3(0.2)	0.03(0.01)	...
G110.65+09.65	3.3(0.6)	10.8(0.1)	11.4(0.1)	2.5(0.1)	0.55(0.01)	0.07(0.01)	0.20(0.01)	2.8(0.3)	0.02(0.01)	2.1(0.1)
G111.66+20.20	3.3(0.6)	10.4(0.1)	10.9(0.1)	2.1(0.1)	0.49(0.01)	0.07(0.01)	0.19(0.01)	2.6(0.2)	0.02(0.01)	1.3(0.1)
G114.67+14.47	3.6(0.9)	9.3(0.2)	9.6(0.2)	2.7(0.1)	0.66(0.01)	0.07(0.01)	0.18(0.01)	3.7(0.5)	0.01(0.01)	1.6(0.1)
G115.81-03.54	3.2(0.5)	9.9(0.3)	10.4(0.4)	1.3(0.1)	0.38(0.01)	0.07(0.01)	0.19(0.01)	2.0(0.1)	0.03(0.01)	2.7(0.1)
G117.11+12.42	3.3(0.6)	10.3(0.4)	10.9(0.5)	3.0(0.1)	0.47(0.01)	0.07(0.01)	0.19(0.01)	2.4(0.2)	0.02(0.01)	3.8(0.2)
G120.67+02.66	3.1(0.3)	15.4(0.1)	17.5(0.1)	0.9(0.2)	0.51(0.01)	0.09(0.01)	0.25(0.01)	2.1(0.2)	0.03(0.01)	0.6(0.1)
G128.89+13.68	3.1(0.4)	9.4(0.5)	9.8(0.6)	3.1(0.1)	0.47(0.01)	0.07(0.01)	0.19(0.01)	2.6(0.3)	0.02(0.01)	6.0(1.4)
G133.48+09.02a	3.2(0.4)	13.5(0.4)	14.9(0.6)	1.3(0.2)	0.95(0.01)	0.09(0.01)	0.23(0.01)	4.2(1.6)	0.01(0.01)	1.1(0.3)
G158.20-20.28	3.4(0.7)	9.9(0.1)	10.3(0.1)	1.8(0.1)	0.41(0.01)	0.07(0.01)	0.19(0.01)	2.2(0.2)	0.03(0.01)	3.4(2.5)
G158.22-20.14	3.7(1.0)	10.1(0.1)	10.6(0.1)	1.5(0.1)	0.40(0.01)	0.07(0.01)	0.19(0.01)	2.1(0.1)	0.03(0.01)	2.0(0.4)
G158.37-20.72	3.3(0.6)	10.4(0.2)	10.9(0.2)	1.8(0.1)	0.55(0.01)	0.07(0.01)	0.19(0.01)	2.9(0.3)	0.02(0.01)	1.5(0.1)
G158.86-21.60	3.4(0.6)	13.3(0.5)	14.6(0.6)	0.6(0.1)	0.51(0.01)	0.08(0.01)	0.23(0.01)	2.3(0.1)	0.03(0.01)	0.7(0.1)
G159.21-20.44	3.9(1.2)	11.1(0.1)	11.9(0.2)	2.5(0.1)	0.61(0.01)	0.08(0.01)	0.20(0.01)	3.0(0.3)	0.02(0.01)	0.9(0.1)
G160.51-16.84	3.1(0.4)	12.7(0.4)	13.9(0.5)	0.9(0.1)	0.51(0.01)	0.08(0.01)	0.22(0.01)	2.4(0.2)	0.03(0.01)	0.5(0.1)
G164.94-08.57	3.5(0.7)	9.7(0.6)	10.2(0.7)	1.0(0.1)	0.53(0.01)	0.07(0.01)	0.19(0.01)	2.8(0.2)	0.02(0.01)	...
G168.13-16.39	3.4(0.6)	10.5(0.3)	11.1(0.3)	1.1(0.1)	0.36(0.01)	0.07(0.01)	0.20(0.01)	1.9(0.1)	0.04(0.01)	4.1(0.1)
G169.98-04.27	3.2(0.5)	13.0(0.3)	14.3(0.4)	1.1(0.1)	0.45(0.01)	0.08(0.01)	0.22(0.01)	2.1(0.1)	0.03(0.01)	2.6(0.1)
G170.00-16.14	3.1(0.4)	11.6(0.3)	12.5(0.4)	0.8(0.1)	0.35(0.01)	0.08(0.01)	0.21(0.01)	1.7(0.1)	0.05(0.01)	1.7(0.1)
G170.26-16.02	3.4(0.7)	9.1(0.1)	9.4(0.1)	4.0(0.2)	0.44(0.01)	0.07(0.01)	0.18(0.01)	2.4(0.2)	0.02(0.01)	3.1(0.3)
G171.49-14.90	3.8(1.1)	8.9(0.1)	9.2(0.1)	4.4(0.2)	0.44(0.01)	0.07(0.01)	0.18(0.01)	2.5(0.2)	0.02(0.01)	5.7(0.3)
G171.80-15.32	3.4(0.7)	9.2(0.1)	9.5(0.1)	3.0(0.1)	0.41(0.01)	0.07(0.01)	0.18(0.01)	2.3(0.2)	0.03(0.01)	2.8(0.3)
G172.85+02.27	3.1(0.3)	16.1(0.1)	18.5(0.1)	1.6(0.1)	0.94(0.01)	0.09(0.01)	0.25(0.01)	3.7(0.5)	0.01(0.01)	0.9(0.1)
G173.36-16.27	3.2(0.5)	10.1(0.2)	10.6(0.3)	1.8(0.1)	0.41(0.01)	0.07(0.01)	0.19(0.01)	2.2(0.2)	0.03(0.01)	4.2(1.3)
G173.80-15.88	3.7(1.0)	9.4(0.1)	9.8(0.1)	2.5(0.1)	0.41(0.01)	0.07(0.01)	0.18(0.01)	2.3(0.2)	0.03(0.01)	...
G174.08-13.24	3.6(0.9)	9.0(0.1)	9.3(0.1)	3.1(0.1)	0.42(0.01)	0.07(0.01)	0.18(0.01)	2.3(0.2)	0.03(0.01)	...
G174.22-13.43	3.6(0.9)	10.3(0.3)	10.8(0.4)	1.4(0.1)	0.63(0.01)	0.07(0.01)	0.19(0.01)	3.3(0.3)	0.01(0.01)	...
G174.70-15.48	3.4(0.7)	9.6(0.3)	10.1(0.4)	1.5(0.1)	0.45(0.01)	0.07(0.01)	0.19(0.01)	2.5(0.2)	0.02(0.01)	...
G175.49-16.80	3.7(0.9)	9.4(0.1)	9.8(0.1)	2.1(0.1)	0.39(0.01)	0.07(0.01)	0.18(0.01)	2.1(0.2)	0.03(0.01)	3.5(0.3)
G177.97-09.72	3.5(0.8)	9.2(0.1)	9.6(0.2)	4.7(0.2)	0.47(0.01)	0.07(0.01)	0.18(0.01)	2.6(0.3)	0.02(0.01)	6.7(0.2)
G201.44+00.65	3.1(0.4)	11.5(0.4)	12.3(0.4)	1.4(0.1)	0.53(0.01)	0.08(0.01)	0.21(0.01)	2.6(0.3)	0.02(0.01)	1.6(0.1)
G201.59+00.55a	3.3(0.5)	11.3(0.7)	12.0(0.8)	1.0(0.1)	0.72(0.01)	0.08(0.01)	0.20(0.01)	3.5(0.8)	0.01(0.01)	...
G202.30-08.91	3.3(0.5)	11.7(0.6)	12.5(0.7)	0.7(0.1)	0.69(0.01)	0.08(0.01)	0.21(0.01)	3.3(0.3)	0.01(0.01)	0.7(0.1)
G203.20-11.20	3.2(0.5)	10.0(0.4)	10.5(0.4)	1.9(0.1)	0.65(0.01)	0.07(0.01)	0.19(0.01)	3.4(0.4)	0.01(0.01)	1.2(0.1)
G206.10-15.77	3.4(0.7)	10.3(0.1)	10.9(0.1)	2.1(0.1)	0.40(0.01)	0.07(0.01)	0.19(0.01)	2.1(0.2)	0.03(0.01)	1.9(1.6)
G211.48-19.27	3.3(0.5)	12.0(0.4)	13.0(0.5)	1.7(0.1)	0.97(0.01)	0.08(0.01)	0.21(0.01)	4.6(0.8)	0.01(0.01)	...
G212.10-19.15	3.4(0.7)	9.4(0.4)	9.8(0.5)	2.0(0.1)	0.62(0.01)	0.07(0.01)	0.18(0.01)	3.4(0.4)	0.01(0.01)	...
G224.27-00.82	3.4(0.7)	10.7(0.1)	11.4(0.2)	2.7(0.1)	0.86(0.01)	0.07(0.01)	0.20(0.01)	4.3(0.7)	0.01(0.01)	1.4(0.1)
G224.47-00.65	3.4(0.7)	11.7(0.3)	12.6(0.3)	1.3(0.1)	0.73(0.01)	0.08(0.01)	0.21(0.01)	3.5(0.5)	0.01(0.01)	1.2(0.2)
G353.49+15.57	4.1(1.3)	11.9(0.1)	12.8(0.1)	1.3(0.1)	0.47(0.01)	0.08(0.01)	0.21(0.01)	2.3(0.2)	0.03(0.01)	...
G353.54+15.73	4.6(1.8)	11.5(0.3)	12.3(0.3)	1.3(0.1)	0.52(0.01)	0.08(0.01)	0.21(0.01)	2.5(0.2)	0.02(0.01)	...
G354.17+15.32	3.5(0.6)	13.5(0.3)	14.8(0.4)	0.5(0.1)</						

**Table A.4.** Kolmogorov-Smirnov test results for line widths, kinematic temperatures, columnn densities and abundances distributions in different star formation samples.

Distributions	Test Parameter	KS Statistic	P-Value
Planck cold cores and BGPS	$T_{\text{kin}}$	0.44	$3.23 \times 10^{-08}$
Planck cold cores and ATLASGAL	$T_{\text{kin}}$	0.75	$3.65 \times 10^{-34}$
Planck cold cores and UC HII Cand	$T_{\text{kin}}$	0.85	$1.40 \times 10^{-18}$
Planck cold cores and High contrast IRDCs	$T_{\text{kin}}$	0.50	$4.58 \times 10^{-17}$
Planck cold cores and High IR extinction clouds	$T_{\text{kin}}$	0.78	$1.54 \times 10^{-15}$
Planck cold cores and EGOs	$T_{\text{kin}}$	0.67	$9.29 \times 10^{-05}$
Planck cold cores and Ophiuchus	$T_{\text{kin}}$	0.46	$1.34 \times 10^{-02}$
Planck cold cores and Perseus	$T_{\text{kin}}$	0.37	$1.50 \times 10^{-03}$
Planck cold cores and Cepheus & Orion L1630/L1641	$T_{\text{kin}}$	0.60	$2.12 \times 10^{-02}$
Planck cold cores and BGPS	$\Delta V(1,1)$	0.44	$3.23 \times 10^{-08}$
Planck cold cores and ATLASGAL	$\Delta V(1,1)$	0.82	$3.65 \times 10^{-34}$
Planck cold cores and UC HII Cand	$\Delta V(1,1)$	0.74	$1.40 \times 10^{-18}$
Planck cold cores and High contrast IRDCs	$\Delta V(1,1)$	0.72	$4.58 \times 10^{-17}$
Planck cold cores and High IR extinction clouds	$\Delta V(1,1)$	0.67	$1.54 \times 10^{-15}$
Planck cold cores and EGOs	$\Delta V(1,1)$	0.38	$9.29 \times 10^{-05}$
Planck cold cores and Ophiuchus	$\Delta V(1,1)$	0.44	$1.34 \times 10^{-02}$
Planck cold cores and Cepheus & Orion L1630/L1641	$\Delta V(1,1)$	0.29	$2.12 \times 10^{-02}$
Planck cold cores and BGPS	$N_{\text{NH}_3}$	0.89	$3.50 \times 10^{-41}$
Planck cold cores and ATLASGAL	$N_{\text{NH}_3}$	0.97	$3.57 \times 10^{-61}$
Planck cold cores and UC HII Cand	$N_{\text{NH}_3}$	0.93	$1.95 \times 10^{-32}$
Planck cold cores and High contrast IRDCs	$N_{\text{NH}_3}$	0.62	$2.25 \times 10^{-12}$
Planck cold cores and High IR extinction clouds	$N_{\text{NH}_3}$	0.87	$1.62 \times 10^{-28}$
Planck cold cores and EGOs	$N_{\text{NH}_3}$	0.87	$4.34 \times 10^{-27}$
Planck cold cores and Ophiuchus	$N_{\text{NH}_3}$	0.71	$1.18 \times 10^{-06}$
Planck cold cores and Cepheus & Orion L1630/L1641	$N_{\text{NH}_3}$	1.00	$1.04 \times 10^{-29}$
Planck cold cores and BGPS	$N_{\text{H}_2}$	0.89	$3.50 \times 10^{-41}$
Planck cold cores and ATLASGAL	$N_{\text{H}_2}$	0.89	$5.69 \times 10^{-43}$
Planck cold cores and High contrast IRDCs	$N_{\text{H}_2}$	0.52	$1.21 \times 10^{-08}$
Planck cold cores and High IR extinction clouds	$N_{\text{H}_2}$	0.94	$7.25 \times 10^{-35}$
Planck cold cores and Ophiuchus	$N_{\text{H}_2}$	0.73	$8.73 \times 10^{-07}$
Planck cold cores and BGPS	$\chi_{\text{NH}_3}$	0.33	$8.42 \times 10^{-05}$
Planck cold cores and ATLASGAL	$\chi_{\text{NH}_3}$	0.20	$4.41 \times 10^{-02}$
Planck cold cores and High contrast IRDCs	$\chi_{\text{NH}_3}$	0.91	$4.18 \times 10^{-30}$
Planck cold cores and High IR extinction clouds	$\chi_{\text{NH}_3}$	0.77	$8.27 \times 10^{-21}$
Planck cold cores and Ophiuchus	$\chi_{\text{NH}_3}$	0.86	$1.26 \times 10^{-09}$

**Table A.5.** Spearman correlation of kinetic temperature versus non-thermal velocity dispersion in different star formation samples.

Dataset	Spearman Correlation	P-value
ATLASGAL	0.53	$1.48 \times 10^{-53}$
BGPS	0.52	$1.20 \times 10^{-36}$
High contrast IRDCs	0.07	0.45
Ophiuchus	0.49	0.03
Cepheus & Orion L1630/L1641	0.49	$2.01 \times 10^{-4}$
Perseus	0.2	0.16
Planck cold cores	0.33	$4.00 \times 10^{-3}$

## Appendix B: Samples of NH<sub>3</sub> spectra

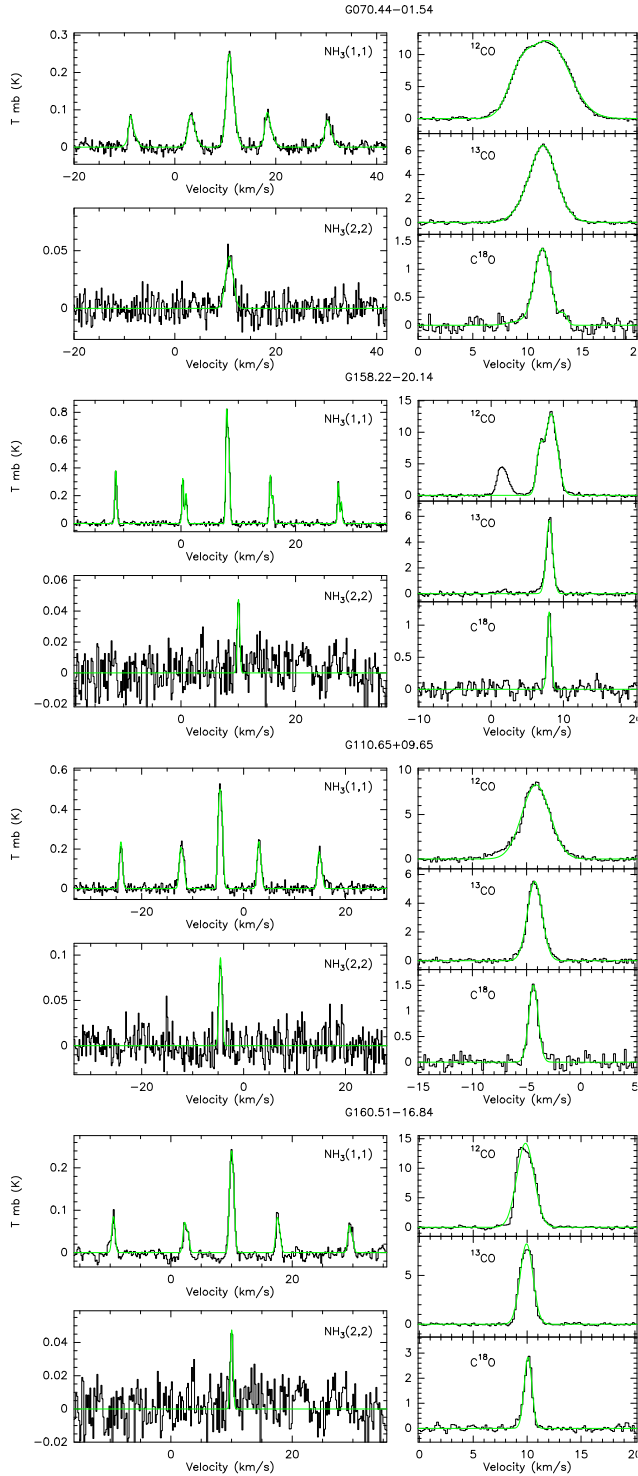


**Fig. B.1.** Examples for typical ammonia spectra in different S/N ratios. Spectra include NH<sub>3</sub>(1,1) and (2,2), <sup>12</sup>CO, <sup>13</sup>CO and C<sup>18</sup>O (1-0) transitions towards cores, namely G070.44-01.54, G110.65+09.65, G158.22-20.14 and G160.51-16.84. The green color indicates the NH<sub>3</sub>(1,1) fitting and Gauss fitting of NH<sub>3</sub>(2,2), <sup>12</sup>CO, <sup>13</sup>CO and C<sup>18</sup>O profile.

## Appendix C: Derived CO parameters

Our calculations assume that the cores are in a state of local thermodynamical equilibrium (LTE) and the <sup>13</sup>CO emission is

optically thin. Adopting a beam-filling factor of unity, the excitation temperature for CO is derived from the following equation (Pineda et al. 2010; Kong et al. 2015)

$$T_{\text{ex(CO)}} = 5.33 \left\{ \ln \left[ 1 + \frac{5.33}{(T_{\text{mb},12\text{CO}} + 0.818)} \right] \right\}^{-1} \text{ K}, \quad (\text{C.1})$$

where  $T_{\text{mb},12\text{CO}}$  is the peak intensity of <sup>12</sup>CO ( $J = 1-0$ ) in units of K. We then obtain the optical depths,  $\tau$ , and the column densities,  $N_{13\text{CO}}$ ,  $N_{\text{C}^{18}\text{O}}$  for the <sup>13</sup>CO and C<sup>18</sup>O molecules using the following equations (Lada et al. 1994; Kawamura et al. 1998).

$$\tau_{13\text{CO}} = -\ln \left\{ 1 - \frac{T_{\text{mb},13\text{CO}}}{5.29([\exp(5.29/T_{\text{ex(CO)})} - 1]^{-1} - 0.164)} \right\}, \quad (\text{C.2})$$

$$\tau_{\text{C}^{18}\text{O}} = -\ln \left\{ 1 - \frac{T_{\text{mb},\text{C}^{18}\text{O}}}{5.27([\exp(5.27/T_{\text{ex(CO)})} - 1]^{-1} - 0.166)} \right\}, \quad (\text{C.3})$$

$$N_{13\text{CO}} = 2.42 \times 10^{14} \frac{\tau_{13\text{CO}} \Delta v_{13\text{CO}} T_{\text{ex(CO)}}}{1 - \exp(-5.29/T_{\text{ex(CO)}})} \text{ cm}^{-2}, \quad (\text{C.4})$$

and

$$N_{\text{C}^{18}\text{O}} = 2.42 \times 10^{14} \frac{\tau_{\text{C}^{18}\text{O}} \Delta v_{\text{C}^{18}\text{O}} T_{\text{ex(CO)}}}{1 - \exp(-5.27/T_{\text{ex(CO)}})} \text{ cm}^{-2}, \quad (\text{C.5})$$

where  $T_{\text{mb},13\text{CO}}$  and  $T_{\text{mb},\text{C}^{18}\text{O}}$  are peak intensities in K, while  $\Delta v_{13\text{CO}}$  and  $\Delta v_{\text{C}^{18}\text{O}}$  are the FWHM linewidths in km s<sup>-1</sup>. In the calculation, the excitation temperatures of <sup>13</sup>CO have been assigned to be equal to those of <sup>12</sup>CO. This would be reasonable when considering the fact that <sup>12</sup>CO, <sup>13</sup>CO, and C<sup>18</sup>O are well coupled in ECCs (Wu et al. 2012). Molecular hydrogen column densities were calculated by the fractional abundances of [H<sub>2</sub>]/[<sup>13</sup>CO] = 89 × 10<sup>4</sup> (McCutcheon et al. 1980) and [H<sub>2</sub>]/[C<sup>18</sup>O] = 7 × 10<sup>6</sup> (Frerking et al. 1982) in the solar neighborhood.

We find that the hydrogen column density ( $N_{\text{H}_2}$ ) values derived from <sup>13</sup>CO and C<sup>18</sup>O are quite close to each other, suggesting that both <sup>13</sup>CO and C<sup>18</sup>O are optically thin and the optical depth effect can be ignored in our calculation (Meng et al. 2013). Therefore we use <sup>13</sup>CO to calculate  $N_{\text{H}_2}$ , as listed in Table C.2 of Appendix C.

The excitation temperatures of CO  $J = 1-0$  ( $T_{\text{ex(CO)}}$ ) for our cores range from 4.4 to 19.7 K. The mean value of  $T_{\text{ex(CO)}}$  is 10.5 K and it is smaller than the value in Wu et al. (2012) and the average dust temperature (13 K) for C3POs (Planck Collaboration et al. 2011a). The H<sub>2</sub> column densities  $N_{\text{H}_2}(\text{<sup>13</sup>CO})$  of our cores are derived from  $N_{13\text{CO}}$  covering the range of (0.07-2.88) × 10<sup>22</sup> cm<sup>-2</sup> with a mean value of 7.4 × 10<sup>21</sup> cm<sup>-2</sup>. Sources in our sample have similar  $N_{\text{H}_2}$  column densities to those in Galactic second quadrant samples, with a mean value of 8 × 10<sup>21</sup> cm<sup>-2</sup> (Meng et al. 2013).

**Table C.1.** Parameters derived from the  $^{12}\text{CO}$ ,  $^{13}\text{CO}$  and  $\text{C}^{18}\text{O}$  (1-0) lines

Name	$V_{\text{LSR}}(\text{CO})$ km s $^{-1}$	$\Delta v_{\text{CO}}$ km s $^{-1}$	$T_{\text{mb},^{12}\text{CO}}$ K	$V_{\text{LSR}}(^{13}\text{CO})$ km s $^{-1}$	$\Delta v_{^{13}\text{CO}}$ km s $^{-1}$	$T_{\text{mb},^{13}\text{CO}}$ K	$V_{\text{LSR}}(\text{C}^{18}\text{O})$ km s $^{-1}$	$\Delta v_{\text{C}^{18}\text{O}}$ km s $^{-1}$	$T_{\text{mb},\text{C}^{18}\text{O}}$ K
G005.03+19.07	3.7(0.1)	1.3(0.1)	14.5(0.2)	3.7(0.1)	1.0(0.1)	8.1(0.1)	3.7(0.1)	0.7(0.1)	1.6(0.2)
G005.29+11.07	4.3(0.1)	0.9(0.1)	16.2(0.3)	4.2(0.1)	0.6(0.1)	7.9(0.1)	4.2(0.1)	0.5(0.1)	1.6(0.1)
G005.80+19.92	2.7(0.1)	0.9(0.1)	6.2(0.3)	2.8(0.1)	0.7(0.1)	6.4(0.1)	2.9(0.1)	0.5(0.1)	1.2(0.1)
G006.08+20.26	4.0(0.1)	1.6(0.1)	10.3(0.2)	3.9(0.1)	1.0(0.1)	8.6(0.1)	3.9(0.1)	0.6(0.1)	2.0(0.2)
G006.32+20.44	4.3(0.1)	1.7(0.1)	10.9(0.2)	4.3(0.1)	0.8(0.1)	8.2(0.2)	4.2(0.1)	0.5(0.1)	3.3(0.1)
G006.41+20.56	4.7(0.1)	1.1(0.1)	12.7(0.3)	4.6(0.2)	0.7(0.2)	7.2(0.2)	4.4(0.1)	0.8(0.1)	2.1(0.1)
G006.70+20.66	3.5(0.1)	1.9(0.1)	11.9(0.2)	3.7(0.1)	1.2(0.1)	7.8(0.1)	3.7(0.1)	0.8(0.1)	2.6(0.1)
G006.98+20.72	3.2(0.1)	1.0(0.1)	11.7(0.3)	3.1(0.1)	0.7(0.1)	6.5(0.1)	3.1(0.1)	0.4(0.1)	1.3(0.1)
G007.53+21.10	3.0(0.1)	1.2(0.1)	16.3(0.2)	3.0(0.1)	0.8(0.1)	8.0(0.1)	3.0(0.1)	0.5(0.1)	1.1(0.1)
G007.80+21.10	3.1(0.1)	0.8(0.1)	8.2(0.2)	3.0(0.1)	0.6(0.1)	6.0(0.2)	3.0(0.1)	0.5(0.1)	0.9(0.1)
G008.52+21.84	3.9(0.1)	1.3(0.1)	10.6(0.4)	3.8(0.1)	0.8(0.1)	7.1(0.2)	3.7(0.1)	0.6(0.1)	2.3(0.2)
G008.67+22.14	3.3(0.1)	1.0(0.1)	11.1(0.3)	3.3(0.1)	0.7(0.1)	7.0(0.1)	3.4(0.1)	0.4(0.1)	2.8(0.1)
G015.16+07.23	2.9(0.1)	1.3(0.1)	8.3(1.2)	2.8(0.1)	1.1(0.1)	3.9(0.2)	2.7(0.1)	0.6(0.1)	0.4(0.1)
G028.45-06.39	12.1(0.1)	1.5(0.1)	8.1(0.2)	11.9(0.1)	1.1(0.1)	5.0(0.1)	12.0(0.1)	0.6(0.1)	2.2(0.1)
G038.36-00.95	17.4(0.1)	3.0(0.1)	6.7(0.3)	16.5(0.1)	1.9(0.1)	4.8(0.1)	16.4(0.1)	1.5(0.1)	1.3(0.1)
G049.76-07.25	21.1(0.1)	1.2(0.1)	5.1(0.2)	21.5(0.1)	1.1(0.1)	3.2(0.1)			
G057.10+03.65	11.5(0.1)	1.6(0.1)	7.6(0.2)	11.6(0.1)	1.4(0.1)	5.1(0.1)	11.5(0.1)	1.1(0.1)	1.4(0.1)
G065.43-03.15	6.1(0.1)	2.6(0.1)	2.4(0.2)	6.0(0.1)	1.2(0.1)	2.4(0.1)	6.1(0.1)	0.6(0.1)	0.9(0.1)
G070.44-01.54	10.8(0.2)	3.4(0.2)	6.8(0.2)	11.3(0.1)	3.3(0.3)	3.0(0.1)	11.4(0.1)	1.7(0.1)	1.4(0.1)
G070.72-00.63	11.2(0.1)	3.8(0.1)	8.9(0.5)	11.7(0.1)	3.1(0.2)	3.9(0.4)			
G074.11+00.11a	2.7(0.2)	10.3(0.2)	1.5(0.2)	-0.1(0.1)	2.2(0.1)	2.9(0.1)	-1.5(0.1)	2.1(0.1)	1.1(0.1)
G074.11+00.11b	1.9(0.2)	4.0(0.2)	5.8(0.2)	2.1(0.1)	2.8(0.1)	2.3(0.1)			
G084.79-01.11	1.0(0.2)	2.9(0.2)	7.9(0.3)	0.8(0.1)	1.8(0.1)	5.5(0.1)	0.8(0.1)	1.3(0.1)	1.5(0.1)
G089.36-00.67	2.5(0.1)	4.6(0.1)	7.2(0.6)	2.6(0.1)	2.5(0.1)	3.7(0.1)	2.7(0.1)	1.4(0.1)	0.8(0.1)
G089.64-06.59	12.5(0.1)	1.2(0.1)	5.2(0.1)	12.6(0.1)	0.9(0.1)	1.9(0.1)	12.5(0.2)	0.8(0.3)	0.4(0.1)
G089.75-02.16	1.4(0.2)	1.4(0.2)	8.5(0.2)	1.5(0.1)	0.9(0.1)	3.3(0.1)	1.6(0.1)	0.9(0.2)	0.6(0.1)
G089.93-01.94	1.6(0.1)	1.6(0.1)	11.4(0.5)	1.4(0.1)	1.2(0.1)	6.1(0.1)	1.4(0.1)	1.0(0.1)	0.9(0.1)
G091.73+04.36	-5.3(0.1)	2.4(0.1)	4.9(0.3)	-4.2(0.1)	2.0(0.1)	4.2(0.1)	-4.3(0.1)	1.1(0.1)	1.9(0.1)
G093.20+09.53	-1.8(0.1)	2.2(0.2)	3.1(0.3)	-1.9(0.1)	1.0(0.1)	2.4(0.1)	-1.8(0.1)	0.7(0.1)	0.7(0.1)
G093.22-04.59	3.5(0.2)	2.1(0.2)	4.4(0.2)	3.6(0.2)	1.3(0.2)	2.4(0.1)	3.6(0.1)	0.8(0.2)	0.5(0.1)
G093.62-04.44	4.5(0.1)	1.7(0.1)	5.5(0.2)	3.9(0.1)	1.3(0.1)	3.8(0.1)	3.7(0.1)	1.0(0.1)	1.6(0.2)
G093.91+10.02	-2.2(0.1)	1.2(0.1)	2.7(0.3)	-1.9(0.1)	0.8(0.1)	3.9(0.1)	-1.9(0.1)	0.6(0.1)	1.4(0.1)
G093.99-04.91	4.7(0.1)	2.4(0.1)	5.1(0.2)	4.9(0.1)	1.1(0.1)	4.6(0.2)	4.9(0.1)	0.7(0.1)	1.2(0.1)
G094.08+09.46	0.6(0.1)	2.2(0.1)	5.5(0.3)	0.2(0.1)	1.6(0.1)	2.4(0.1)	0.1(0.1)	1.1(0.2)	0.5(0.1)
G095.11+06.50	-2.7(0.1)	1.0(0.1)	4.5(0.2)	-2.4(0.2)	1.2(0.2)	2.2(0.1)	-2.3(0.1)	0.6(0.1)	1.2(0.1)
G095.51+09.97	-2.3(0.1)	2.1(0.2)	5.6(1.2)	-2.4(0.1)	1.2(0.1)	2.0(0.2)	-2.4(0.1)	0.6(0.1)	1.0(0.1)
G096.59+10.29	-2.8(0.1)	1.6(0.1)	5.0(0.2)	-2.6(0.1)	0.7(0.1)	4.2(0.1)	-2.6(0.1)	0.4(0.1)	1.5(0.1)
G096.94+10.25	-2.9(0.1)	1.6(0.1)	7.3(0.1)	-2.4(0.1)	1.3(0.1)	3.8(0.1)	-2.4(0.1)	0.8(0.1)	1.4(0.1)
G097.09+10.12	-2.7(0.2)	1.1(0.2)	3.9(0.2)	-2.8(0.1)	1.1(0.1)	3.2(0.1)	-2.8(0.1)	0.6(0.1)	1.6(0.1)
G097.20+09.87	-2.6(0.1)	2.0(0.1)	4.4(0.2)	-2.5(0.1)	1.1(0.1)	4.0(0.1)	-2.5(0.1)	0.8(0.1)	1.7(0.1)
G097.38+09.95	-2.1(0.1)	1.8(0.1)	3.9(0.1)	-2.2(0.1)	1.0(0.1)	2.7(0.1)	-2.3(0.1)	0.8(0.1)	0.6(0.1)
G098.52+13.88	-3.6(0.1)	0.7(0.1)	2.4(0.3)	-3.1(0.1)	0.9(0.1)	3.1(0.1)	-3.1(0.1)	0.6(0.2)	0.5(0.1)
G098.89+14.01	-2.8(0.1)	1.0(0.1)	5.8(0.2)	-2.9(0.1)	0.7(0.1)	3.6(0.1)	-2.9(0.1)	0.7(0.1)	0.6(0.1)
G098.96+13.68	-2.8(0.1)	1.9(0.1)	6.2(0.3)	-2.8(0.1)	1.1(0.1)	3.3(0.1)	-2.8(0.1)	0.5(0.1)	0.7(0.1)
G102.34+15.96	2.3(0.1)	1.0(0.1)	6.1(0.1)	2.7(0.1)	1.0(0.1)	4.9(0.1)	2.6(0.1)	0.7(0.1)	1.0(0.1)
G102.70+15.19	2.5(0.1)	1.5(0.1)	6.6(0.2)	2.0(0.1)	0.9(0.1)	3.9(0.2)	2.0(0.1)	0.6(0.1)	1.4(0.2)
G102.72+15.36	1.0(0.1)	1.9(0.1)	6.3(0.2)	1.2(0.1)	1.0(0.1)	3.4(0.1)	1.3(0.1)	0.6(0.1)	1.2(0.2)
G103.90+13.97	2.4(0.1)	0.6(0.1)	2.3(0.2)	2.9(0.1)	1.3(0.1)	4.8(0.1)	2.9(0.1)	0.6(0.1)	1.3(0.1)
G108.10+13.19	-5.4(0.1)	0.9(0.1)	5.4(0.6)	-5.2(0.1)	1.0(0.1)	3.7(0.1)	-5.4(0.1)	0.5(0.1)	1.5(0.1)
G110.41+11.52	-4.9(0.1)	1.4(0.1)	4.9(0.1)	-4.8(0.1)	1.0(0.1)	3.3(0.1)	-4.8(0.1)	0.5(0.1)	2.2(0.1)
G110.52+19.17	-9.5(0.1)	0.6(0.1)	3.9(0.2)	-9.2(0.1)	0.5(0.1)	2.9(0.1)	-9.3(0.1)	0.4(0.1)	1.7(0.1)
G110.65+09.65	-4.1(0.1)	3.1(0.1)	8.3(0.2)	-4.2(0.1)	1.6(0.1)	5.5(0.1)	-4.4(0.1)	1.0(0.1)	1.5(0.1)
G111.66+20.20	-7.6(0.1)	1.6(0.1)	6.0(0.3)	-7.9(0.1)	1.3(0.1)	5.6(0.2)	-8.0(0.1)	0.9(0.1)	1.4(0.1)
G111.68+19.74	-9.1(0.1)	0.7(0.1)	3.6(0.2)	-8.8(0.1)	0.7(0.1)	1.8(0.1)	-9.0(0.1)	0.5(0.1)	1.1(0.1)
G111.77+20.26	-8.6(0.1)	0.9(0.1)	5.9(0.2)	-8.3(0.1)	0.9(0.1)	3.6(0.1)	-8.1(0.1)	0.8(0.1)	1.1(0.1)
G112.25+13.82	-3.9(0.1)	1.0(0.1)	4.9(0.1)	-4.0(0.1)	0.8(0.1)	4.0(0.1)	-4.0(0.1)	0.9(0.1)	2.1(0.1)
G114.16+14.80	-4.6(0.1)	1.2(0.1)	6.6(0.3)	-4.1(0.1)	1.5(0.1)	3.6(0.1)	-4.2(0.1)	0.7(0.1)	1.6(0.1)
G114.56+14.72	-3.8(0.1)	1.3(0.1)	5.0(0.3)	-4.5(0.1)	0.8(0.1)	3.2(0.1)	-4.7(0.1)	0.8(0.1)	1.8(0.1)
G114.67+14.47	-3.9(0.1)	1.6(0.1)	7.1(0.2)	-4.2(0.1)	1.6(0.1)	6.1(0.1)	-4.2(0.1)	1.2(0.1)	1.8(0.1)
G115.81-03.54	-0.5(0.1)	1.1(0.1)	5.6(0.2)	-0.7(0.1)	1.0(0.1)	3.9(0.1)	-0.9(0.1)	0.7(0.1)	1.0(0.1)
G116.08-02.38	-0.8(0.2)	1.6(0.2)	7.0(0.2)	-0.8(0.1)	1.2(0.1)	3.4(0.1)	-1.0(0.1)	1.6(0.1)	0.7(0.1)

**Table C.1.** Continued

Name	$V_{\text{LSR}}(\text{CO})$ km s $^{-1}$	$\Delta v_{\text{CO}}$ km s $^{-1}$	$T_{\text{mb},^{12}\text{CO}}$ K	$V_{\text{LSR}}(^{13}\text{CO})$ km s $^{-1}$	$\Delta v_{^{13}\text{CO}}$ km s $^{-1}$	$T_{\text{mb},^{13}\text{CO}}$ K	$V_{\text{LSR}}(\text{C}^{18}\text{O})$ km s $^{-1}$	$\Delta v_{\text{C}^{18}\text{O}}$ km s $^{-1}$	$T_{\text{mb},\text{C}^{18}\text{O}}$ K
G117.11+12.42	3.6(0.1)	0.8(0.1)	7.5(0.2)	3.9(0.1)	1.0(0.1)	5.5(0.1)	3.9(0.1)	0.6(0.1)	2.0(0.1)
G120.16+03.09	-19.1(0.1)	2.4(0.1)	7.3(0.2)	-18.9(0.2)	1.3(0.2)	4.0(0.1)	-19.3(0.1)	1.3(0.1)	0.8(0.1)
G120.67+02.66	-18.0(0.1)	3.4(0.1)	13.0(0.6)	-18.0(0.1)	2.2(0.1)	5.3(0.1)	-18.1(0.1)	1.8(0.1)	0.7(0.1)
G120.98+02.66	-16.9(0.1)	2.7(0.1)	9.0(0.6)	-16.9(0.1)	1.7(0.1)	3.8(0.1)	-17.1(0.1)	1.5(0.2)	0.5(0.1)
G121.35+03.39	-6.1(0.1)	2.3(0.1)	4.8(0.4)	-5.5(0.1)	1.5(0.1)	3.5(0.1)	-5.4(0.1)	0.9(0.1)	1.2(0.1)
G123.66+24.89	-4.2(0.2)	1.0(0.2)	5.5(0.2)	-4.3(0.1)	1.1(0.1)	3.4(0.1)	-4.3(0.1)	0.7(0.1)	0.6(0.1)
G127.85+14.16	3.0(0.1)	1.2(0.1)	4.4(0.2)	2.9(0.1)	0.9(0.1)	5.1(0.1)	2.9(0.1)	0.6(0.1)	2.0(0.1)
G127.88+02.66	-11.3(0.1)	1.4(0.1)	8.9(0.2)	-11.3(0.1)	1.4(0.1)	6.0(0.1)	-11.4(0.1)	0.9(0.1)	1.0(0.1)
G128.89+13.68	3.8(0.1)	1.0(0.1)	6.6(0.6)	3.9(0.1)	0.8(0.1)	4.7(0.1)	3.9(0.1)	0.5(0.1)	0.7(0.1)
G128.95-00.18	-14.6(0.1)	1.7(0.1)	8.5(0.5)	-14.6(0.1)	1.0(0.1)	4.8(0.1)	-14.6(0.1)	0.9(0.1)	0.9(0.1)
G132.29+09.36	-12.8(0.2)	2.0(0.2)	4.2(0.1)	-12.2(0.1)	1.6(0.1)	2.9(0.1)	-12.1(0.1)	0.6(0.2)	0.7(0.1)
G133.28+08.81	-10.1(0.2)	2.0(0.2)	5.7(0.2)	-10.6(0.2)	1.4(0.2)	4.0(0.1)	-10.7(0.1)	1.3(0.1)	0.8(0.1)
G133.48+09.02a	-17.1(0.2)	2.7(0.2)	10.0(1.5)	-16.9(0.2)	2.0(0.3)	5.1(0.5)	-16.8(0.2)	1.4(0.2)	1.2(0.1)
G133.48+09.02b	-14.2(0.2)	3.5(0.2)	5.8(1.5)	-15.1(0.3)	2.2(0.4)	3.9(0.5)	-15.2(0.2)	1.5(0.2)	1.0(0.1)
G140.97+05.73	-11.6(0.1)	1.4(0.1)	6.3(0.2)	-11.6(0.1)	1.4(0.1)	5.1(0.1)	-11.7(0.1)	0.8(0.1)	1.5(0.1)
G144.66+00.16	-7.6(0.1)	1.5(0.1)	7.4(0.3)	-7.8(0.1)	1.0(0.1)	4.6(0.3)			
G147.01+03.39	-4.5(0.1)	0.9(0.1)	5.0(0.4)	-4.7(0.1)	0.7(0.1)	3.6(0.1)	-4.7(0.1)	0.7(0.1)	0.5(0.1)
G149.23+03.07	3.1(0.1)	1.3(0.1)	5.1(1.1)	3.0(0.1)	0.8(0.1)	3.4(0.1)	3.1(0.1)	0.5(0.1)	0.5(0.1)
G149.41+03.37	3.2(0.1)	1.1(0.1)	5.8(0.4)	3.3(0.1)	1.1(0.1)	3.4(0.1)	3.2(0.1)	0.7(0.2)	0.5(0.1)
G149.52-01.23	-8.2(0.1)	3.3(0.1)	12.0(0.2)	-7.3(0.1)	1.1(0.1)	2.8(0.1)	-7.5(0.1)	1.1(0.1)	0.8(0.1)
G150.22+03.91	3.5(0.1)	2.0(0.1)	6.6(0.4)	3.3(0.1)	1.2(0.1)	4.6(0.1)	3.5(0.1)	0.3(0.1)	0.7(0.1)
G150.44+03.95	3.2(0.1)	2.1(0.1)	7.8(1.1)	3.2(0.1)	1.1(0.1)	5.1(0.1)	3.3(0.1)	0.6(0.1)	1.2(0.1)
G151.08+04.46	3.3(0.1)	1.3(0.1)	7.5(0.7)	3.2(0.1)	0.7(0.1)	5.7(0.1)	3.1(0.1)	0.4(0.1)	1.6(0.1)
G151.45+03.95	1.8(0.2)	1.1(0.2)	4.5(0.2)	1.3(0.2)	1.5(0.2)	3.4(0.1)	1.6(0.1)	1.0(0.3)	0.7(0.1)
G154.07+05.09	4.2(0.1)	2.4(0.1)	7.0(0.2)	4.3(0.1)	1.7(0.1)	4.0(0.1)	4.8(0.1)	0.4(0.1)	0.6(0.1)
G154.07+05.21	4.3(0.1)	1.4(0.1)	5.8(0.2)	4.6(0.1)	0.8(0.1)	1.6(0.1)	4.5(0.1)	0.6(0.1)	0.5(0.1)
G154.68-15.34	2.9(0.1)	2.1(0.1)	4.2(0.2)	3.2(0.1)	1.2(0.1)	3.1(0.1)	3.3(0.1)	0.6(0.1)	0.8(0.1)
G154.90+04.61a	3.0(0.1)	1.3(0.1)	6.3(0.2)	3.3(0.1)	1.2(0.1)	2.3(0.1)	3.4(0.1)	0.9(0.1)	0.3(0.1)
G154.90+04.61b	4.6(0.1)	2.0(0.1)	8.5(0.2)	4.1(0.1)	1.5(0.1)	2.9(0.1)	4.5(0.1)	0.3(0.1)	0.3(0.1)
G155.45-14.59	2.9(0.1)	1.4(0.1)	2.9(0.1)	2.1(0.1)	1.0(0.1)	3.6(0.1)	2.1(0.1)	0.7(0.1)	1.5(0.1)
G155.67+05.11	4.6(0.1)	1.6(0.1)	8.1(0.4)	4.5(0.1)	1.3(0.1)	3.9(0.2)	4.6(0.1)	0.6(0.1)	0.6(0.1)
G156.20+05.26	5.5(0.1)	1.0(0.1)	8.1(0.3)	5.3(0.1)	0.7(0.1)	5.6(0.1)	5.3(0.1)	0.5(0.1)	0.8(0.1)
G156.90-08.49	-7.4(0.1)	2.1(0.1)	4.4(0.1)	-7.9(0.1)	2.2(0.1)	2.8(0.1)	-7.8(0.1)	0.7(0.1)	1.7(0.1)
G157.10-08.70	-6.9(0.1)	1.5(0.1)	5.8(0.2)	-7.3(0.1)	1.1(0.1)	3.8(0.1)	-7.5(0.1)	0.8(0.1)	1.6(0.1)
G157.12-11.56	-2.0(0.1)	2.0(0.1)	10.0(0.7)	-1.7(0.1)	1.3(0.1)	4.7(0.1)	-1.6(0.1)	0.9(0.1)	0.7(0.1)
G157.25-01.00	5.1(0.1)	1.0(0.1)	7.6(0.9)	5.2(0.1)	0.7(0.1)	7.1(0.2)	5.3(0.1)	0.5(0.1)	2.6(0.1)
G157.60-12.17	-8.1(0.1)	2.6(0.1)	6.6(0.2)	-7.8(0.1)	1.2(0.2)	3.8(1.0)	-7.8(0.1)	0.9(0.1)	0.9(0.1)
G158.20-20.28	7.2(0.4)	2.3(1.3)	11.2(2.6)	7.5(0.2)	0.9(0.2)	5.1(0.2)	7.5(0.1)	0.8(0.1)	1.0(0.1)
G158.22-20.14	8.3(0.1)	2.0(0.2)	12.9(1.1)	8.1(0.1)	1.1(0.1)	5.6(0.1)	8.0(0.1)	0.7(0.1)	1.2(0.1)
G158.24-21.80	4.1(0.1)	2.1(0.1)	6.6(0.1)	4.0(0.1)	1.8(0.1)	3.0(0.1)	3.9(0.2)	1.0(0.2)	0.6(0.1)
G158.37-20.72	6.9(0.1)	2.8(0.1)	12.9(0.4)	7.1(0.1)	1.6(0.1)	5.9(0.1)	7.1(0.2)	1.9(0.2)	0.6(0.1)
G158.77-33.30	-2.5(0.1)	2.3(0.1)	5.7(0.1)	-2.2(0.1)	1.1(0.1)	3.1(0.2)	-2.5(0.1)	0.9(0.2)	0.6(0.1)
G158.86-21.60	5.4(0.1)	3.1(0.1)	10.7(0.4)	5.2(0.1)	1.6(0.1)	4.5(0.2)	5.2(0.1)	1.2(0.2)	0.7(0.2)
G159.01-08.46	-3.9(0.1)	2.5(0.1)	4.2(0.2)	-4.7(0.1)	2.1(0.1)	3.2(0.1)	-4.4(0.1)	1.1(0.1)	1.0(0.1)
G159.21-20.44	6.6(0.2)	1.5(0.2)	10.2(0.2)	6.8(0.2)	1.8(0.2)	8.5(0.1)	6.7(0.1)	1.2(0.1)	4.0(0.1)
G159.34+11.20	2.7(0.1)	1.0(0.1)	9.2(0.3)	2.4(0.1)	0.7(0.1)	4.6(0.1)	2.4(0.1)	0.4(0.1)	0.8(0.1)
G159.65-19.68	2.0(0.1)	0.7(0.1)	7.4(0.1)	2.0(0.1)	0.5(0.1)	1.8(0.1)	2.2(0.1)	0.4(0.2)	0.5(0.1)
G159.65+11.39	7.2(0.1)	2.4(0.1)	14.7(0.2)	7.3(0.1)	1.6(0.1)	7.1(0.4)	7.3(0.1)	0.9(0.1)	1.4(0.1)
G159.67-34.31	-1.8(0.1)	1.0(0.1)	5.7(0.1)	-1.5(0.1)	0.8(0.1)	3.4(0.1)	-1.6(0.1)	0.4(0.1)	0.4(0.1)
G159.76-19.62	8.1(0.1)	2.1(0.1)	9.3(0.3)	7.6(0.1)	1.6(0.2)	6.1(0.5)	7.8(0.1)	0.7(0.1)	1.4(0.2)
G160.51-16.84	9.8(0.1)	1.9(0.1)	14.2(0.2)	9.9(0.1)	1.4(0.1)	8.2(0.1)	10.1(0.1)	0.9(0.1)	2.8(0.1)
G160.53-19.72	-3.7(0.1)	1.3(0.1)	7.2(0.1)	-3.6(0.1)	0.9(0.1)	3.4(0.1)	-3.7(0.1)	1.1(0.3)	0.4(0.1)
G160.53-09.84	3.2(0.1)	2.1(0.1)	10.8(0.2)	3.4(0.1)	1.7(0.1)	5.5(0.1)	3.6(0.1)	0.9(0.1)	1.6(0.1)
G161.21-08.72	-2.7(0.2)	2.0(0.2)	5.1(0.2)	-3.9(0.1)	1.5(0.1)	3.9(0.1)	-3.8(0.1)	0.9(0.1)	0.9(0.1)
G161.43-35.59	-5.9(0.1)	0.8(0.1)	8.3(0.2)	-5.9(0.1)	0.6(0.1)	5.0(0.1)	-5.9(0.1)	0.5(0.1)	0.8(0.1)
G161.60-08.34	-3.7(0.1)	0.8(0.2)	2.8(0.6)	-3.5(0.3)	0.9(0.5)	1.8(0.6)	-3.0(0.1)	1.5(0.2)	1.8(0.4)
G161.85-35.75	-6.6(0.1)	0.8(0.1)	6.4(0.3)	-6.6(0.1)	0.6(0.1)	4.3(0.2)			
G162.46-08.70	0.0(0.1)	1.1(0.1)	1.7(0.1)	-0.8(0.1)	1.1(0.1)	3.2(0.1)	-1.2(0.1)	1.0(0.1)	2.0(0.1)
G163.32-08.42	-2.1(0.1)	3.1(0.1)	2.8(0.1)	-2.2(0.1)	0.6(0.1)	1.2(0.1)	-1.8(0.1)	0.9(0.1)	1.5(0.1)
G165.16-07.55	-1.3(0.1)	2.4(0.1)	4.9(0.2)	-0.8(0.1)	0.9(0.1)	3.0(0.1)	-0.8(0.1)	0.7(0.1)	0.8(0.1)
G165.34-07.51a	-1.2(0.2)	1.3(0.2)	5.7(0.1)	-1.4(0.1)	1.3(0.1)	3.7(0.3)	-1.6(0.1)	0.6(0.1)	0.4(0.1)

**Table C.1.** Continued

Name	$V_{\text{LSR}}(\text{CO})$ km s $^{-1}$	$\Delta v_{\text{CO}}$ km s $^{-1}$	$T_{\text{mb},^{12}\text{CO}}$ K	$V_{\text{LSR}}(^{13}\text{CO})$ km s $^{-1}$	$\Delta v_{^{13}\text{CO}}$ km s $^{-1}$	$T_{\text{mb},^{13}\text{CO}}$ K	$V_{\text{LSR}}(\text{C}^{18}\text{O})$ km s $^{-1}$	$\Delta v_{\text{C}^{18}\text{O}}$ km s $^{-1}$	$T_{\text{mb},\text{C}^{18}\text{O}}$ K
G165.34-07.51b	0.0(0.2)	1.6(0.2)	4.4(0.1)	-0.2(0.1)	1.0(0.1)	2.7(0.3)	-0.5(0.1)	1.0(0.1)	0.9(0.1)
G165.69-09.14	-0.4(0.1)	2.8(0.2)	4.7(0.6)	-0.6(0.1)	1.5(0.1)	4.0(0.3)	-0.8(0.1)	0.6(0.1)	1.2(0.3)
G168.00-15.69	7.7(0.1)	1.0(0.1)	10.7(0.6)	7.7(0.2)	0.8(0.2)	4.7(0.1)	7.7(0.1)	0.6(0.1)	2.5(0.1)
G168.13-16.39	5.9(0.2)	0.9(0.2)	7.6(0.2)	6.1(0.1)	0.6(0.1)	4.0(0.1)	6.5(0.1)	0.8(0.1)	2.7(0.1)
G168.72-15.48	7.1(0.2)	1.3(0.2)	9.1(0.4)	7.2(0.1)	1.4(0.1)	6.4(0.3)	7.3(0.1)	0.6(0.1)	2.7(0.2)
G169.76-16.15a	5.5(0.1)	1.2(0.1)	7.1(0.2)	5.5(0.1)	1.0(0.1)	4.7(0.1)	5.5(0.1)	0.5(0.1)	2.1(0.1)
G169.76-16.15b	7.4(0.1)	1.5(0.1)	9.5(0.2)	6.5(0.1)	0.8(0.1)	1.6(0.1)	6.9(0.1)	0.6(0.1)	1.6(0.1)
G169.84-07.61	6.4(0.1)	1.3(0.1)	7.2(0.1)	6.4(0.1)	0.7(0.1)	4.4(0.1)	6.4(0.1)	0.4(0.1)	1.9(0.1)
G169.98-04.27	7.9(0.1)	1.0(0.1)	6.6(0.2)	8.1(0.1)	0.7(0.1)	4.6(0.1)	8.0(0.1)	0.5(0.1)	1.2(0.1)
G170.00-16.14	7.4(0.1)	1.0(0.1)	4.5(0.3)	6.8(0.1)	0.8(0.1)	3.6(0.2)	6.8(0.2)	1.0(0.4)	0.7(0.2)
G170.13-16.06	7.4(0.1)	0.9(0.1)	3.8(0.2)	6.9(0.2)	1.0(0.2)	4.7(0.1)	7.0(0.1)	0.6(0.1)	1.4(0.1)
G170.26-16.02	5.9(0.1)	1.2(0.1)	6.5(0.3)	6.5(0.1)	1.2(0.1)	5.6(0.1)	6.5(0.1)	0.8(0.1)	1.6(0.1)
G170.81-18.34	7.6(0.1)	1.4(0.1)	8.3(0.3)	7.9(0.1)	0.8(0.1)	6.3(0.2)	7.9(0.1)	0.5(0.1)	2.4(0.2)
G170.88-10.92	6.2(0.1)	1.3(0.4)	5.3(2.0)	6.1(0.1)	0.7(0.1)	4.7(0.2)	6.0(0.1)	0.5(0.1)	1.4(0.1)
G170.99-15.81	6.6(0.1)	1.6(0.3)	4.2(0.5)	6.5(0.1)	1.1(0.1)	5.5(0.3)	6.4(0.1)	0.6(0.1)	3.0(0.3)
G171.14-17.58	7.2(0.1)	1.0(0.2)	7.1(0.9)	7.4(0.1)	0.9(0.1)	4.3(0.3)	7.4(0.1)	0.4(0.1)	2.1(0.2)
G171.34+02.59	-20.0(0.1)	2.1(0.1)	7.7(0.3)	-19.2(0.2)	2.1(0.2)	3.2(0.1)	-19.3(0.1)	1.3(0.1)	0.6(0.1)
G171.49-14.90	6.0(0.1)	1.6(0.1)	6.9(0.3)	6.5(0.1)	0.9(0.1)	5.4(0.2)	6.4(0.1)	0.4(0.1)	2.6(0.2)
G171.51-10.59	6.2(0.1)	2.4(0.1)	3.8(0.2)	6.1(0.1)	0.6(0.1)	4.9(0.2)	6.1(0.1)	0.4(0.1)	1.8(0.1)
G171.80-15.32	6.8(0.1)	1.7(0.1)	7.5(0.4)	6.9(0.1)	0.9(0.1)	6.4(0.2)	6.8(0.1)	1.0(0.1)	1.2(0.2)
G171.84-05.22	7.1(0.1)	0.9(0.1)	8.4(0.3)	7.0(0.1)	0.6(0.1)	6.0(0.2)	6.9(0.1)	0.4(0.1)	1.5(0.2)
G172.06-15.21	6.6(0.1)	1.5(0.1)	6.1(0.2)	6.7(0.1)	0.8(0.1)	5.5(0.1)	6.9(0.1)	0.7(0.1)	1.8(0.1)
G172.13-16.93	6.9(0.2)	1.2(0.2)	8.7(0.1)	7.0(0.1)	0.9(0.1)	5.7(0.1)	7.1(0.1)	0.6(0.1)	2.4(0.1)
G172.85+02.27	-15.6(0.1)	3.8(0.1)	8.7(0.2)	-17.2(0.1)	3.3(0.1)	4.7(0.1)	-17.3(0.1)	2.0(0.1)	0.8(0.1)
G172.92-16.74	5.0(0.2)	1.1(0.2)	7.3(0.1)	5.0(0.1)	0.8(0.1)	5.9(0.1)	5.0(0.1)	0.7(0.1)	0.9(0.1)
G172.94-05.49	7.0(0.1)	0.8(0.1)	10.7(0.6)	7.0(0.1)	0.6(0.1)	6.4(0.1)	7.0(0.1)	0.4(0.1)	2.6(0.1)
G173.07-16.52	6.6(0.1)	1.3(0.1)	10.9(0.3)	6.7(0.1)	0.9(0.1)	6.5(0.2)	6.8(0.1)	0.7(0.1)	2.0(0.2)
G173.12-13.32	5.0(0.1)	0.6(0.3)	4.1(0.4)	5.2(0.1)	0.7(0.1)	4.5(0.3)	5.2(0.1)	0.5(0.1)	2.4(0.3)
G173.36-16.27	6.1(0.1)	1.0(0.2)	6.8(0.6)	6.2(0.1)	1.0(0.2)	3.9(0.5)			
G173.45-13.34	5.4(0.1)	1.3(0.1)	7.0(0.2)	5.4(0.1)	0.8(0.1)	4.3(0.1)	5.3(0.1)	0.4(0.1)	2.4(0.2)
G173.89-17.64	5.0(0.1)	1.3(0.1)	7.4(0.4)	5.2(0.1)	0.9(0.1)	5.0(0.3)	5.2(0.1)	0.5(0.1)	1.8(0.2)
G173.95-13.74	6.8(0.1)	1.6(0.1)	6.7(0.3)	6.7(0.1)	0.9(0.1)	6.2(0.2)	6.5(0.1)	0.6(0.1)	3.5(0.2)
G174.06-15.81	6.1(0.1)	2.6(0.1)	9.9(0.2)	6.3(0.1)	1.2(0.1)	7.5(0.1)	6.3(0.1)	0.7(0.1)	2.8(0.1)
G174.39-13.43	5.7(0.2)	1.0(0.2)	6.6(0.2)	5.3(0.1)	0.9(0.1)	4.6(0.1)	5.8(0.1)	0.9(0.1)	2.4(0.1)
G174.44-15.75	6.9(0.1)	1.8(0.1)	10.1(0.3)	6.8(0.1)	1.1(0.1)	6.2(0.2)	6.8(0.1)	0.5(0.1)	1.3(0.2)
G174.81-15.15	6.3(0.1)	0.9(0.1)	3.7(0.1)	5.8(0.1)	0.7(0.1)	4.7(0.1)	5.7(0.1)	0.4(0.1)	0.9(0.1)
G175.49-16.80	6.1(0.1)	1.7(0.1)	6.2(0.3)	5.6(0.1)	0.8(0.1)	4.9(0.2)	5.5(0.1)	0.4(0.1)	2.2(0.2)
G177.14-01.21	-17.1(0.1)	3.7(0.1)	8.4(0.2)	-17.2(0.1)	2.2(0.1)	4.5(0.1)	-17.1(0.1)	1.6(0.1)	1.0(0.1)
G177.86+01.04	-17.8(0.2)	2.5(0.2)	5.8(0.2)	-18.1(0.1)	1.8(0.2)	2.1(0.1)			
G177.89-20.16	7.2(0.1)	1.1(0.1)	8.2(1.5)	7.1(0.1)	0.8(0.1)	5.7(0.4)	7.0(0.1)	0.4(0.1)	1.4(0.1)
G177.97-09.72	7.1(0.1)	1.0(0.1)	11.2(0.3)	7.1(0.1)	0.7(0.1)	7.0(0.1)	7.1(0.1)	0.5(0.1)	3.1(0.1)
G178.28-00.61	-1.0(0.1)	2.1(0.1)	7.3(0.2)	-0.9(0.1)	1.5(0.1)	3.9(0.1)	-1.0(0.1)	1.2(0.2)	0.6(0.1)
G178.98-06.74	7.5(0.1)	0.8(0.1)	7.9(0.2)	7.7(0.1)	0.8(0.1)	6.4(0.1)	7.7(0.1)	0.4(0.1)	2.8(0.1)
G180.81-19.66	8.8(0.1)	1.0(0.1)	8.6(0.5)	8.9(0.1)	0.7(0.1)	5.9(0.1)	8.9(0.1)	0.4(0.1)	1.3(0.1)
G180.92+04.53	2.1(0.2)	4.2(0.2)	1.8(0.3)	1.7(0.1)	1.3(0.1)	2.7(0.2)	1.4(0.1)	1.2(0.4)	0.6(0.1)
G181.73-19.35	8.7(0.1)	1.6(0.1)	8.7(0.4)	8.8(0.1)	1.1(0.1)	4.5(0.2)			
G181.84+00.31	2.5(0.2)	2.7(0.4)	6.0(1.1)	2.9(0.1)	1.6(0.1)	3.4(0.1)	2.9(0.1)	1.1(0.1)	0.6(0.1)
G182.04+00.41	2.0(0.3)	2.9(0.3)	4.0(0.7)	2.7(0.1)	1.4(0.1)	3.6(0.1)	2.9(0.1)	1.0(0.1)	0.7(0.1)
G190.17-13.78	0.6(0.1)	1.4(0.1)	8.5(0.5)	1.1(0.1)	1.2(0.1)	5.4(0.3)			
G191.51-00.76	-0.2(0.1)	2.0(0.1)	10.0(1.0)	0.0(0.1)	1.3(0.1)	5.4(0.2)	0.0(0.1)	0.9(0.1)	1.3(0.2)
G192.12-10.90	10.0(0.1)	1.4(0.1)	14.0(0.2)	10.0(0.1)	0.9(0.1)	7.7(0.1)	10.1(0.1)	0.7(0.1)	1.9(0.1)
G192.28-11.33	10.7(0.2)	1.3(0.2)	12.7(0.2)	10.1(0.1)	1.4(0.1)	7.9(0.1)	10.1(0.1)	0.9(0.1)	1.1(0.1)
G192.32-11.87	12.0(0.1)	1.3(0.1)	14.3(0.3)	12.0(0.1)	0.9(0.1)	7.3(0.1)	11.9(0.1)	0.8(0.1)	1.3(0.1)
G192.94-03.73	4.5(0.2)	2.3(0.2)	1.6(0.2)	4.5(3.3)	1.3(6.0)	2.0(0.2)	4.1(0.1)	1.1(0.2)	0.5(0.2)
G194.80-03.41	11.9(0.1)	2.6(0.1)	6.7(0.2)	12.6(0.1)	2.4(0.1)	3.1(0.2)			
G198.03-15.24	-0.2(0.1)	1.2(0.1)	11.2(0.1)	-0.1(0.1)	0.8(0.1)	5.4(0.1)	0.0(0.1)	0.5(0.1)	0.6(0.1)
G198.56-09.10	11.8(0.1)	1.7(0.1)	12.0(0.4)	11.7(0.1)	1.3(0.1)	5.7(0.1)	11.6(0.1)	1.1(0.1)	0.6(0.1)
G199.88+00.93	4.8(0.2)	1.8(0.2)	4.9(0.2)	5.7(0.1)	1.8(0.1)	4.2(0.4)	5.7(0.1)	1.3(0.1)	1.2(0.1)
G201.13+00.31	5.0(0.1)	2.4(0.1)	7.7(0.9)	5.0(0.1)	1.4(0.1)	4.7(0.1)	5.0(0.1)	1.1(0.1)	0.9(0.1)
G201.44+00.65	6.1(0.2)	4.1(0.2)	7.9(0.1)	6.5(0.1)	2.3(0.1)	3.4(0.1)	6.5(0.1)	1.6(0.1)	1.1(0.1)
G201.59+00.55a	3.0(0.1)	1.6(0.1)	3.7(0.2)	4.0(0.2)	1.8(0.2)	4.6(0.1)	4.1(0.1)	1.5(0.2)	0.7(0.1)

**Table C.1.** Continued

Name	$V_{\text{LSR}}(\text{CO})$ km s $^{-1}$	$\Delta v_{\text{CO}}$ km s $^{-1}$	$T_{\text{mb},^{12}\text{CO}}$ K	$V_{\text{LSR}}(^{13}\text{CO})$ km s $^{-1}$	$\Delta v_{^{13}\text{CO}}$ km s $^{-1}$	$T_{\text{mb},^{13}\text{CO}}$ K	$V_{\text{LSR}}(\text{C}^{18}\text{O})$ km s $^{-1}$	$\Delta v_{\text{C}^{18}\text{O}}$ km s $^{-1}$	$T_{\text{mb},\text{C}^{18}\text{O}}$ K
G201.59+00.55b	4.9(0.1)	3.8(0.1)	8.5(0.2)	5.7(0.2)	1.1(0.2)	3.0(0.1)	5.6(0.1)	0.7(0.2)	0.5(0.1)
G202.30-08.91	12.0(0.1)	2.1(0.1)	8.9(0.2)	12.0(0.1)	1.7(0.1)	4.9(0.6)	11.9(0.1)	1.0(0.1)	1.1(0.1)
G203.20-11.20	10.6(0.1)	2.2(0.1)	8.0(0.2)	10.6(0.1)	1.6(0.1)	6.3(0.2)	10.5(0.1)	1.2(0.1)	2.4(0.1)
G203.75-08.49	12.1(0.2)	1.4(0.2)	6.0(0.3)	11.6(0.1)	1.0(0.1)	5.0(0.1)	11.6(0.1)	0.7(0.1)	1.1(0.1)
G204.82-13.88	7.3(0.3)	3.6(0.3)	8.4(0.2)	7.9(0.2)	1.2(0.2)	3.5(0.1)	8.4(0.1)	1.0(0.1)	2.0(0.1)
G205.57-08.25	11.8(0.1)	1.7(0.2)	4.5(0.4)	11.5(0.1)	1.6(0.1)	3.3(0.2)	11.3(0.1)	1.1(0.3)	0.9(0.3)
G206.10-15.77	9.5(0.4)	3.1(0.9)	12.5(4.3)	9.3(0.2)	1.5(0.4)	5.7(1.6)	9.3(0.1)	0.7(0.1)	1.3(0.2)
G208.56+02.36	9.3(0.1)	1.5(0.1)	8.8(0.2)	9.3(0.1)	1.1(0.1)	3.6(0.1)	9.3(0.1)	0.6(0.1)	0.8(0.1)
G217.13-12.54	11.6(0.1)	3.4(0.1)	6.8(0.3)	11.7(0.1)	1.3(0.1)	3.6(0.1)			
G222.23+01.21	28.2(0.1)	2.4(0.1)	6.2(0.3)	28.4(0.1)	1.5(0.1)	3.1(0.1)	28.5(0.1)	1.0(0.2)	0.7(0.1)
G224.27-00.82	15.8(0.2)	2.9(0.2)	6.2(0.5)	14.3(0.1)	2.7(0.1)	4.9(0.3)	14.4(0.1)	1.4(0.1)	3.0(0.3)
G224.47-00.65	14.8(0.1)	3.6(0.2)	6.2(0.6)	15.2(0.1)	1.5(0.1)	4.8(0.4)			

**Table C.2.** Derived Parameters of CO lines

Name	$T_{\text{ex(CO)}}$ K	$\tau_{^{13}\text{CO}}$	$\tau_{\text{C}^{18}\text{O}}$	$N_{^{13}\text{CO}}$ $10^{15}\text{cm}^{-2}$	$N_{\text{C}^{18}\text{O}}$ $10^{15}\text{cm}^{-2}$	$N_{\text{H}_2}(^{13}\text{CO})$ $10^{22}\text{cm}^{-2}$	$N_{\text{H}_2}(\text{C}^{18}\text{O})$ $10^{22}\text{cm}^{-2}$	Name	$T_{\text{ex(CO)}}$ K	$\tau_{^{13}\text{CO}}$	$\tau_{\text{C}^{18}\text{O}}$	$N_{^{13}\text{CO}}$ $10^{15}\text{cm}^{-2}$	$N_{\text{C}^{18}\text{O}}$ $10^{15}\text{cm}^{-2}$	$N_{\text{H}_2}(^{13}\text{CO})$ $10^{22}\text{cm}^{-2}$	$N_{\text{H}_2}(\text{C}^{18}\text{O})$ $10^{22}\text{cm}^{-2}$
G005.03+19.07	17.9(0.2)	0.8(0.01)	0.1(0.01)	14.0(0.5)	1.4(0.2)	1.2(0.4)	1.0(0.1)	G110.52+19.17	7.1(0.2)	1.4(0.03)	0.6(0.02)	2.3(0.3)	0.7(0.1)	0.2(0.3)	0.5(0.1)
G005.29+11.07	19.6(0.3)	0.7(0.01)	0.1(0.01)	8.6(0.3)	1.0(0.1)	0.8(0.3)	0.7(0.1)	G110.65+09.65	11.6(0.2)	1.1(0.01)	0.2(0.01)	13.0(0.7)	1.6(0.2)	1.2(0.6)	1.1(0.2)
G005.80+19.92	9.4(0.3)		0.2(0.58)		0.6(1.8)		0.4(1.2)	G111.66+20.20	9.2(0.3)	2.8(0.20)	0.3(0.31)	18.0(2.6)	1.2(1.5)	1.6(2.3)	0.8(1.0)
G006.08+20.26	13.6(0.2)	1.8(0.01)	0.2(0.01)	18.0(0.7)	1.4(0.2)	1.6(0.6)	1.0(0.1)	G111.68+19.74	6.7(0.3)	0.7(0.01)	0.4(0.01)	1.6(0.3)	0.6(0.1)	0.1(0.3)	0.4(0.1)
G006.32+20.44	14.2(0.2)	1.4(0.01)	0.4(0.01)	13.0(0.5)	2.2(0.2)	1.1(0.5)	1.5(0.1)	G111.77+20.26	9.1(0.2)	1.0(0.01)	0.2(0.01)	4.2(0.4)	0.8(0.1)	0.4(0.3)	0.6(0.1)
G006.41+20.56	16.0(0.3)	0.8(0.01)	0.2(0.01)	8.6(2.2)	2.0(0.2)	0.8(1.9)	1.4(0.1)	G112.25+13.82	8.1(0.1)	1.7(0.02)	0.6(0.02)	5.4(0.6)	2.0(0.2)	0.5(0.5)	1.4(0.1)
G006.70+20.66	15.2(0.2)	1.1(0.01)	0.2(0.01)	16.0(0.6)	2.4(0.2)	1.4(0.5)	1.7(0.1)	G114.16+14.80	9.8(0.3)	0.8(0.02)	0.3(0.02)	6.7(0.6)	1.2(0.2)	0.6(0.5)	0.8(0.1)
G006.98+20.72	15.0(0.3)	0.8(0.01)	0.1(0.01)	7.0(0.4)	0.6(0.1)	0.6(0.3)	0.4(0.1)	G114.56+14.72	8.2(0.3)	1.0(0.01)	0.4(0.03)	3.5(0.5)	1.4(0.2)	0.3(0.5)	1.0(0.2)
G007.53+21.10	19.7(0.2)	0.7(0.01)	0.1(0.01)	11.0(0.4)	0.7(0.2)	1.0(0.4)	0.5(0.1)	G114.67+14.47	10.4(0.2)	2.0(0.08)	0.3(0.07)	20.0(1.6)	2.1(0.7)	1.7(1.4)	1.5(0.5)
G007.80+21.10	11.4(0.2)	1.3(0.01)	0.1(0.01)	6.4(0.5)	0.4(0.1)	0.6(0.5)	0.3(0.1)	G115.81-03.54	8.8(0.2)	1.2(0.02)	0.2(0.03)	5.6(0.4)	0.6(0.2)	0.5(0.4)	0.4(0.1)
G008.52+21.84	13.9(0.4)	1.1(0.02)	0.2(0.02)	9.5(0.9)	1.5(0.3)	0.9(0.8)	1.0(0.2)	G116.08-02.38	10.3(0.2)	0.7(0.01)	0.1(0.01)	4.9(0.5)	1.0(0.2)	0.4(0.5)	0.7(0.1)
G008.67+22.14	14.4(0.3)	1.0(0.01)	0.3(0.01)	8.0(0.5)	1.5(0.2)	0.7(0.4)	1.0(0.1)	G117.11+12.42	10.8(0.2)	1.3(0.03)	0.3(0.03)	8.9(0.6)	1.1(0.2)	0.8(0.6)	0.8(0.1)
G015.16+07.23	11.6(1.2)	0.6(0.08)	0.0(0.09)	5.4(1.8)	0.2(0.5)	0.5(1.6)	0.1(0.3)	G120.16+03.09	10.6(0.2)	0.8(0.01)	0.1(0.01)	6.8(1.1)	1.1(0.1)	0.6(1.0)	0.7(0.1)
G028.45-06.39	11.4(0.2)	1.0(0.01)	0.3(0.01)	7.8(0.4)	1.3(0.1)	0.7(0.3)	0.9(0.1)	G120.67+02.66	16.3(0.6)	0.5(0.02)	0.1(0.02)	16.0(2.0)	1.5(0.8)	1.4(1.8)	1.0(0.5)
G038.36-00.95	9.9(0.3)	1.3(0.05)	0.2(0.06)	14.0(1.6)	2.0(0.8)	1.3(1.4)	1.4(0.5)	G120.98+02.66	12.3(0.6)	0.6(0.03)	0.1(0.03)	8.2(1.3)	0.8(0.6)	0.7(1.2)	0.6(0.4)
G049.76-07.25	8.3(0.3)	1.0(0.01)		4.8(0.4)		0.4(0.4)		G121.35+03.39	8.0(0.4)	1.3(0.11)	0.3(0.12)	7.8(1.4)	1.1(0.6)	0.7(1.3)	0.8(0.4)
G057.10+03.65	10.9(0.2)	1.1(0.01)	0.2(0.01)	10.0(0.8)	1.6(0.2)	0.9(0.7)	1.1(0.1)	G123.66+24.89	8.7(0.2)	0.9(0.01)	0.1(0.01)	5.0(0.4)	0.4(0.1)	0.5(0.3)	0.3(0.1)
G065.43-03.15	5.4(0.2)		0.5(1.74)			0.7(2.5)	0.5(1.7)	G127.85+14.16	7.6(0.2)		0.6(0.18)		1.3(0.5)		0.9(0.3)
G070.44-01.54	10.0(0.2)	0.6(0.01)	0.2(0.01)	11.0(1.5)	2.3(0.2)	1.0(1.4)	1.6(0.1)	G127.88+02.66	12.2(0.2)	1.1(0.01)	0.1(0.01)	13.0(0.4)	1.0(0.1)	1.2(0.4)	0.7(0.1)
G070.72-00.63	12.2(0.5)	0.6(0.02)			15.0(2.8)		1.3(2.5)	G128.89+13.68	9.8(0.6)	1.3(0.16)	0.1(0.16)	5.8(1.4)	0.3(0.6)	0.5(1.3)	0.2(0.4)
G074.11+00.11	4.4(0.2)		1.5(0.15)		5.0(0.9)		3.5(0.6)	G128.95-00.18	11.8(0.5)	0.8(0.05)	0.1(0.06)	6.7(1.1)	0.7(0.5)	0.6(0.9)	0.5(0.4)
G074.11+00.11	9.0(0.2)	0.5(0.01)		7.1(0.5)		0.6(0.4)		G132.29+09.36	7.3(0.1)	1.2(0.01)	0.2(0.01)	6.7(0.4)	0.4(0.1)	0.6(0.4)	0.3(0.1)
G084.79-01.11	11.2(0.3)	1.2(0.05)	0.2(0.05)	16.0(1.7)	2.0(0.7)	1.4(1.5)	1.4(0.5)	G133.28+08.81	8.9(0.2)	1.2(0.01)	0.1(0.01)	8.1(1.3)	0.9(0.2)	0.7(1.1)	0.6(0.1)
G089.36-00.67	10.4(0.7)	0.7(0.06)	0.1(0.07)	12.0(2.5)	1.0(0.8)	1.0(2.2)	0.7(0.6)	G133.48+09.02	13.3(1.5)	0.7(0.06)	0.1(0.13)	14.0(5.6)	1.8(2.4)	1.2(5.0)	1.3(1.6)
G089.64-06.59	8.5(0.1)	0.4(0.01)	0.1(0.01)	1.8(0.3)	0.3(0.1)	0.2(0.3)	0.2(0.1)	G133.48+09.02	9.0(1.5)	1.1(0.29)	0.2(0.48)	12.0(9.2)	1.4	1.1(8.1)	1.0(2.9)
G089.75-02.16	11.7(0.2)	0.5(0.01)	0.1(0.01)	3.4(0.3)	0.6(0.1)	0.3(0.2)	0.4(0.1)	G140.97+05.73	9.5(0.2)	1.7(0.05)	0.3(0.04)	12.0(0.9)	1.2(0.3)	1.1(0.8)	0.8(0.2)
G089.93-01.94	14.7(0.6)	0.8(0.03)	0.1(0.04)	10.0(1.3)	1.0(0.5)	0.9(1.1)	0.7(0.4)	G144.66+00.16	10.7(0.3)	1.0(0.06)		6.3(1.0)		0.6(0.9)	
G091.73+04.36	8.1(0.3)	2.0(0.20)	0.5(0.19)	16.0(2.9)	2.2(1.1)	1.4(2.6)	1.6(0.7)	G147.01+03.39	8.1(0.4)	1.3(0.13)	0.1(0.15)	3.7(0.8)	0.3(0.5)	0.3(0.7)	0.2(0.3)
G093.20+09.53	6.2(0.3)	1.4(0.07)	0.3(0.09)	3.7(0.7)	0.5(0.3)	0.3(0.6)	0.3(0.2)	G149.23+03.07	8.3(1.2)	1.1(0.38)	0.1(0.40)	3.7(2.4)	0.2(0.9)	0.3(2.1)	0.1(0.6)
G093.22-04.59	7.6(0.2)	0.8(0.01)	0.1(0.01)	3.8(0.6)	0.3(0.1)	0.3(0.6)	0.2(0.1)	G149.41+03.37	9.0(0.4)	0.9(0.05)	0.1(0.05)	4.8(0.8)	0.3(0.3)	0.4(0.7)	0.2(0.2)
G093.62-04.44	8.8(0.2)	1.2(0.01)	0.3(0.01)	7.4(0.6)	1.6(0.2)	0.7(0.6)	1.2(0.1)	G149.52-01.23	15.3(0.2)	0.3(0.01)	0.1(0.01)	3.7(0.5)	1.0(0.2)	0.3(0.4)	0.7(0.1)
G093.91+10.02	5.8(0.3)		0.7(0.24)		1.0(0.5)		0.7(0.4)	G150.22+03.91	9.8(0.4)	1.2(0.08)	0.1(0.07)	8.0(1.1)	0.2(0.2)	0.7(1.0)	0.1(0.2)
G093.99-04.91	8.3(0.2)	2.4(0.05)	0.3(0.14)	11.0(1.1)	0.8(0.5)	1.0(1.0)	0.5(0.4)	G150.44+03.95	11.1(1.1)	1.1(0.23)	0.2(0.23)	8.0(3.3)	0.7(1.1)	0.7(2.9)	0.5(0.8)
G094.08+09.46	8.7(0.3)	0.6(0.01)	0.1(0.01)	4.2(0.4)	0.5(0.2)	0.4(0.4)	0.4(0.1)	G151.08+04.46	10.8(0.7)	1.4(0.23)	0.2(0.24)	6.5(1.9)	0.6(0.7)	0.6(1.7)	0.4(0.5)
G095.11+06.50	7.7(0.2)	0.7(0.01)	0.3(0.01)	3.1(0.6)	0.7(0.1)	0.3(0.5)	0.5(0.1)	G151.45+03.95	7.7(0.2)	1.4(0.05)	0.2(0.04)	7.9(1.5)	0.6(0.3)	0.7(1.3)	0.4(0.2)
G095.51+09.97	8.8(1.3)	0.4(0.08)	0.2(0.10)	2.4(1.1)	0.5(0.4)	0.2(1.0)	0.4(0.3)	G154.07+05.09	10.2(0.2)	0.9(0.01)	0.1(0.01)	8.7(0.6)	0.2(0.1)	0.8(0.5)	0.1(0.1)
G096.59+10.29	8.2(0.2)	1.8(0.07)	0.4(0.11)	5.2(0.6)	0.6(0.3)	0.5(0.5)	0.4(0.2)	G154.07+05.21	9.0(0.2)	0.3(0.01)	0.1(0.01)	1.2(0.2)	0.3(0.1)	0.1(0.2)	0.2(0.1)
G096.94+10.25	10.5(0.1)	0.7(0.01)	0.2(0.01)	6.3(0.2)	1.0(0.1)	0.6(0.2)	0.7(0.1)	G154.68-15.34	7.4(0.2)	1.3(0.03)	0.2(0.02)	5.4(0.7)	0.4(0.1)	0.5(0.6)	0.3(0.1)
G097.09+10.12	7.0(0.2)	1.8(0.07)	0.5(0.09)	6.3(0.8)	1.1(0.3)	0.6(0.7)	0.7(0.2)	G154.90+04.61	9.5(0.2)	0.5(0.01)	0.1(0.01)	2.9(0.2)	0.3(0.1)	0.3(0.2)	0.2(0.1)
G097.20+09.87	7.6(0.2)	2.4(0.09)	0.5(0.11)	9.8(0.9)	1.4(0.4)	0.9(0.8)	1.0(0.3)	G154.90+04.61	11.8(0.2)	0.4(0.01)	0.0(0.01)	4.9(0.3)	0.1(0.1)	0.4(0.3)	0.1(0.1)
G097.38+09.95	7.1(0.1)	1.2(0.02)	0.2(0.03)	4.1(0.3)	0.4(0.1)	0.4(0.2)	0.3(0.1)	G155.45-14.59	6.0(0.1)		0.7(0.08)		1.3(0.3)		0.9(0.2)
G098.52+13.88	5.5(0.3)		0.2(0.32)		0.3(0.5)		0.2(0.4)	G155.67+05.11	11.4(0.4)	0.6(0.01)	0.1(0.01)	6.1(0.7)	0.3(0.2)	0.6(0.7)	0.2(0.1)
G098.89+14.01	9.1(0.2)	1.0(0.01)	0.1(0.01)	3.4(0.3)	0.4(0.1)	0.3(0.2)	0.3(0.1)	G156.20+05.26	11.4(0.3)	1.2(0.04)	0.1(0.04)	6.0(0.6)	0.4(0.2)	0.5(0.5)	0.3(0.1)
G098.96+13.68	9.5(0.3)	0.8(0.01)	0.1(0.01)	4.4(0.4)	0.3(0.1)	0.4(0.3)	0.2(0.1)	G156.90-08.49	7.5(0.1)	1.0(0.01)	0.5(0.01)	8.2(0.5)	1.2(0.1)	0.7(0.5)	0.9(0.1)
G102.34+15.96	9.3(0.1)	1.6(0.01)	0.2(0.01)	8.1(0.3)	0.6(0.1)	0.7(0.3)	0.4(0.1)	G157.10-08.70	9.1(0.2)	1.1(0.01)	0.3(0.01)	5.7(0.3)	1.2(0.1)	0.5(0.2)	0.8(0.1)
G102.70+15.19	9.9(0.2)	0.9(0.01)	0.2(0.01)	4.4(0.4)	0.8(0.1)	0.4(0.3)	0.6(0.1)	G157.12-11.56	13.3(0.7)	0.6(0.05)	0.1(0.05)	7.8(1.4)	0.6(0.5)	0.7(1.3)	0.5(0.4)
G102.72+15.36	9.5(0.2)	0.8(0.01)	0.2(0.01)	4.2(0.4)	0.7(0.1)	0.4(0.3)	0.5(0.1)	G157.25-01.00	10.9(1.0)	2.7(1.41)	0.4(1.45)	13.0(8.8)	1.3	1.1(7.8)	0.9(3.4)
G103.90+13.97	5.4(0.2)		0.8(0.12)		1.1(0.3)		0.8(0.2)	G157.60-12.17	9.9(0.2)	0.9(0.33)	0.1(0.01)	6.2(3.6)	0.8(0.1)	0.6(3.2)	0.5(0.1)
G108.10+13.19	8.6(0.6)	1.2(0.20)	0.3(0.20)	5.6(1.7)	0.8(0.6)</td										

**Table C.2.** continued

Name	$T_{\text{ex(CO)}}$ K	$\tau_{^{13}\text{CO}}$	$\tau_{\text{C}^{18}\text{O}}$	$N_{^{13}\text{CO}}$ $10^{15}\text{cm}^{-2}$	$N_{\text{C}^{18}\text{O}}$ $10^{15}\text{cm}^{-2}$	$N_{\text{H}_2}(^{13}\text{CO})$ $10^{22}\text{cm}^{-2}$	$N_{\text{H}_2}(\text{C}^{18}\text{O})$ $10^{22}\text{cm}^{-2}$	Name	$T_{\text{ex(CO)}}$ K	$\tau_{^{13}\text{CO}}$	$\tau_{\text{C}^{18}\text{O}}$	$N_{^{13}\text{CO}}$ $10^{15}\text{cm}^{-2}$	$N_{\text{C}^{18}\text{O}}$ $10^{15}\text{cm}^{-2}$	$N_{\text{H}_2}(^{13}\text{CO})$ $10^{22}\text{cm}^{-2}$	$N_{\text{H}_2}(\text{C}^{18}\text{O})$ $10^{22}\text{cm}^{-2}$
G158.24-21.80	9.8(0.1)	0.6(0.01)	0.1(0.01)	6.1(0.2)	0.6(0.2)	0.6(0.2)	0.4(0.1)	G173.45-13.34	10.2(0.2)	1.0(0.01)	0.4(0.01)	4.6(0.4)	1.0(0.1)	0.4(0.3)	0.7(0.1)
G158.37-20.72	16.2(0.4)	0.6(0.01)	0.1(0.01)	14.0(0.9)	1.3(0.4)	1.2(0.8)	0.9(0.3)	G173.89-17.64	10.7(0.4)	1.1(0.03)	0.3(0.01)	6.9(0.9)	0.8(0.2)	0.6(0.8)	0.6(0.1)
G158.77-33.30	8.9(0.1)	0.8(0.05)	0.1(0.01)	4.1(0.6)	0.5(0.2)	0.4(0.6)	0.4(0.1)	G173.95-13.74	9.9(0.3)	2.7(0.11)	0.7(0.14)	13.0(2.2)	2.7(0.8)	1.2(2.0)	1.9(0.6)
G158.86-21.60	14.0(0.4)	0.6(0.01)	0.1(0.01)	9.5(0.9)	0.8(0.3)	0.8(0.8)	0.6(0.2)	G174.06-15.81	13.2(0.2)	1.4(0.03)	0.3(0.02)	17.0(0.9)	2.1(0.3)	1.5(0.8)	1.5(0.2)
G159.01-08.46	7.3(0.2)	1.5(0.05)	0.3(0.04)	11.0(0.9)	1.0(0.3)	1.0(0.8)	0.7(0.2)	G174.39-13.43	9.8(0.2)	1.2(0.02)	0.5(0.01)	5.9(0.4)	2.3(0.2)	0.5(0.3)	1.6(0.1)
G159.21-20.44	13.5(0.2)	1.8(0.04)	0.5(0.04)	32.0(4.7)	5.9(0.8)	2.9(4.2)	4.1(0.5)	G174.44-15.75	13.4(0.3)	1.0(0.01)	0.1(0.01)	11.0(0.9)	0.8(0.2)	1.0(0.8)	0.5(0.1)
G159.34+11.20	12.5(0.3)	0.7(0.01)	0.1(0.01)	4.1(0.3)	0.3(0.1)	0.4(0.3)	0.2(0.1)	G174.81-15.15	6.9(0.1)		0.3(0.08)		0.4(0.2)		0.3(0.1)
G159.65-19.68	10.6(0.1)	0.3(0.01)	0.1(0.01)	1.0(0.2)	0.2(0.1)	0.1(0.1)	0.1(0.1)	G175.49-16.80	9.4(0.3)	1.6(0.04)	0.4(0.04)	6.7(0.7)	1.0(0.2)	0.6(0.6)	0.7(0.1)
G159.65+11.39	18.1(0.2)	0.7(0.03)	0.1(0.01)	18.0(1.8)	1.5(0.2)	1.6(1.6)	1.1(0.1)	G177.14-01.21	11.7(0.3)	0.8(0.01)	0.1(0.01)	13.0(0.8)	1.5(0.3)	1.1(0.7)	1.0(0.2)
G159.67-34.31	8.9(0.1)	0.9(0.01)	0.1(0.01)	3.5(0.2)	0.2(0.1)	0.3(0.2)	0.1(0.1)	G177.86+01.04	9.0(0.2)	0.5(0.01)		4.0(0.7)		0.4(0.6)	
G159.76-19.62	12.6(0.3)	1.1(0.10)	0.2(0.01)	15.0(4.0)	1.0(0.2)	1.4(3.5)	0.7(0.2)	G177.89-20.16	11.5(1.5)	1.2(0.25)	0.2(0.38)	7.1(3.6)	0.7(1.5)	0.6(3.2)	0.5(1.0)
G160.51-16.84	17.5(0.2)	0.9(0.01)	0.2(0.01)	20.0(0.4)	3.1(0.1)	1.8(0.4)	2.2(0.1)	G177.97-09.72	14.5(0.3)	1.0(0.02)	0.3(0.01)	7.9(0.5)	1.7(0.2)	0.7(0.4)	1.2(0.1)
G160.53-19.72	10.4(0.1)	0.6(0.01)	0.1(0.01)	3.7(0.2)	0.4(0.2)	0.3(0.2)	0.3(0.1)	G178.28-00.61	10.6(0.2)	0.8(0.01)	0.1(0.01)	7.4(0.5)	0.8(0.1)	0.7(0.4)	0.5(0.1)
G160.53-09.84	14.1(0.2)	0.7(0.01)	0.2(0.01)	13.0(0.5)	1.5(0.1)	1.2(0.4)	1.1(0.1)	G178.98-06.74	11.2(0.2)	1.6(0.01)	0.4(0.01)	9.7(0.4)	1.3(0.1)	0.9(0.4)	0.9(0.1)
G161.21-08.72	8.3(0.2)	1.4(0.02)	0.2(0.01)	9.1(0.6)	0.8(0.2)	0.8(0.6)	0.5(0.1)	G180.81-19.66	11.9(0.5)	1.1(0.08)	0.2(0.08)	6.4(1.1)	0.6(0.4)	0.6(0.9)	0.4(0.3)
G161.43-35.59	11.6(0.2)	0.9(0.01)	0.1(0.01)	4.1(0.3)	0.3(0.1)	0.4(0.2)	0.2(0.1)	G180.92+04.53	4.8(0.3)		0.4(0.31)		0.8(0.9)		0.5(0.7)
G161.60-08.34	5.8(0.7)	1.1(0.16)	1.1(0.01)	2.4(2.1)	3.7(1.3)	0.2(1.9)	2.6(0.9)	G181.73-19.35	12.0(0.4)	0.7(0.01)		6.5(0.6)		0.6(0.6)	
G161.85-35.75	9.6(0.3)	1.1(0.01)		4.0(0.4)		0.4(0.3)		G181.84+00.31	9.2(1.1)	0.8(0.18)	0.1(0.19)	6.7(3.0)	0.6(0.2)	0.6(2.6)	0.4(0.9)
G162.46-08.70	4.7(0.1)							G182.04+00.41	7.2(0.7)	2.3(1.22)	0.2(1.25)	11.0(7.5)	0.7(0.8)	0.9(6.7)	0.5(3.2)
G163.32-08.42	5.9(0.1)	0.6(0.03)	0.8(0.03)	0.8(0.2)	1.8(0.2)	0.1(0.1)	1.3(0.2)	G190.17-13.78	11.7(0.5)	1.0(0.01)		9.9(1.5)		0.9(1.4)	
G165.16-07.55	8.1(0.2)	1.0(0.01)	0.2(0.01)	3.4(0.3)	0.6(0.1)	0.3(0.3)	0.4(0.1)	G191.51-00.76	13.3(1.0)	0.8(0.08)	0.1(0.08)	10.0(2.5)	1.2(1.0)	0.9(2.2)	0.9(0.7)
G165.34-07.51	8.9(0.1)	1.1(0.11)	0.1(0.01)	6.6(1.4)	0.2(0.1)	0.6(1.3)	0.1(0.1)	G192.12-10.90	17.3(0.2)	0.8(0.01)	0.1(0.01)	11.0(0.4)	1.6(0.2)	1.0(0.4)	1.1(0.1)
G165.34-07.51	7.6(0.1)	1.0(0.13)	0.2(0.01)	3.5(1.0)	0.8(0.1)	0.3(0.9)	0.6(0.1)	G192.28-11.33	16.0(0.2)	1.0(0.01)	0.1(0.01)	19.0(0.5)	1.1(0.1)	1.7(0.4)	0.8(0.1)
G165.69-09.14	7.9(0.6)	1.9(0.28)	0.3(0.32)	11.0(3.4)	0.7(1.0)	1.0(3.1)	0.5(0.7)	G192.32-11.87	17.6(0.3)	0.7(0.01)	0.1(0.01)	11.0(0.6)	1.2(0.2)	1.0(0.5)	0.8(0.2)
G168.00-15.69	14.0(0.6)	0.6(0.03)	0.3(0.03)	5.3(1.7)	1.7(0.4)	0.5(1.5)	1.2(0.3)	G192.94-03.73	4.5(0.3)		0.4(0.33)		0.8(0.8)		0.5(0.5)
G168.13-16.39	10.8(0.2)	0.8(0.01)	0.4(0.01)	3.0(0.3)	2.3(0.2)	0.3(0.2)	1.6(0.1)	G194.80-03.41	9.9(0.2)	0.6(0.01)		8.6(0.7)		0.8(0.7)	
G168.72-15.48	12.4(0.4)	1.2(0.01)	0.4(0.03)	14.0(1.6)	1.9(0.4)	1.3(1.4)	1.3(0.3)	G198.03-15.24	14.5(0.1)	0.7(0.01)	0.1(0.01)	5.9(0.3)	0.3(0.1)	0.5(0.3)	0.2(0.1)
G169.76-16.15	10.3(0.2)	1.1(0.01)	0.3(0.01)	6.9(0.3)	1.2(0.1)	0.6(0.3)	0.8(0.1)	G198.56-09.10	15.3(0.4)	0.6(0.01)	0.1(0.01)	11.0(0.8)	0.8(0.2)	1.0(0.7)	0.5(0.2)
G169.76-16.15	12.7(0.2)	0.2(0.01)	0.2(0.01)	1.4(0.1)	1.1(0.2)	0.1(0.1)	0.7(0.1)	G199.88+00.93	8.0(0.2)	2.1(0.48)	0.3(0.06)	16.0(4.8)	1.5(0.4)	1.4(4.3)	1.1(0.3)
G169.84-07.61	10.5(0.1)	0.9(0.01)	0.3(0.01)	4.5(0.2)	0.8(0.1)	0.4(0.2)	0.6(0.1)	G201.13+00.31	10.9(1.0)	0.9(0.14)	0.1(0.14)	9.2(3.0)	0.9(1.3)	0.8(2.7)	0.6(0.9)
G169.98-04.27	9.9(0.2)	1.2(0.01)	0.2(0.01)	4.8(0.2)	0.6(0.1)	0.4(0.2)	0.4(0.1)	G201.44+00.65	11.2(0.1)	0.6(0.01)	0.1(0.01)	9.3(0.7)	1.7(0.4)	0.8(0.6)	1.2(0.3)
G170.00-16.14	7.7(0.3)	1.7(0.05)	0.2(0.01)	4.9(0.9)	0.7(0.3)	0.4(0.8)	0.5(0.2)	G201.59+00.55	6.9(0.2)		0.2(0.16)		1.0(1.0)		0.7(0.7)
G170.13-16.06	6.9(0.2)		0.5(0.13)		0.9(0.4)		0.6(0.3)	G201.59+00.55	11.8(0.2)	0.4(0.01)	0.1(0.01)	3.8(0.8)	0.3(0.2)	0.3(0.7)	0.2(0.1)
G170.26-16.02	9.7(0.3)	2.1(0.17)	0.3(0.15)	14.0(2.0)	1.3(0.8)	1.3(1.8)	0.9(0.6)	G202.30-08.91	12.2(0.2)	0.8(0.12)	0.1(0.01)	11.0(2.6)	1.1(0.1)	1.0(2.3)	0.8(0.1)
G170.81-18.34	11.6(0.3)	1.4(0.02)	0.3(0.03)	8.4(0.7)	1.2(0.3)	0.8(0.7)	0.8(0.2)	G203.20-11.20	11.3(0.3)	1.5(0.01)	0.3(0.03)	18.0(1.1)	3.1(0.5)	1.6(1.0)	2.2(0.3)
G170.88-10.92	8.5(2.1)	2.2(2.86)	0.3(3.04)	7.0(12.0)	0.6	0.6(11.0)	0.4(4.7)	G203.75-08.49	9.2(0.3)	1.8(0.15)	0.2(0.15)	9.0(1.5)	0.7(0.7)	0.8(1.3)	0.5(0.5)
G170.99-15.81	7.3(0.5)		1.3(0.28)		2.8(1.2)		1.9(0.8)	G204.82-13.88	11.6(0.2)	0.5(0.01)	0.3(0.01)	5.2(0.9)	2.3(0.2)	0.5(0.8)	1.6(0.2)
G171.14-17.58	10.3(0.9)	0.9(0.09)	0.4(0.12)	5.1(1.5)	0.9(0.5)	0.5(1.3)	0.6(0.4)	G205.57-08.25	7.6(0.4)	1.4(0.08)	0.2(0.03)	7.8(1.6)	1.0(0.5)	0.7(1.4)	0.7(0.4)
G171.34+02.59	11.0(0.3)	0.5(0.01)	0.1(0.01)	7.8(1.0)	0.7(0.1)	0.7(0.9)	0.5(0.1)	G206.10-15.77	15.8(4.3)	0.6(0.05)	0.1(0.25)	12.0(11.0)	1.1(9.4)	0.7(2.1)	
G171.49-14.90	10.1(0.3)	1.5(0.01)	0.5(0.01)	8.6(0.8)	1.3(0.2)	0.8(0.8)	0.9(0.1)	G208.56+02.36	12.1(0.2)	0.5(0.01)	0.1(0.01)	4.6(0.3)	0.5(0.1)	0.4(0.3)	0.3(0.1)
G171.51-10.59	7.0(0.2)		0.6(0.12)		0.9(0.3)		0.6(0.2)	G217.13-12.54	10.0(0.3)	0.8(0.01)		5.8(0.6)		0.5(0.5)	
G171.80-15.32	10.7(0.4)	2.0(0.10)	0.2(0.10)	12.0(1.6)	1.2(0.9)	1.1(1.4)	0.8(0.6)	G222.23+01.21	9.4(0.3)	0.7(0.01)	0.1(0.01)	5.5(0.6)	0.7(0.2)	0.5(0.6)	0.5(0.1)
G171.84-05.22	11.7(0.3)	1.2(0.01)	0.2(0.01)	5.8(0.5)	0.7(0.2)	0.5(0.4)	0.5(0.1)	G224.27-00.82	9.4(0.5)	1.6(0.04)	0.7(0.05)	22.0(3.2)	4.8(1.1)	2.0(2.9)	3.3(0.8)
G172.06-15.21	9.4(0.3)	2.3(0.13)	0.3(0.16)	9.6(1.2)	1.2(0.7)	0.9(1.1)	0.8(0.5)	G224.47-00.65	9.4(0.6)	1.6(0.05)		12.0(2.8)		1.1(2.5)	
G172.13-16.93	11.9(0.1)	1.1(0.01)	0.3(0.01)	7.9(0.3)	1.6(0.1)	0.7(0.3)	1.1(0.1)								
G172.85+02.27	12.0(0.2)	0.8(0.01)	0.1(0.01)	20.0(0.8)	1.6(0.2)	1.8(0.7)	1.1(0.1)								
G172.92-16.74	10.6(0.1)	1.6(0.01)	0.1(0.01)	8.1(0.3)	0.6(0.1)	0.7(0.2)	0.4(0.1)								
G172.94-05.49	14.0(0.6)	0.9(0.06)	0.3(0.06)	5.9(0.9)	1.1(0.4)	0.5(0.8)	0.8(0.3)								
G173.07-16.52	14.2(0.3)	0.9(0.01)	0.2(0.01)	9.3(0.7)	1.6(0.3)	0.8(0.7)	1.1(0.2)								
G173.12-13.32	7.3(0.4)		0.9(0.39)		1.5(1.0)		1.0(0.7)								
G173.36-16.27	10.1(0.6)	0.8(0.05)		4.9(1.8)		0.4(1.6)									